5-2008

Mutual Coupling Considerations in the Development of Multi-feed Antenna Systems

Sung-Woo Lee
University of Tennessee - Knoxville

Recommended Citation

Lee, Sung-Woo, "Mutual Coupling Considerations in the Development of Multi-feed Antenna Systems. " PhD diss., University of Tennessee, 2008.
https://trace.tennessee.edu/utk_graddiss/395

To the Graduate Council:

I am submitting herewith a dissertation written by Sung-Woo Lee entitled "Mutual Coupling Considerations in the Development of Multi-feed Antenna Systems." I have examined the final electronic copy of this dissertation for form and content and recommend that it be accepted in partial fulfillment of the requirements for the degree of Doctor of Philosophy, with a major in Electrical Engineering.

Aly E. Fathy, Major Professor

We have read this dissertation and recommend its acceptance:

Paul B. Crilly, Marshall O. Pace, Myong K. Jeong, Yoon W. Kang

Accepted for the Council:

Carolyn R. Hodges

Vice Provost and Dean of the Graduate School

(Original signatures are on file with official student records.)

To the Graduate Council:

I am submitting herewith a dissertation written by Sung-Woo Lee entitled *"Mutual Coupling Considerations in the Development of Multi-feed Antenna Systems."* I have examined the final electronic copy of this dissertation for form and content and recommend that it be accepted in partial fulfillment of the requirements for the degree of Doctor of Philosophy, with a major in Electrical Engineering.

Aly E. Fathy, Major Professor

We have read this dissertation
and recommend its acceptance:

Paul B. Crilly

Marshall O. Pace

Myong K. Jeong

Yoon W. Kang

Accepted for the Council:

Carolyn R. Hodges, Vice Provost and
Dean of the Graduate School

(Original signatures are on file with official student records.)

Mutual Coupling Considerations in the Development of Multi-feed Antenna Systems

A Thesis Presented for
the degree of
Doctor of Philosophy
The University of Tennessee, Knoxville

Sung-Woo Lee
May 2008

ACKNOWLEDGEMENTS

I would like to express thanks to my advisor, Dr. Aly E. Fathy, for his guidance and encouragement during the course of this dissertation. As a teacher, coworker, and like a brother his personality has kept reminded me the attitude of not only a researcher but a character. I can not forget my former advisor, Dr. Samir M. El-Ghazaly, at Arizona State University and early year of my study at University of Tennessee. His generous but keen insight motivated me in exploring the unknowns. My sincere appreciation is extended to my committee: Dr. Marshall O. Pace, Dr. Paul B. Crilly Dr. Myong K. Jeong and Dr. Yoon W. Kang for taking time to evaluate the context of this manuscript and provide valuable comments.

I am so grateful to my prayer supports from members of Korean Church of Knoxville. I would not forget the tears, prayer, and unfailing encouragement and support from my parents, family members, and my wife Mikeong Kim.

Above all, I would like this whole work be the praise to the Glory of Our Lord God.

“Praise the LORD, O my soul, and forget not all his benefits” (Psalm 103:2)

ABSTRACT

In the design of any multi-port network with more than one antenna, mutual coupling between these different ports must be accounted for. In an effort to investigate and control these mutual coupling effects, we have selected three structures to be thoroughly analyzed. Furthermore, they have been fabricated and tested to develop relevant design guides for these selected structures to have minimal mutual coupling effects.

These selected structures included a feed network for a multi-port antenna, a dual feedhorn for a large reflector antenna, as well as a set of Multi-Input Multi-Output (MIMO) laptop antennas. In the first study, we analyzed a 30-port radial splitter that can be used for an in-phase feeding of a 30-high power transmitter. Our objectives here have been geared towards estimating the mutual coupling between the 30 ports and exploring the port and alignment failure analysis, its graceful degradation results, and relevant efficiency performance for such high power multi-port network will be presented.

In the second study, we investigated the mutual coupling of a multi-feedhorn structure of a large reflector antenna in order to allow multi-beam radiation or reception. This high gain antenna utilizes integrated feeds with precise physical tight spacing and could suffer from strong inter-coupling. Mutual coupling effects here include input match deterioration, beam width broadening, and cross-polarization degradation due to the proximity coupling of these various feeds. Our study derived accurate feed location expressions as well as methods

to improve the decoupling between the feeds that have been implemented. These results will be discussed.

For the third study, we carried out extensive investigates into the mutual coupling effects amidst wireless laptop antennas for a MIMO system implementation. For a laptop use, it is required to determine the best location, optimum spacing, and orientations of these antennas in order to achieve the maximum benefits of the system's diversity. First, we studied the coupling between two antennas as a function of their spacing, types, and orientations. Subsequently, we extended the study to a controlled multi-antenna system for a MIMO implementation. Design rules for such implementation have been derived and will be discussed in detail.

TABLE OF CONTENTS

LIST OF TABLES

Table Page

LIST OF FIGURES

Figure Page

CHAPTER 2

CHAPTER 3

CHAPTER 4

CHAPTER I
INTRODUCTION

Motivation and Challenges

We designed and analyzed three different structures to investigate various mutual coupling effects. These structures are radial combiners/splitters of N-transmitters, feedhorn cluster of a large reflector for multi-beam operation, and an array of closely spaced laptop antennas for MIMO applications. Mutual coupling of these multi-port networks need to be controlled on all these applications to sustain high performance. Methods to investigate and minimize these mutual coupling effects are presented here in detail.

Radial Combiners

Power combiners/splitters can be used to feed multi-port antenna or to develop relatively high power amplifier systems beyond single amplifier typical performance. Combining/splitting efficiency and large amplifier graceful degradation are critical design considerations in their development. Port matching, magnitude and phase balance are the key factors to achieve high efficiency over wide band. Radial combiner amplifier design is based on the high structure symmetry and the utilization of almost identical amplifiers—balance in amplitude and phase. It is very important to understand, quantify and prevent the effects of any fabrication or assembly asymmetries or amplifiers imbalances to sustain high efficiency and graceful degradation performance.

As a widely accepted design/analysis methodology, circuit models are used in designing these radial combiners. But the existing circuit models represent only ideal symmetric structures with perfectly balanced amplifiers. Meanwhile using 3-dimensional electromagnetic (EM) models, possible non-ideal situations like asymmetric fabrication can be accounted for. In this regard, an EM model using CAD tools like HFSS has been developed and verified by measurement.

The full EM model was developed and investigated for two non-ideal situations.

1) The off-centered common feed situation as a common assembly problem was simulated.

2) Port failure was also considered emulating the progressive amplifier failure, and a full graceful degradation performance was carried out.

Mutual coupling strongly affects the combiner's overall performance and it is required to increase port isolation. Use of isolation resistors to bridge the various ports was evaluated to increase the isolation between the ports. Isolation resistors are used to dump higher order modes thus sustaining adequate balance between the ports.

Dual-Feed Horn for Reflector Antenna

Reflectors are utilized to achieve high gain directive antenna systems. For a multi-beam application, more than one feed antenna is used. For a low cost fabrication, it is advisable to integrate these multiple feeds into one platform.

These multiple feeds are defocused from the focal point to point the beams into different direction. However, there are three design issues:

1) Simulating such a large system--it is numerically immense beyond current full EM CAD tools capabilities.

2) Precise calculation of the beam angle as a function of the physical off-focus displacement.

3) Physical overlapping of feed horns for small beam deviation angles and can lead to a strong coupling and performance degradation.

For analysis, we have used the geometrical theory of diffraction (GTD) method for our calculations rather than using a commonly accepted beam deviation factor formulas. In the case of closely spaced feedhorns and to minimize their strong mutual coupling, we have used a diaphragm between these integrated feed horns. The effects of mutual coupling with and without this diaphragm have been thoroughly investigated and will be presented.

Multi-Input Multi-Output (MIMO) antennas for Laptops

MIMO concepts have emerged as an excellent solution for wireless communication to circumvent the reflective and reverberant multi-fading channel characteristics. Meanwhile, laptop computers have become one of the most highly used means for wireless mobile communication. The ever-decreasing space and the never-ceasing demand of more functionalities and robust connectivity for antennas brought the mutual coupling/isolation issues as the most active research area in laptop wireless communication. However, there are three issues/problems in this regard:

1) Identifying the proper antenna type when considering performance, shape and size.

2) Quantifying an acceptable mutual coupling level for a set of antenna types and orientations.

3) Relating the mutual coupling/isolation with wireless communication requirements and antennas physical spacing.

Survey of some appropriate antenna types for laptops, investigation of their mutual coupling as function of their physical spacing and orientations, and exploration of MIMO system implementation will be discussed in detail here.

CHAPTER II
MULTI-PORT RADIAL COMBINER/SPLITTER

There has been a considerable interest in recent years in developing a highly efficient and scalable approach to combining a large number of amplifiers at ever-increasing operating frequencies. Radial combiners have proved to be efficient, but due to their design complexity their use is still limited. We have investigated the currently available design approaches and devised and validated a simplified design procedure. Details are provided following some general background observations.

First, approaches to combining can be categorized into two groups: those that combine two amplifiers at a time (series combiners), such as tree-combiners, and those that combine N-amplifiers in one step (parallel combiners), such as radial combiners (RCs) [1-4]. The tree-structures have the disadvantage of utilizing a multitude of couplers and connecting transmission line segments, which add losses and significantly degrade the overall combining efficiency, especially for higher N. The RCs, on the other hand, do not have this disadvantage, since their common combining path lengths are generally minimized. In addition, careful design of the various sections and junctions of the radial combiner structures lead to a wider operating bandwidth – with over 90% combining efficiency [4].

Second, the binary trees are generally suitable for up to 8-way application, as in, 2^3 =N (i.e., order of 3, where the order is the number of combining stages). Losses of each planar splitter stage could amount (at X-band) to at least 0.15 to 0.25 dB [2]. Higher order splitters definitely suffer from the losses of the much longer lines at the later combining stages. Thus, it is anticipated that tree-combining efficiency will be significantly degraded for N>8 as shown in figure 2.1.

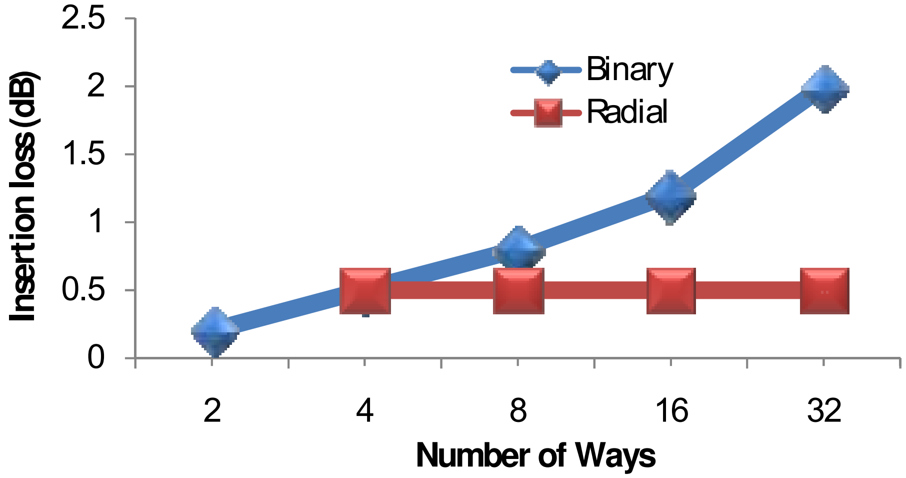

Figure 2.1. Loss of Radial vs. Binary Splitters due to ohmic and dielectric losses. For the binary combiner, it was assumed 0.25 dB loss per stage, and there is extra loss as we move to higher order combiners (i.e., larger N) due to the addition of very long lines to connect the different combining levels. However, for the radial combiner, we have only one splitting stage (where we assumed 0.40 dB for the radial line loss and a 0.15 dB for the loss of the input coaxial line transformer).

Figure 2.1 clearly demonstrates the main advantage of the radial combiners: providing a minimum path length. With a binary (tree) combiner, however, the divided signals in an N=8 way for binary structures travel at least 3λ/4 distance as they pass through three successive λ/4-divider sections that are connected in cascade. Based on [5], about 1 dB overall loss is anticipated for this type of combiner. On the other hand, the whole signal in the radial combiner passes through an optimally designed low-loss path for a relatively much shorter distance (as compared to binary combiners) and then is divided. Assuming the common path to be a parallel plate waveguide for insertion loss calculations, it is estimated that RCs at 12.5 GHz only suffer a 0.40 dB loss for the ≈ 1”- 30-way radial splitter distance, and another 0.15 dB insertion loss for the input coaxial line transformer (corresponding to roughly a 0.55 dB overall loss). This radial line loss estimate does not change significantly for larger N, and the above losses obviously do not include the [–10log(N)] dB drop in the signal power level due to splitting.

In Summary, RCs are known to render high combining efficiency, and are typically preferred when N>8. RCs present low loss, excellent amplitude/phase balance performance, and high power-handling capabilities [4]. RCs allow the placement of a large number of ports very close to the central combining port, and their high combining efficiency results whenever the combining path and its associated losses are kept at a minimum.

A full sketch of a radial combiner including the amplifier connections is shown in figure 2.2. The input signal is fed to the input of the bottom coaxial line,

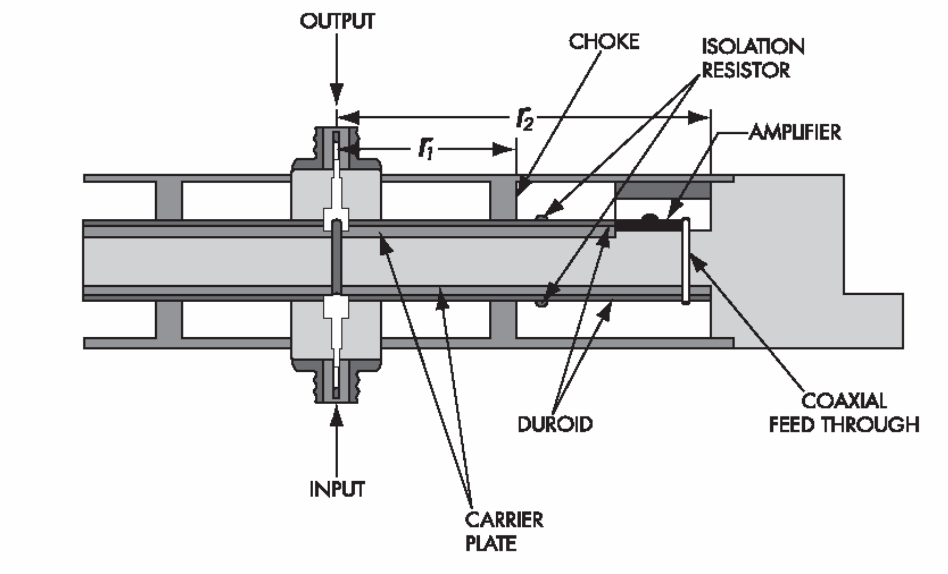

Figure 2.2. A Full sketch of the radial combiner showing the bottom splitter, the feedthroughs, the amplifier connections and the top combiner.

and then divided into N-equal signals (using a radial splitter), where each is vertically fed to the upper level through coaxial feedthroughs to the input of an amplifier at the upper level. These N-amplified signals are then collected (using a radial combiner very similar to the radial splitter) and are centrally fed to the upper output coaxial line.

The input signal (12 W) is fed at the bottom coaxial line input and divided into equal 30 signals, which are fed to the upper level through a coaxial feed-through to the input of each amplifier; these amplifier outputs (1 W each) are collected at the central point and fed centrally to the coaxial output line to obtain 30 W. Assuming almost 90% efficiency, we achieved 26.6 W output power at 12.5 GHz.

In this chapter, we will present a simplified, systematic methodology for the design of the basic building blocks of the RC. We then validate our simple approximate design formulas through a more accurate 3D-modeling using HFSS (this yielded excellent agreement between predicted and measured results). Then we will address the RC efficiency evaluation, its graceful degradation performance analysis, and some practical packaging issues such as cavity resonances and higher order mode suppression.

II-1 Radial Combiner (RC) Section

The RC consists of three sections: the launcher, the splitting path, and the N-way planar splitter. The launcher section (see figure 2.3) is a coaxial line feeding an infinite radial line. The splitting path (the radial line) is a low-loss, parallel-plate transmission line with a central-point excitation, where energy expands uniformly outward in the dominant E-mode with an axial electric field component. The radial line has relatively lower loss compared to a microstrip line (roughly one-third of the loss of a 50-ohm microstrip line, in our case). However, it is extremely important to symmetrically feed the radial line to prevent the propagation of higher order modes. Mechanical stability, feed symmetry, and proper selection of the outer diameter of the coaxial line launcher are keys to achieving balanced feed and uniformity. Propagation of higher order modes will, besides increasing the insertion loss, severely imbalance the amplitude and phase between individual peripheral ports of the N-way splitter (dominant mode propagates radially and higher order modes propagate circumferentially as well). The dominant mode provides in-phase balanced signal for all ports, while higher order modes change their polarity periodically in the circumferential direction every π/n angle (where n is the mode-number), and cause severe phase imbalance.

The selected common path (i.e., middle section) is a circular disc loaded at its rim with a resistive ring to provide damping of the circumferentially propagating higher order modes, sustaining adequate isolation between the ports. The disc is branched into N-microstrip lines that comprise the divider section. Microstrip lines are used to feed individual amplifiers and are relatively lossy; hence, their lengths should be kept as short as possible to maximize the combining efficiency.

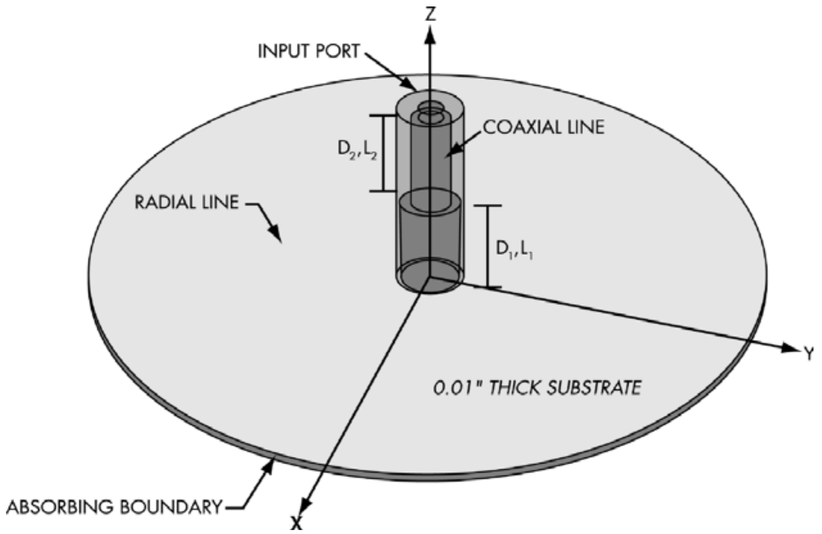

Figure 2.3. HFSS model for the coaxial/radial line structure. The radial line is centrally fed using a coaxial line, and the coaxial line (the launcher) has two $\lambda/4$ sections (impedance transformers). The HFSS model utilizes an absorbing wall at the edge of the radial line (the combining path), and the radial line radius r_c equals 1.1".

II-2 Feed Section Design

The radial line is centrally fed using a 50-ohm input coaxial line transformer. We use a Butterworth impedance transformer that is comprised of two $\lambda/4$ sections to provide a smooth impedance transition from the coaxial line to the radial line. For modeling, the coaxial line is terminated by the equivalent impedance of an infinite radial-line[1] [4, 5]. In general, the input impedance of the radial line is complex, but for a long radial line with a relatively large input radius, the imaginary part can be neglected. Hence, we assume that the infinite radial line at $r = r_o$ is represented by a pure real characteristic impedance given by:

$$Z_0 \approx \frac{h}{2\pi r_0}\sqrt{\frac{\mu}{\varepsilon_r \varepsilon_0}} \quad (2.1)$$[1]

where h is the substrate thickness, and r_o approximately equals half of the coaxial line outer conductor diameter, which is fixed at 0.166”. Based on a Duroid substrate of $\varepsilon_r = 2.2$, thickness h = 0.01 inch, and r_o = 0.083 inch, the equivalent impedance of the infinite radial line is ≈5ς. Consequently, we used a two-$\lambda/4$ section Butterworth coaxial transformer to provide adequate impedance transformation (over a 25% bandwidth), where at the design center frequency of 12.5 GHz the initial bottom section dimensions are: an inner diameter of D_1 = 0.144 inch and height L_1 = 0.275 inch; while

---

[1] The input admittance of an infinite radial line is, in general, not equal to the line's characteristic admittance; the relative input admittance is complex and has a negative imaginary (inductive) part. This is different from the relative input admittance of an infinite uniform line, which is always real and equal to unity. This inductive effect was evaluated and taken into consideration.

D_2 = 0.106 inch, and L_2 = 0.275 inch are the corresponding parameters for the top section as seen in figure 2.3. This initial choice will still lead to a poor input match due to the effect of the discontinuity of the coaxial-to-radial line transition and the inductive loading of the infinite radial line. Further optimization is necessary to improve the input match; to do so we can utilize either the circuit or the HFSS models to implement an optimization analysis, and our goal is to achieve greater than 25 dB for the RC input match.

Models Development

1) Circuit Model

We utilize the equivalent circuit model (shown in figure 2.4) to represent the launcher section. The junction discontinuity model is based on Williamson's equivalent circuit (figure 2.5), and the input radial line is assumed excited only by the dominant E mode [6, 7], where its input admittance (Y`) is given by [3]:

$$Y^{'}(r) = \frac{j + Y^{'}(r_o)\xi(x,y)ct(x,y)}{Ct(x,y) + jY^{'}(r_o)\xi(x,y)} \tag{2.2}$$

$$ct(x,y) = \frac{J_1 N_{oo} - N_1 J_{oo}}{J_o N_{oo} - N_o J_{oo}} \tag{2.3}$$

$$Ct(x,y) = \frac{J_{1o} N_o - N_{1o} J_o}{J_1 N_{1o} - N_1 J_{1o}} \tag{2.4}$$

$$\xi(x,y) = \frac{J_o N_{oo} - N_o J_{oo}}{J_1 N_{1o} - N_1 J_{1o}} \tag{2.5}$$

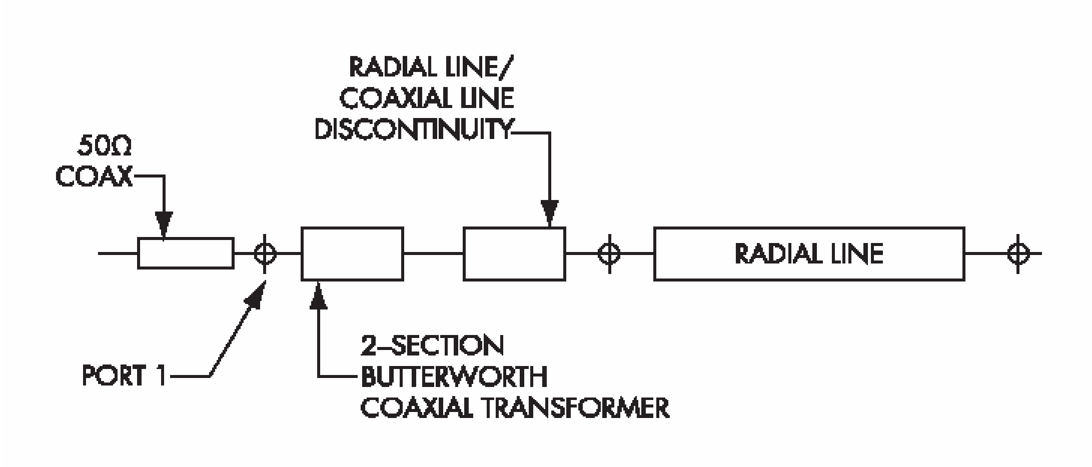

Figure 2.4. Equivalent Circuit Model of the Radial Line Feed Structure (the Launcher). This one-port network is terminated by an absorptive boundary condition at point M shown above.

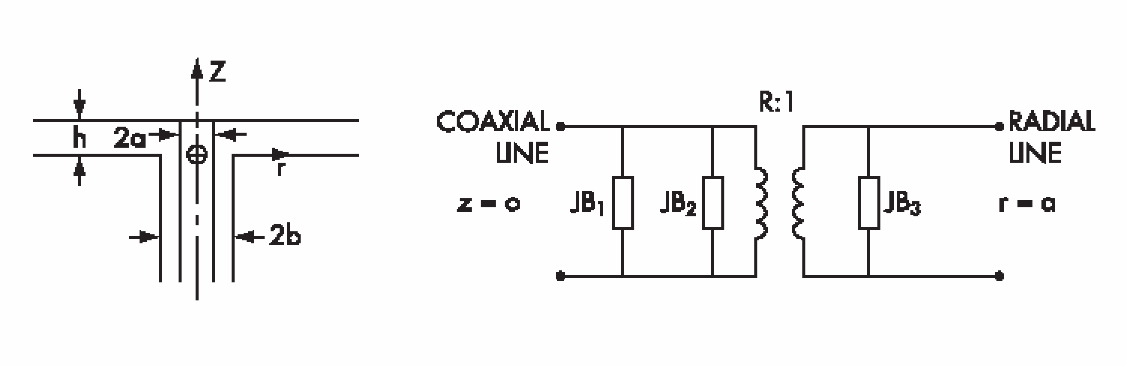

Figure 2.5. Williamson’s radial line/coaxial line junction equivalent circuit; use Ref [6] for details.

When using *Bessel* (J) and *Neumann* (N) functions with, $x=kr$, $y = kr_o$, $J_o(kr) = J_o$, $J_o(kr_o) = J_{oo}$, $J_1(kr_o)=J_{10}$ and Y'(r) is the relative admittance at any radius r given in terms of a reference relative admittance $Y'(r_o)$ evaluated at radius r_o and $k = 2\pi/\lambda$.

2) EM Model

We utilize the HFSS model to represent the launcher section. A circular disc terminated by an absorbing boundary modeled the infinite radial line. The one-port network and its coaxial line excitation shown in figure 2.3, including a match-absorbing boundary at the rim of the disc, were modeled using HFSS. We carried out an extensive analysis, and our predicted and measured results of the input return loss (RL) are shown in figure 2.6. “Circuit model” and “HFSS” predictions were in very good agreement with measured results. Subsequently –

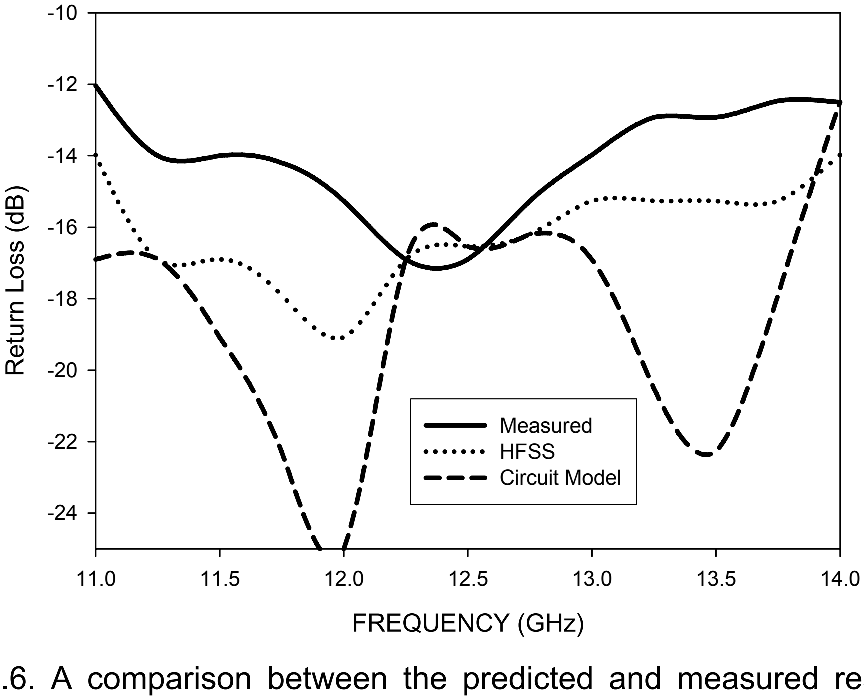

Figure 2.6. A comparison between the predicted and measured results of the input return loss.

and based on our models and the optimization of the structure shown in figure 2.3 to minimize input reflections – it was necessary to absorb the inductive junction discontinuity by slightly reducing the height of the first coaxial line transformer bottom section to L_1= 0.245 inch.

II-3 Designing the Combining Path and the Peripheral Ports

It is important to keep the signal common path in a radial line format as long as possible to minimize the insertion loss of the RC. The radial line has much lower loss as compared to the use of the microstrip line. Hence the length of the microstrip lines was kept as short as possible. We assumed that the amplifiers when populated in the combiner make a circle with radius r_a, which is determined from the number of amplifiers and their widths. In our design, r_a equals 1.24 inch (based on using 30 amplifiers of 0.25 inch width each), and the optimum radius of the radial line disc r_c is then determined approximately as (r_a minus one λ/4- wavelength in dielectric). At r_c, the radial line has a real-value characteristic impedance and is given by:

$$Z_0 = \frac{h}{2\pi r_c}\sqrt{\frac{\mu}{\varepsilon_r \varepsilon_0}} \tag{2.6}$$

which is branched into N-sections and the impedance of each section is:

$$Z_0 = \frac{Nh}{2\pi r_c}\sqrt{\frac{\mu}{\varepsilon_r \varepsilon_0}} \tag{2.7}$$

Hence, we need one λ/4-microstrip transformer section to provide a smooth impedance transition from the impedance given by (7) to the 50-ς amplifier input impedance. In our case, the microstrip line section was designed to transform an 11 ς (the equivalent impedance at r_c) to a 50 ς at r_a. Peripheral port to port isolation was measured and compared to theoretical predications using HFSS as shown in figure 2.7, where good agreement was demonstrated.

A. HFSS and the Circuit Models

We have developed a circuit model to simulate the overall combiner structure. The structure includes the coaxial line launcher, the disc, and the 30 microstrip line transformers. The applicability of this equivalent transmission-line description is restricted to a single-mode propagation case, and having no higher-order mode interaction between any geometrical discontinuities of the structure. The approximate circuit and the fabricated test fixture for our experiment are shown in figure 2.9. Based on implementation of the optimization analysis using the circuit and the HFSS model to minimize the overall input reflections and transmission insertion loss, it was concluded that we needed to reduce the length of these 30 microstrip line transformer sections to 0.140 inch, and hence absorb the effects of the discontinuities.

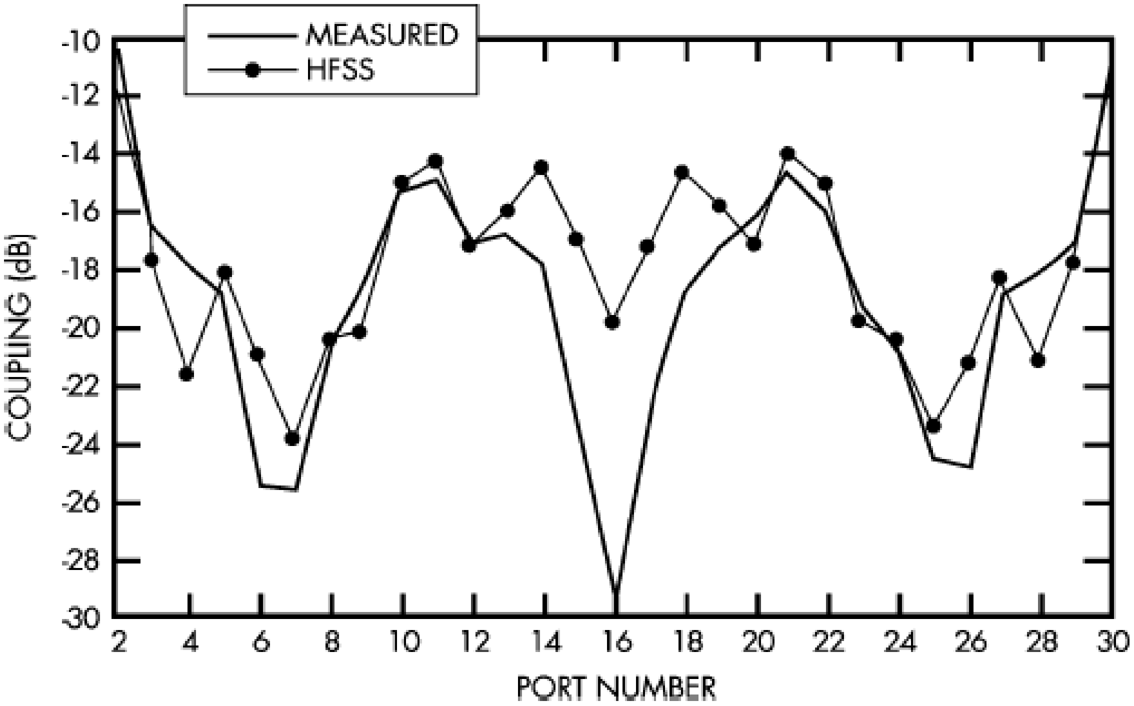

Figure 2.7. Comparison between HFSS and the measured coupling (isolation) results (no isolation resistors case).

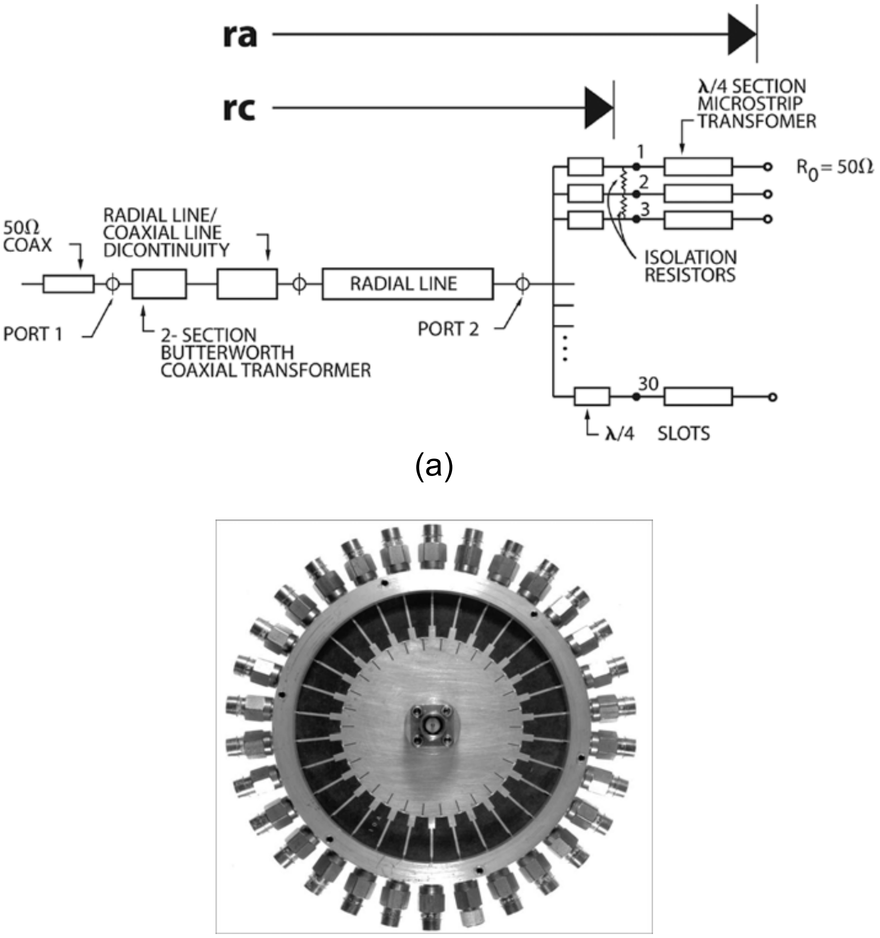

(a)

(b)

Figure 2.8. (a) Full circuit model of the radial combiner (b) Test fixture used for measurements.

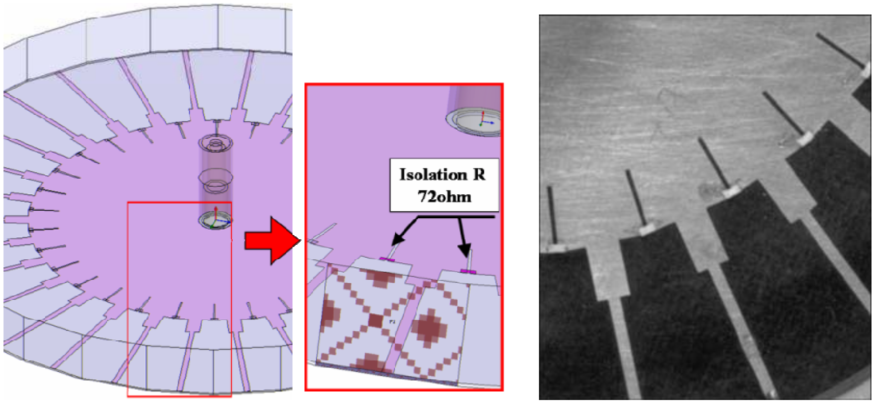

Figure 2.9. HFSS Model including the isolation resistors, and a picture of the real structure where chip resistors have been implemented.

B. Summary of the Step-by-Step Design Procedure

1) We estimated the initial approximate structure dimensional values for the various sections:

a) Based on the RC combining efficiency "η", and each amplifier linear power rating P_{linear}, determined N the combiner order (ways).

$$N = \frac{\left(\dfrac{\text{Required Output Power}}{\eta}\right)}{P_{\text{linear}}} \tag{2.8}$$

b) Measured each amplifier width "W_a", and based on N, determined the combiner radius r_a.

$$r_a = \frac{(N * W_a)}{2\pi} \tag{2.9}$$

c) Added a slot ring radius r_c; as $r_c = r_a - \lambda/4$. At the edge of the disc, we opened N slots to create ports. The narrow slots were λ/4 long. Adding bridging resistors and λ/4 slots (shown in figure 2.8) helped in damping higher order modes.

d) λ/4 microstrip transformers were required between r_c and r_a. Where the impedance of this transformer is given by:

$$Z = \sqrt{50\sqrt{\frac{\mu}{\varepsilon_r \varepsilon_o}}\frac{Nh}{2\pi r_c}} \tag{2.10}$$

e) At the input side (i.e., the launcher), we needed a two λ/4 coaxial transformer. Where their characteristic impedances for a Butterworth design are given by:

$$Z_2 = (50)^{0.75}\left(\sqrt{\frac{\mu}{\varepsilon_{rc}\varepsilon_o}}\frac{h}{2\pi r_0}\right)^{0.25} \tag{2.11}$$

and

$$Z_1 = (50)^{0.25}\left(\sqrt{\frac{\mu}{\varepsilon_{rc}\varepsilon_o}}\frac{h}{2\pi r_0}\right)^{0.75} \tag{2.12}$$

where ε_{rc} is the dielectric constant of the coaxial line filling (loading). Similar coaxial transformer sections will be needed at the output of the radial combiner.

2) The Optimization Step:

a) Using HFSS, we optimized the input coaxial launcher that is connected to an infinite radial line or an absorbing boundary, as shown in figure 2.3. The goal of this step was to minimize the input return loss over the wide band.

b) Using HFSS, we built a model that included all the sections (similar to figure 2.9b). We optimized the whole structure for a minimum insertion loss and a good input match (from the coaxial line side) over the operating band.

II-4 Associated Practical Problems

In building the combiner, we tackled three major practical problems: (1) excitation of higher order modes due to any structural asymmetries, (2) EM coupling between peripheral ports, and (3) package cavity resonances. In this section, we will address these problems in detail.

A. Suppression of Higher Order Modes

One of the major problems when utilizing a radial line is the excitation of higher order modes, which is triggered by any mechanical asymmetries in the structure. While the dominant mode travels in the radial direction and its phase front is uniform along the circumference, higher order modes propagate circumferentially, causing their phases to be a function of their traveling angle. As previously explained in Section II-3, higher order modes could add to or subtract from the dominant mode, causing amplitude ripples and significant phase imbalance and thus significantly lowering the combining efficiency. Hence, it is essential to suppress these modes.

A radial line with height $h < \lambda/2$ (parallel-plate waveguide height) will have a higher order mode propagation constant given by [5]:

$$\kappa^2 = k^2 - \left(m / r\right)^2 \tag{2.13}$$

where κ is the propagation constant and *m* is the mode number. The dominant mode *(m* = o) has propagation constant κ =k*,* while all higher order modes (if excited) are below cutoff at small values of *r*. Higher order modes will propagate at different critical radii, as given by $r_m > m/k$, for mode number m. For example, at the periphery of the radial line, up to 6 higher modes can exist and propagate at 12 GHz for a radial line with substrate thickness *h* = 0.254 mm and $\varepsilon_r = 2.2$, if excited. Therefore, the possibility of excitation of higher order modes has to be reduced by exercising great care in the mechanical design and assembly to avoid any structural asymmetry. Also, the radial-to-coaxial junction should be designed to be at a small radius ($r_o < \lambda/2\pi$) so that all higher order modes will be below cutoff at this interface as well. Any remaining asymmetries may lead to higher-mode excitation, but fortunately those undesirable modes possess circumferential current components and radial magnetic field components. Therefore, the use of radial slots will impede their circumferential path, and they can also be absorbed with resistors that intercept the circumferential current component. Experimentally, we found out that damping of those higher order modes will noticeably maintain the balance among ports, especially if there is any mechanical asymmetry or non-uniformity of amplifiers.

B. Isolation

Another important aspect of higher order mode damping is failure tolerance. A well-designed radial combiner has the feature of graceful degradation. This means that there is sufficient isolation between ports, and failure of one amplifier does not result in any progressive failure of other amplifiers or consequent load-pull effects. Ideally, the choice of isolation resistors should provide

$$S_{ij} = \begin{cases} 0 & \text{if} \quad i = j \\ \text{minimum} & \text{if} \quad i \neq j \end{cases} \tag{2.14}$$

where S_{ij} is the scattering coefficient from peripheral port *i* to peripheral port *j.* This choice would allow a uniform and maximum isolation between ports. The proper value will serve to limit the inherent strong coupling between adjacent and opposite ports (see figure 2.9 for HFSS model). Experimentally we have achieved a minimum isolation of 16 dB, by placing $\lambda/4$ slots (0.176”) into the disc (i.e., the radial line). Slots are bridged by isolation resistors, as shown in figure 2.10 [9] to secure better phase and amplitude balance between the N-ports when impeding the propagation of any radial line higher order mode, as seen in figure 2.8. The resistor values (72 ohms) were experimentally evaluated, and their use is based on a complete experimental justification by measuring the performance both with and without these resistors and noticing some performance improvement with resistor utilization.

Consequently, we were able to maintain a good uniformity. This uniformity rendered a measured amplitude imbalance of ±0.4 dB and phase imbalance of only ±5° as shown in figures 2.11 and 2.12, respectively. With these very good results, we were able to build a combiner that has a combining efficiency of over

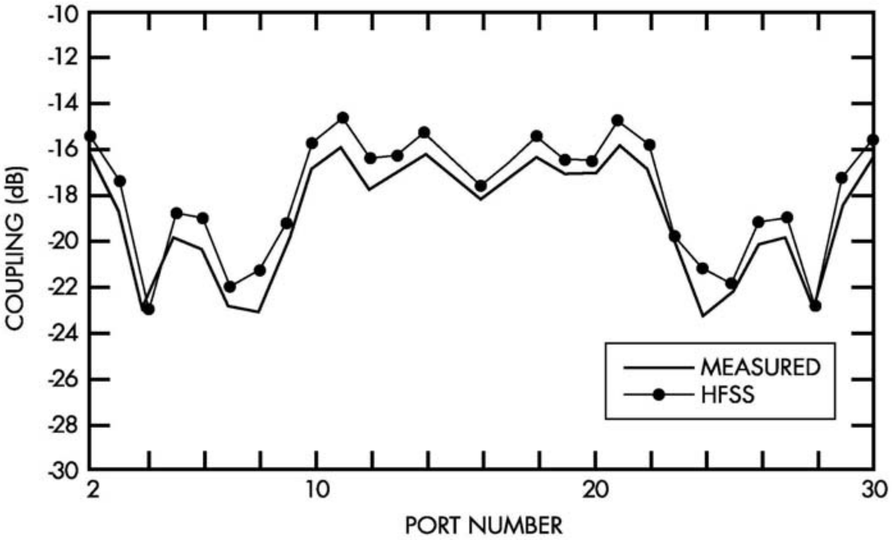

Figure 2.10. Comparison between measured and HFSS calculated coupling (isolation) between different ports after using the isolation resistors.

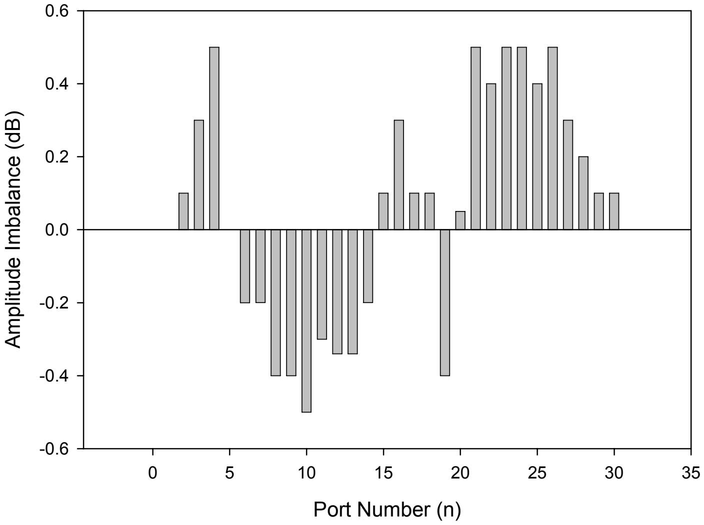

Figure 2.11. Radial Combiner measured transmission coefficient S1n amplitude deviation was evaluated. Where |S1n| was measured between port 1 (center port) and port n (a peripheral port) while all other ports are match-terminated, n goes from 1 to 30. The figure shows the amplitude deviation as function of port #. The imbalance is < ±0.5 dB above average.

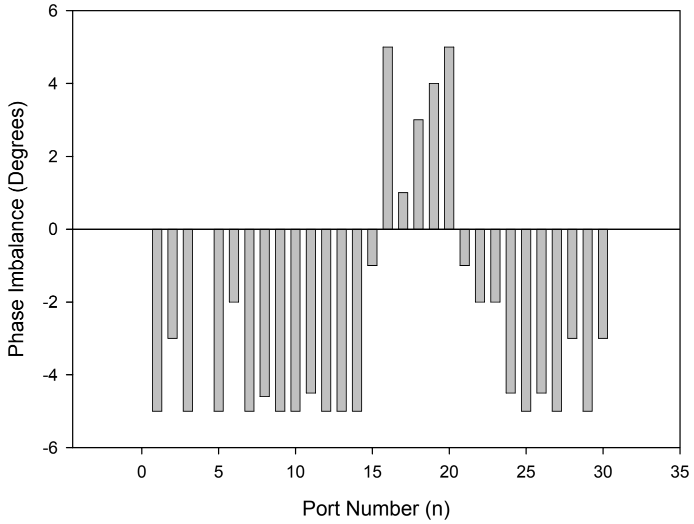

Figure 2.12. Radial Combiner transmission coefficient S1n phase variations, where phase (S1n) was measured between port 1 (center port) and port n (n is any peripheral port where n = 2,3,…30) while all other ports are match-terminated. The above figure shows the phase deviation of the transmission coefficient for all peripheral ports. The measured phase imbalance is within ± 5 degrees above average.

90%. Obviously, the overall efficiency will depend on the amplifiers' amplitude and phase uniformity that will be populated in the combiner.

C. Cavity Resonances

The back-to-back radial structure with its coaxial and microstrip transitions is shown in figure 2.2. The cover above the microstrip line creates a cylindrical cavity with a number of resonant frequencies that can greatly affect the combiner performance, if they fall within the frequency band of interest. It is important, therefore, to predict these cavity resonances and avoid them by displacing their frequencies far enough away from the operating frequency range.

To predict the resonant frequencies, we considered a radial line short-circuited at both the outer radius r_2 and the inner radius r_1 (seen in figure 2.2). For an E-type radial line with an electrical length

$$y - x = k(r_2 - r_1)\,,$$

where k is the wave-number, the resonance condition is

$$ct(x = kr, y = kr_1) = -\infty\,. \tag{2.15}$$

where ct(x,y) is a combined function given by expression (4). Since the total admittance at r_1 is the sum of the two admittances seen looking at both ends, the input admittance due to the short at r_2 should equal ∞ at r_1. In particular, given the ratio $y/x = r_2/r_1$, a solution of equation (2.15) in terms of $y\text{-}x= k(r_2 - r_1)$ can be found. According to the dimensions we used, the predicted resonance frequency is 11.2 GHz. Figure 2.13 shows the input VSWR degradation due to resonance at that frequency.

A choke is used to eliminate this resonance. Its dimensions were chosen to locate r_1 at roughly the junction of the radial line and the 30 microstrip lines. Now the dominant resonance, as evaluated by equation (2.15) and according to the new ratio (r_2/r_1), occurs at 7.3 GHz (see figure 2.14). Resonances of other higher order modes are also far away from the operating frequency band. In addition, the choke's specified location serves as a necessary balun to the transmission line to enable conversion from balanced to unbalanced operation.

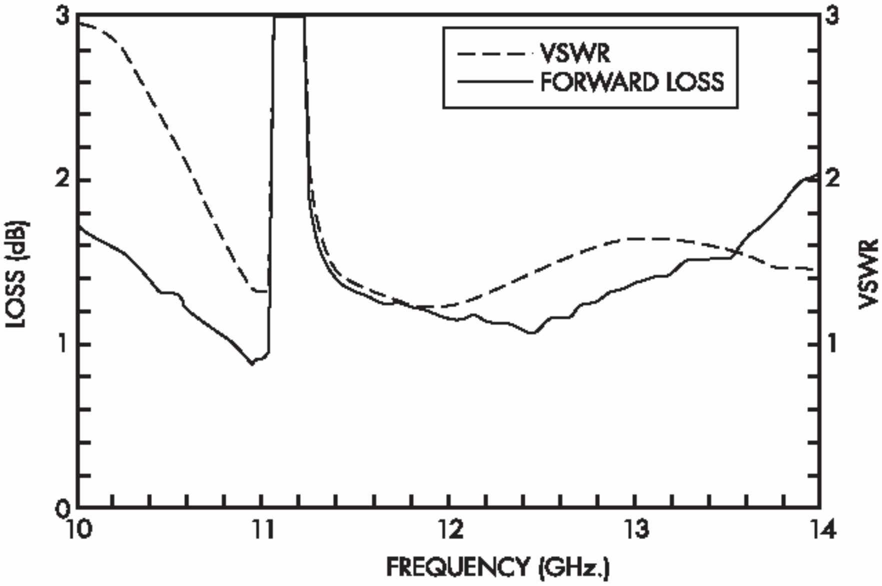

Figure 2.13. Package resonance of the complete combiner without the choke. The resonance is close to 11 GHz, slightly affecting the performance. Input VSWR is < 2 over the band.

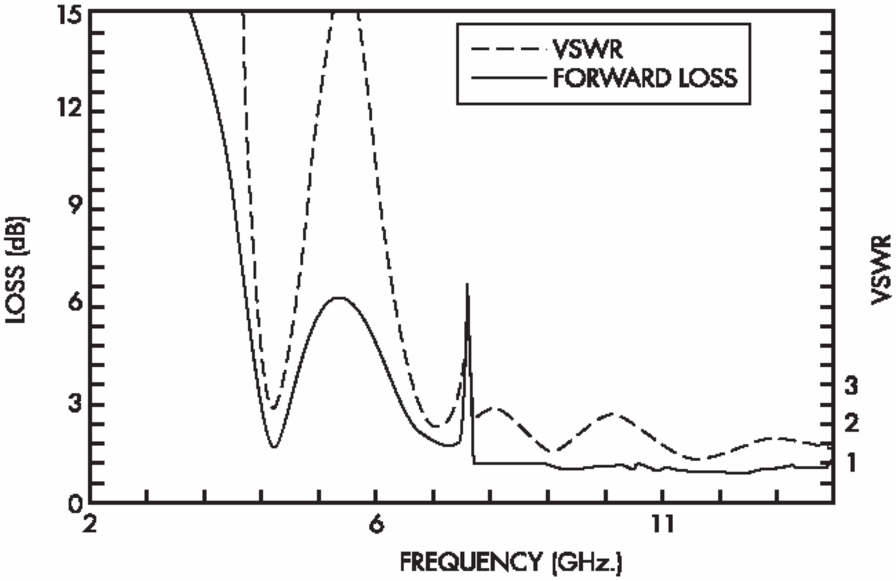

Figure 2.14. Package resonance of the whole combiner when using a choke, where the resonance now has moved to 7 GHz.

II-5 Populated RC Performance

Thirty amplifiers were picked up to populate the radial combiner [4]. Their typical output power is 1 W. Their amplitude and phase deviation were less than ±1 dB and ± 15º degrees, respectively. We carried out measurements of a back-to-back combiner/divider structure to evaluate its insertion loss. We concluded that within our frequency band the insertion loss of either the combiner or the divider structure is approximately 0.40 dB. An extra 0.15 dB needs to be added to the divider loss due to the feed-through from the divider level to the combiner level. Therefore, the overall divider loss is 0.55 dB, as demonstrated in the efficiency figure 2.16.

A series of measurements was also performed to determine the amount of power lost in the isolation resistors due to asymmetries. We first recorded the temperature differences of all resistors measured with respect to the radial combiner top metallization. Then, based on a calibration of power dissipated vs. temperatures taken on resistors mounted with similar boundary conditions, the original readings were converted to dissipated power values in the resistors. Due to the amplifiers' amplitude and phase imbalance, a few isolation resistors dissipated significantly more power than the rest. The calculated power dissipated in the isolation resistors under this condition is shown in figure 2.15, which amounts to an overall power loss due to asymmetries of about 0.9 W or

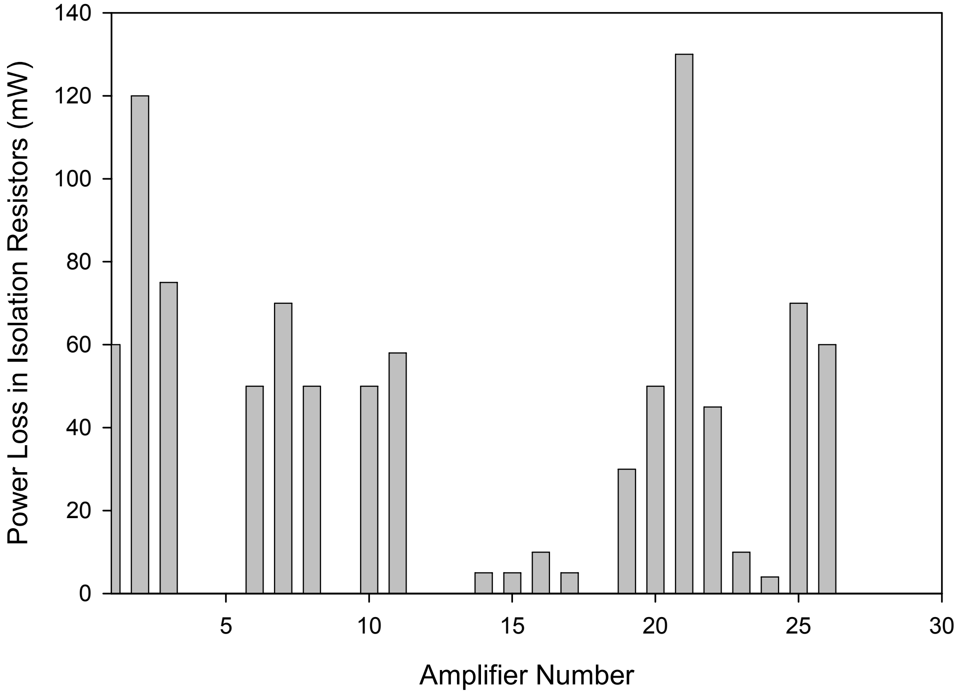

Figure 2.15. Estimated power loss in each isolation resistor based on previously calibrated-resistor chip-temperature rise vs. dissipated power.

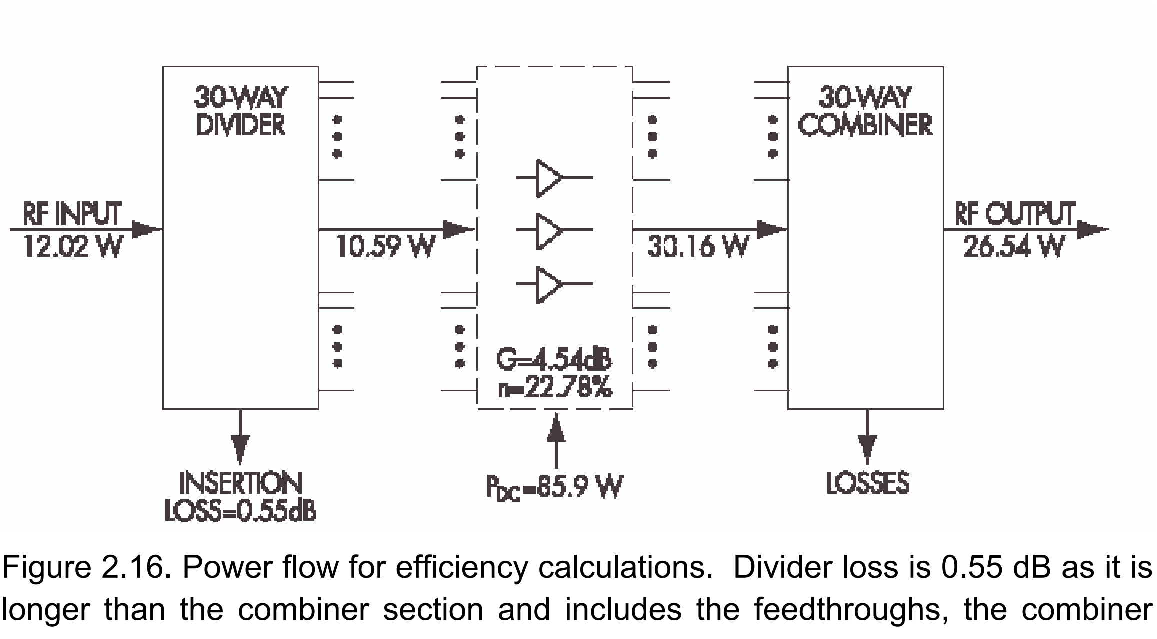

Figure 2.16. Power flow for efficiency calculations. Divider loss is 0.55 dB as it is longer than the combiner section and includes the feedthroughs, the combiner loss is 0.4-dB insertion loss, and 0.15 dB due to amplifiers non-uniformity, based on thermal analysis (where a total of 0.9 W was estimated).

0.15 dB. Even this amount could be further reduced if the power amplifiers have been individually corrected for phase deviations to be less than ±15°. Hence, the total combiner insertion loss is also 0.55 dB.

Figure 2.16 shows the estimate of the overall efficiency, based on the radial divider/combiner insertion loss and amplifier performance unbalances. The combining efficiency then is very close to 90% after taking the amplifier's performance variations into account. The populated combiner structure provided 26.5 W at normal operating conditions.

II-6 Graceful Degradation

If we have N identical amplifiers that are reasonably matched and have adequate isolation, it is expected that the total output power to fail gracefully as one or more amplifiers fail [9-13]. In this case, the output voltage at the common port typically becomes (N-m)/N of its maximum value with no amplifier failures, which corresponds to a power drop of

$$P_{out} \big/ P_{out,\max} = \left(1 - m/N\right)^2 \tag{2.16}$$

where *m* is the number of failed amplifiers, and N=30 in our case. This is still short of the optimum graceful degradation (derived by the sum of the output of the remaining amplifiers) as given by:

$$P_{out} \big/ P_{out,\max} = \left(1 - m/N\right). \tag{2.17}$$

A number of graceful degradation tests were performed and the RC structure demonstrated excellent graceful degradation performance. For example, we turned off up to seven amplifiers and a mere 1.6-dB power drop was measured. See figure 2.17 for our results when we emulated amplifier failures by turning off their bias in a progressive, step-by-step fashion. Additionally, we investigated the effect of shorts that may occur when power devices fail, by placing shorts at different positions; a change of the overall gain degradation with respect to the turned-off results was anticipated. But at most an additional drop in the output power of 1 W per each amplifier failure was found at the worst location of the short. Hence, it was concluded that the failure model is slightly better than the $((N-m)/N)^2$ case (as seen in figure 2.17). Graceful degradation is extremely valuable feature for these solid-state combiners – when reliability is an issue – compared to traveling wave tubes.

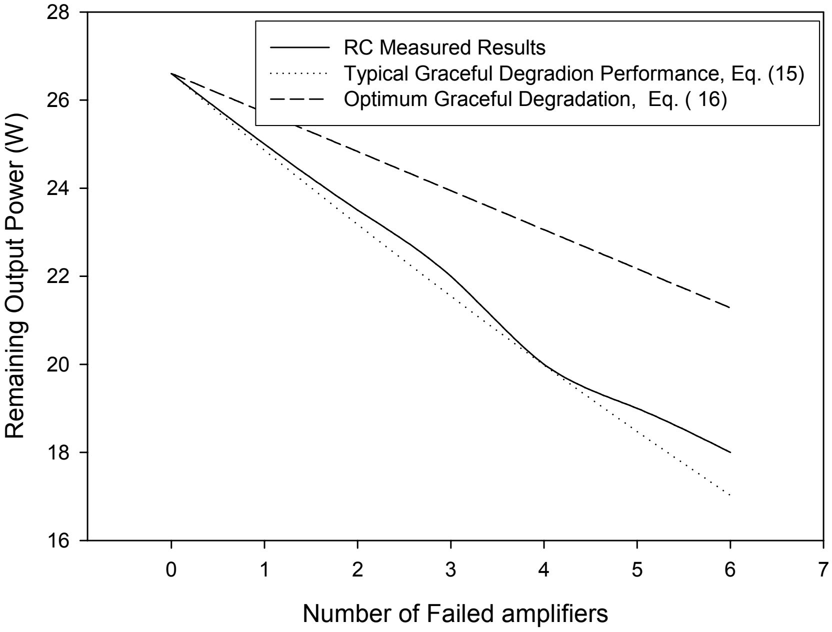

Figure 2.17. Measured output power with emulated amplifier failure (by turning their corresponding bias off). RC results are slightly better than $((N-m)/N)^2$ graceful degradation model.

II-7 Port Failure and Off-center Study

In order to validate the performance enhancement using isolation resistors, two additional studies have been considered; 1) off-centering the coaxial input port and 2) port failure simulations shown in figure 2.18. As mentioned in previous sections, any imbalance in magnitude, phase and port impedances will degrade system efficiency and performance. Off-centered coaxial input feed introduces unequal radial travel distances to the radial outputs. This causes significant phase and magnitude imbalances. Through off-centering simulation input case study the imbalances can be quantified. Port failures affect isolations between radial peripheral output ports. Reflections from failed ports (due to amplifiers being short or open) traveling back and forth could degrade the isolation symmetry and cause magnitude and phase imbalances. Figure 2.18 depicts the simulation concepts of off-centering and progressive port failure analyses.

Moving the feed off the center, the amplitude and phase deviations became worse than when it was at the center. Adding the isolation resistors between the ports had improved the match of each port and also reduced the non-uniformity in both the amplitude and phase. Similarly, for the port failure, the amplitude and phase distribution change a lot due to having short/open circuit terminations. The resistors use is a circuit concept for improving the isolation, but

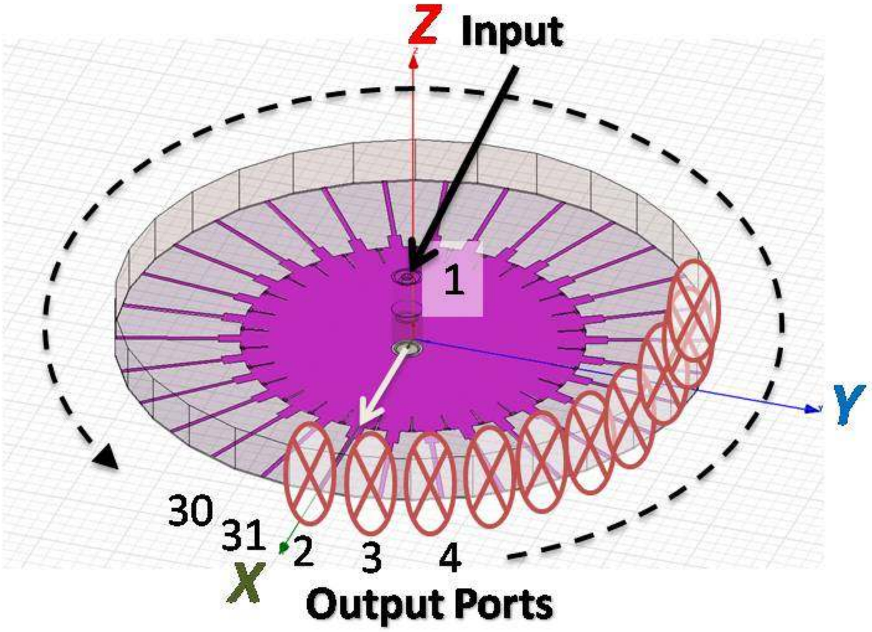

Figure 2.18. Off-centering coaxial input simulation (indicated as the arrow) and progressive radial output port failure (x-marked ports were shorted with PEC boundaries) simulation setups.

from an EM point of view it was found out that it does not localize these failures as expected and energy does not propagate only in the lateral direction as anticipated from the circuit point of view. The reflections from the opposite ports cause these imbalances.

Both off-centering and port failing simulation results, in figure 2.19, show that the isolation resistors ($R_{Isolation}$) mitigated the port isolations, and overall magnitude and phase variations. The obtained output port matching performance was very poor, about -5dB, and the isolation resistors improved -20dB or less in every situation.

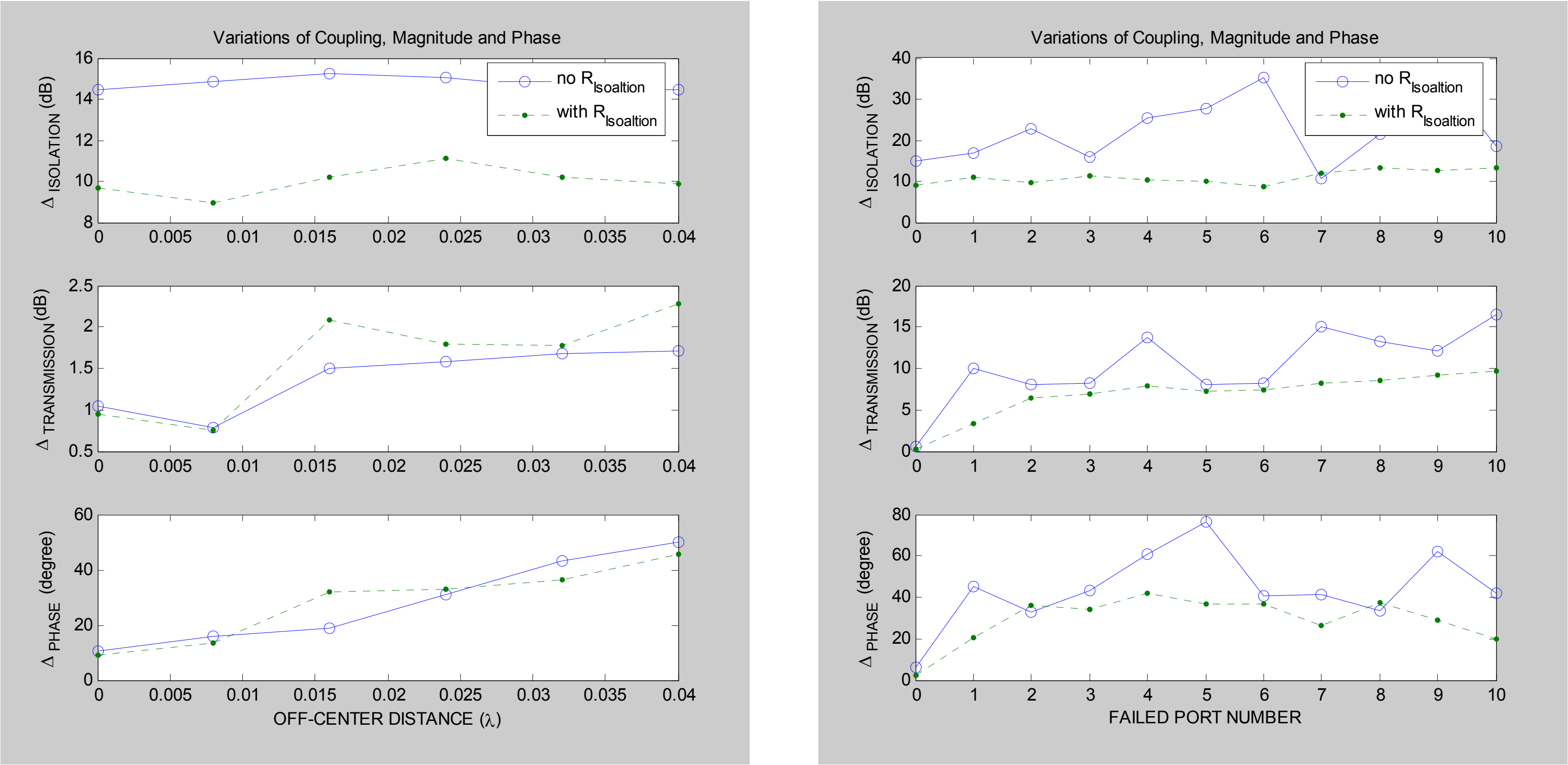

(a) Off-centering coaxial input simulation results

(b) Output port progressive failure simulation

Figure 2.19. HFSS simulation results of variations on isolation, transmission and phase (maximum deviations among the radial output port were taken); (a) off-centered input port without port failure (b) progressive port failure with centered input.

The isolation resistors are important as they cause the ports to become 50 ohms which is essential for power amplifier operation otherwise their matching and linear operation will be affected and cause the overall efficiency degradation. The results clearly indicate that the isolation resistors slightly improved the port isolation for both cases: 1) port failure 2) off center.

II-8 Conclusion

A simple technique has been presented for the design of radial power combiners with a highly predictable performance. The technique is general, and may be applied to any similar N-way radial combiner structure. The developed approximation has been validated by circuit model analysis and HFSS modeling. A detailed comparison between the predicted results and the measurements is presented here.

We have demonstrated that the N-way power combiner is a very compact, lightweight structure that is ideally suited for space and airborne applications, and could be easily designed with today's CAD tools starting with our simple approximations. The radial combiner structure has excellent efficiency, amplitude, and phase uniformity, as well as excellent heat dissipation capability. Results for this populated combiner with power amplifiers of 1 W each are included here to validate its graceful degradation performance. Much higher power levels (well in excess of 100 W/per device) could be achieved by further increasing N and using higher power amplifiers and isolation resistors with better heat sink.

CHAPTER III
DUAL-FEED HORN FOR REFLECTOR ANTENNA

For large-feed arrays, designers of satellite communication systems frequently employ offset reflectors to avoid blockage effects while utilizing a tailored feed to provide an edge taper of approximately -10 dB [13]–[15]. For a multi-beam reflector operation, it becomes necessary to illuminate the reflector with a slightly defocused feed [16]–[19] to allow utilization of multiple feeds [20]. Either axial or lateral feed displacement (i.e., “feed defocusing”) introduces beam-scanning capability. But for even a limited scan-angle, this will be associated with slight radiation pattern degradation. In general, this scan-angle θ_B is a function of the reflector’s focal length F, its diameter D, and the feed’s physical displacement δ, and is related to the feed angle by the beam deviation factor (BDF). Typical expressions for BDF evaluation are approximate similar to the one given in [14], and it is necessary to evaluate it more accurately for small or very large defocusing distances using CAD tools that take diffraction effects into account. In order to produce two independent (dual) beams with 4.5°—beam spacing using an offset dish reflector, two laterally displaced feed-horns are used. However, for ease of assembly and to reduce the number of parts count, an integrated twin-feed horn structure with a pre-determined center-to-center spacing between the two horns was developed. An estimate of this offset distance was initially obtained through consultation of a graph provided in [14], [17]. Where for an F/D ratio of 0.59 and a feed tilt angle of $\Psi_c = 48°$ (see figure

3.1) an approximate BDF value of 0.93 was obtained based on [17]. In the following, we will address the need for accurate spacing evaluation of this integrated dual feed in Section III-2. The coupling effects on patterns symmetry due to the feeds proximity coupling will be investigated. The overall performance of a 60 cm reflector (D = 60 cm) fed with this twin feed horn structure will be demonstrated.

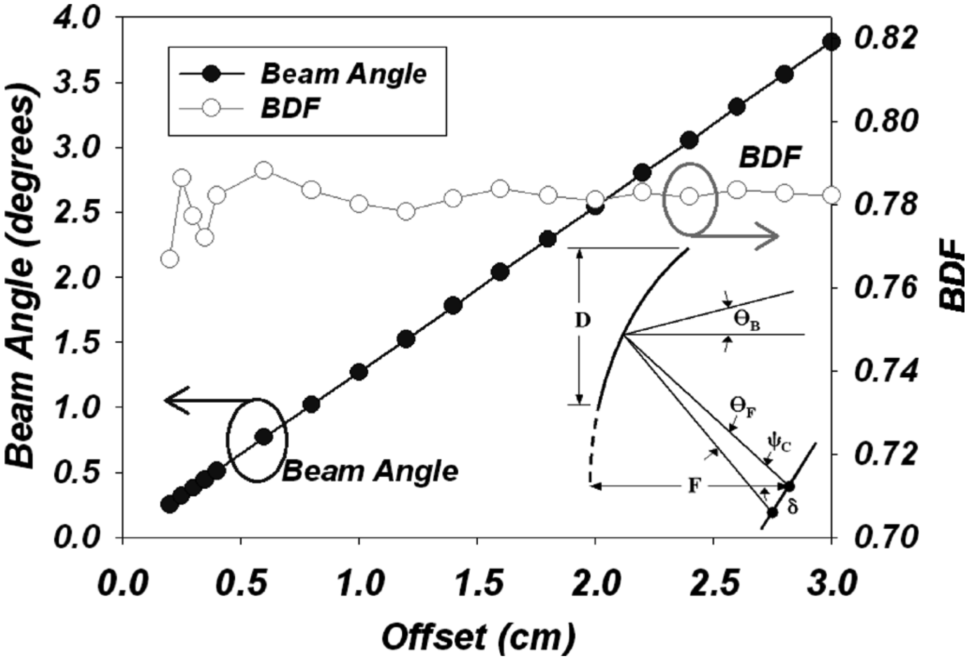

Figure 3.1. Beam “deflection” angle θ_B for a feed offset distance of a 60-cm reflector. The BDF for the lateral feed displacement of offset parabolic reflector is given by: BDF $=\theta_B / \theta_F$, where $\theta_F = \tan^{-1}(\delta = F)$.

III-1 Single-Horn Development

Design of high-performance aperture antennas puts emphasis on providing radiation patterns with low side-lobe levels and high gain. Corrugated feedhorns with circular aperture are preferred, as they are generally used to produce relatively low first side-lobe levels. In addition, corrugated horns are utilized to provide pattern symmetry. Their assumed radiation pattern is given by [14]:

$$E_\theta = K \cos^M \theta \tag{3.1}$$

where M is a constant.

A special design of a conical corrugated horn antenna was selected. The selected antenna structure, its cross-section, and its radiation pattern are symmetric. Based on experimental evaluation and for a 1.75 in. diameter, M = 6 as shown in figure 3.2. Its measured gain of 14 dB indicates a relatively high aperture efficiency of 85%.

Additionally, a full-wave model was successfully developed based on the High Frequency Structure Simulator (HFSS) commercial software package [22]. The feedhorn antenna performance was predicted and full parametric study was carried out. For simplicity, the feedhorn flanges were modeled as thin perfect electrical conductor (PEC) boundaries (as shown in figure 3.3). In addition, a full parametric study was carried out, in which the symmetry of the radiation patterns at both the E and H planes was examined. Our parametric study included the effects of the heights of the PEC corrugated flange. The optimum design goal

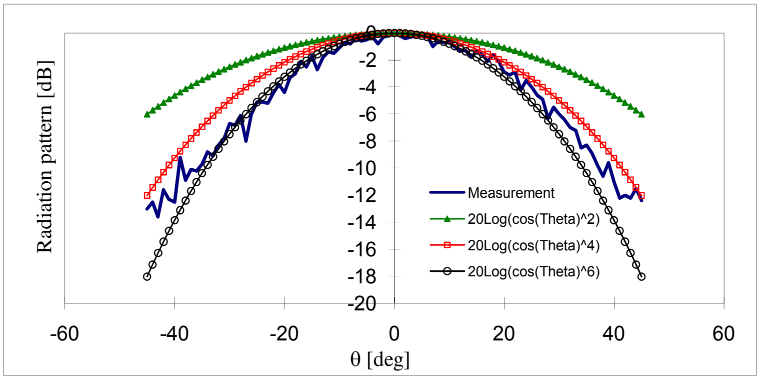

Figure 3.2. Source feed pattern approximation. (M = 6).

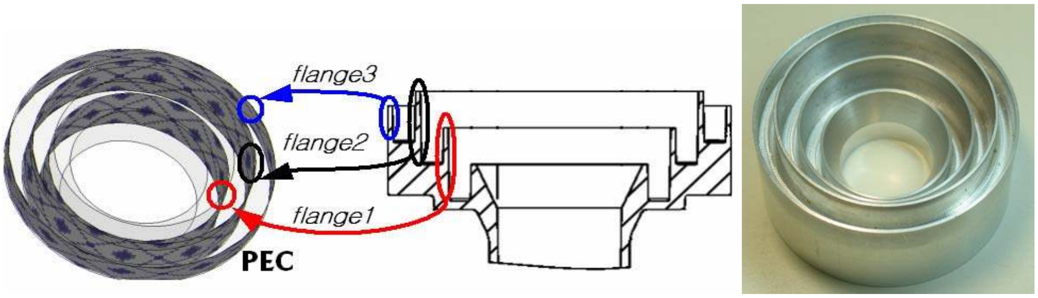

Figure 3.3. HFSS model for the corrugations and manufactured part.

was to minimize the difference between the E- and H-plane radiation patterns to help assure symmetry. This difference was quantitatively set to be less than 0.5 dB within the main beam range, and less than 2.0 dB for off-broadside angles up to ± 30 degrees, as shown in figure 3.4. Low side/back- lobe levels have been demonstrated for the structure with the selected optimum dimensions as seen in figure 3.5. HFSS simulated results indicated an overall antenna gain of ≈ 14 dB, and an excellent input match. These predicted results were compared to the measured results and a summary of gain performance across the frequency range is shown in figure 3.6.

III-2 Development of an Offset Feed

A. Offset Feed Displacement

A more accurate BDF value can be obtained by utilizing CAD programs that include diffraction effects. For example, when using an offset lateral distance of 1.5 cm, a 1.98° beam angle value is predicted utilizing Grasp8 [21] as demonstrated in figure 3.1. The predicted angle corresponds to a BDF value of only 0.78, not 0.93 as approximately provided by the graph in [17]. The predicted beam angle as a function of the feed offset distance is shown in figure 3.1.

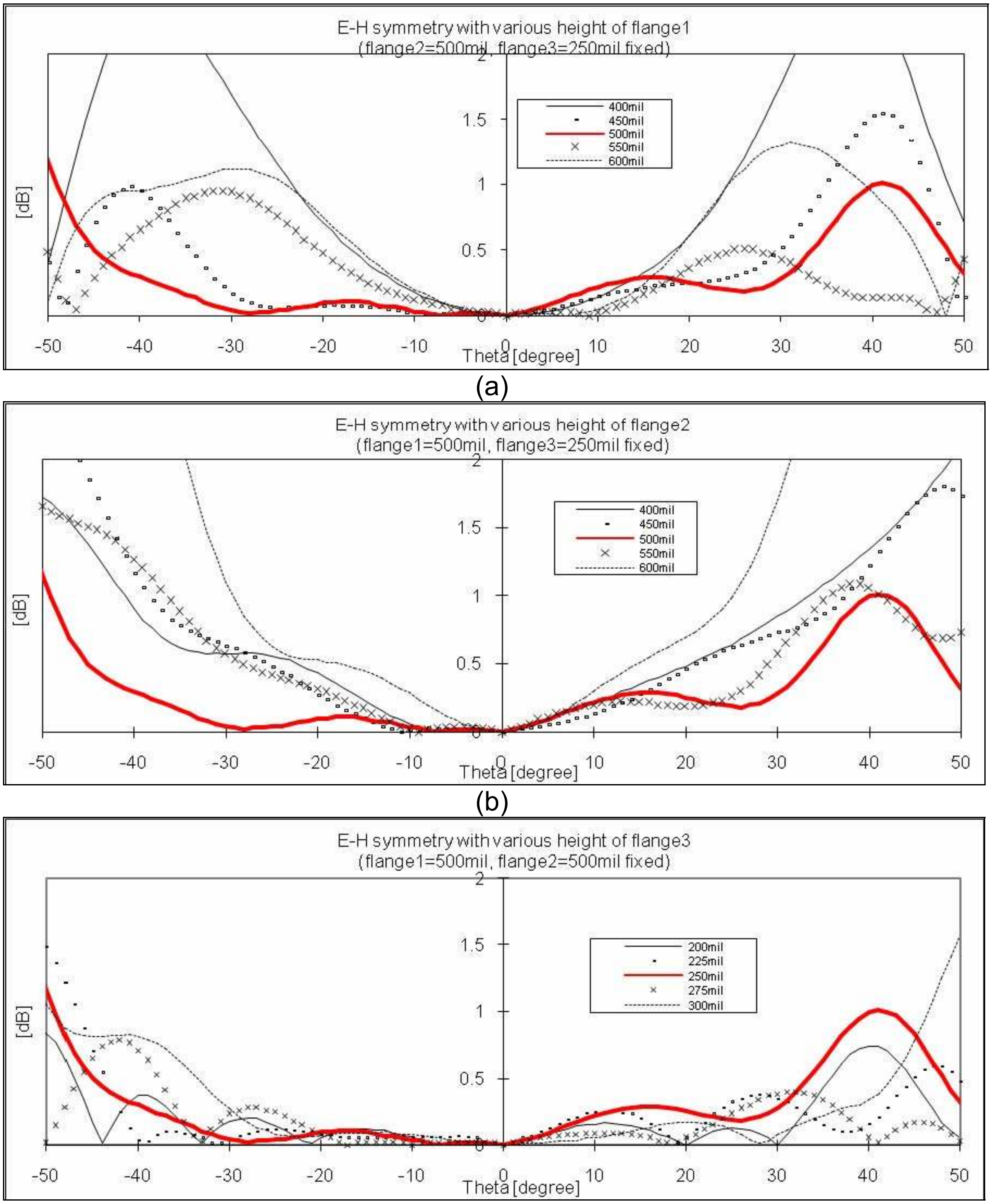

(a)

(b)

(c)

Figure 3.4. Full-wave parametric study on the E-H pattern symmetry over heights of (a) flange1 (while flange2: 0.5 in., and flange3: 0.25 in.), (b) flange2 (while flange1: 0.5 in., and flange3: 0.25 in.), and (c) flange3 (while flange1: 0.5 in., and flange2: 0.5' in.) at 12.2 GHz. (optimum dimensions are: flange1: 0.5 in., flange2: 0.5 in., and flange3: 0.25 in.)

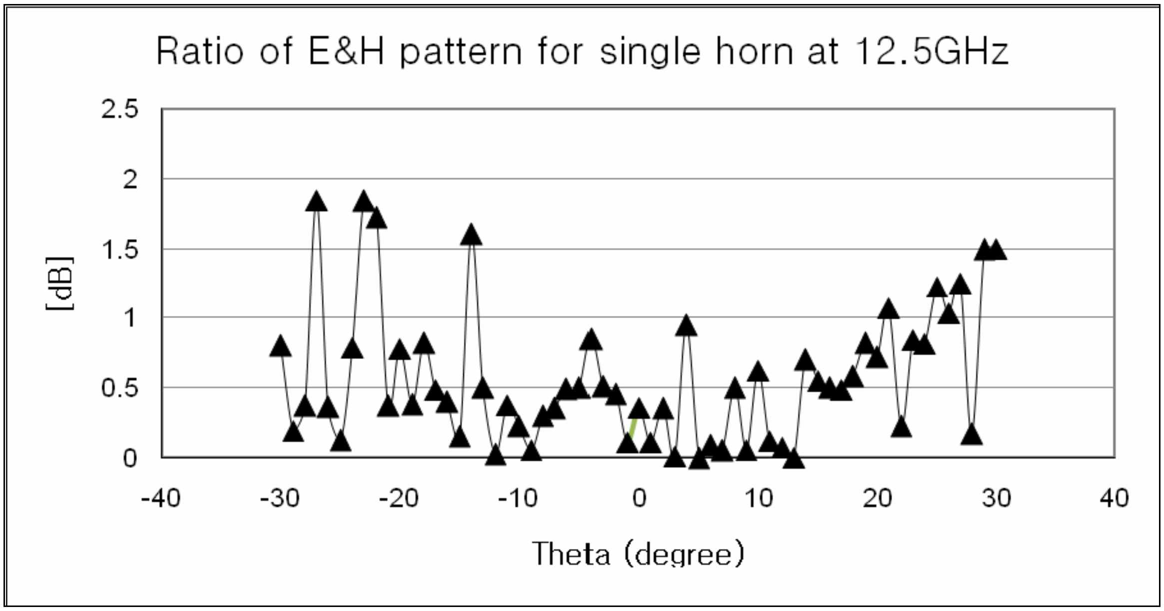

Figure 3.5. Measured E-H pattern symmetry with optimum corrugated flange dimensions.

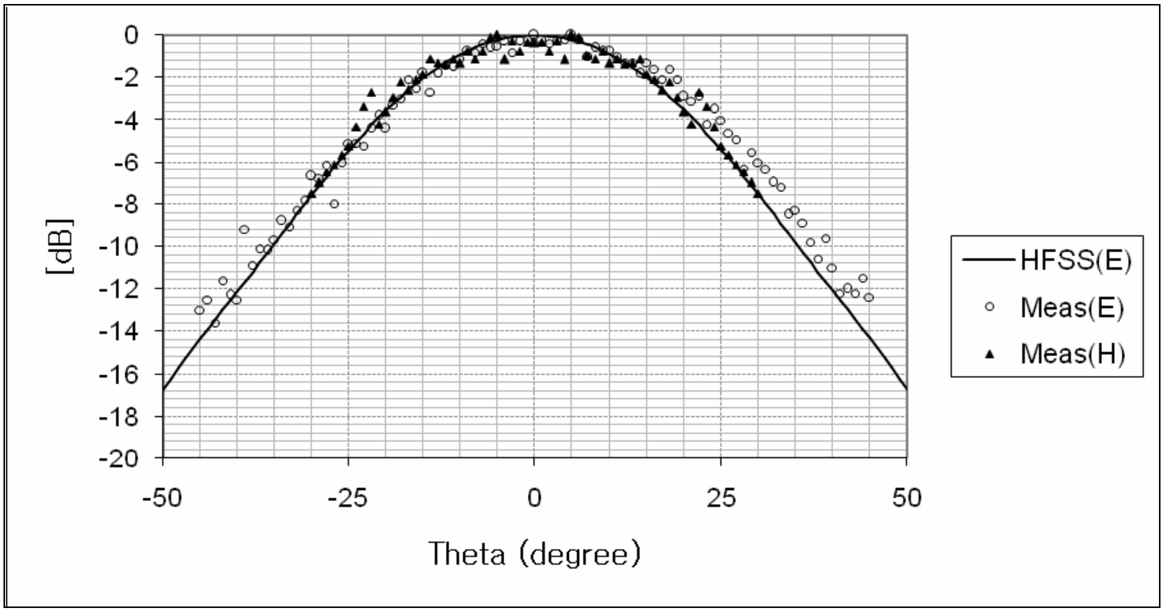

Figure 3.6. Radiation pattern of corrugated feedhorn (solid line: HFSS simulation; marked points: measured data).

B. Beam Deviation Factor

In order to produce two independent (dual) beams from an offset dish reflector, two feedhorns that are laterally displaced are used. However, an integrated twin feedhorn structure can be used instead to provide a 4.0° dual beam spacing. This spacing is determined according to the dish size “D”, and the focal length “F”. An estimate of this offset distance was initially obtained through consultation of a graph provided in [14, 17], and based on the ratio of the beam deflection angle (θ_B) and the angular displacement of the feed from the focal point (θ_F); identified in figure 3.7 (where for an F/D ratio of 0.59 and a feed tilt angle of 48° the BDF is constant and equals 0.93 based on [17]). This BDF value can be predicted using equation (3.2) here, as a function of k, where $0 < k < 1$. And when k equals 0.55, the formula yields a BDF value of 0.93.

$$BDF = \frac{\sin^{-1}\left(\delta / F\right)\left[1 + k(D/4F)^2\right] \Big/ \left[1 + (D/4F)^2\right]}{\tan^{-1}\left(\delta / F\right)} \tag{3.2}$$

However, upon utilization of SABOR [24] and NEC-REF [25] programs based on geometrical theory of diffraction (GTD), the predicted BDF value was not a constant but rather a function of the feed angle θ_F, especially when small displacements are involved. For example, when using an offset lateral distance of 2.0 cm, a 2° and a 2.09° beam angle values were predicted utilizing SABOR and NEC-REF programs respectively. Those predicted angle values correspond to a BDF value of only 0.8 as indicated in table 3.1.

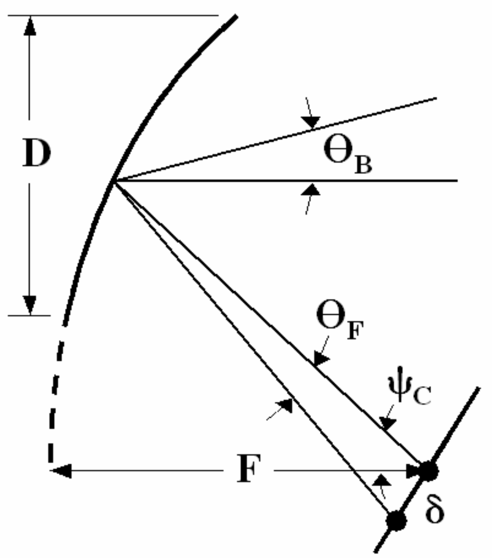

Figure 3.7. Beam deviation factor (BDF) for the lateral feed displacement of offset parabolic reflector. BDF is given by: BDF = θ_B/θ_F.

Table 3.1. Calculated BDF ratios for different feed offsets

		NEC-REF Code		SABOR	
Feed Offset Distance (cm)	Feed Angle (θ_F) degrees	Beam Angle (θ_B) degrees	BDF	Beam Angle (θ_B) degrees	BDF
0.2	0.326	0.2	0.614	0.253	0.777
0.25	0.407	0.4	0.983	0.316	0.777
0.3	0.489	0.4	0.818	0.403	0.825
0.35	0.57	0.4	0.702	0.466	0.818
0.4	0.652	0.6	0.921	0.529	0.812
0.6	0.977	0.8	0.819	0.782	0.801
0.8	1.302	1	0.769	1.03	0.792
1	1.628	1.4	0.86	1.31	0.805
1.2	1.953	1.6	0.82	1.56	0.799
1.4	2.278	1.8	0.791	1.84	0.808
1.6	2.603	2	0.769	2.09	0.803
1.8	2.928	2.4	0.82	2.34	0.8
2	3.252	2.6	0.8	2.62	0.806
2.2	3.577	2.8	0.783	2.87	0.803
2.4	3.901	3.2	0.821	3.15	0.808
2.6	4.225	3.4	0.805	3.4	0.805
2.8	4.548	3.6	0.792	3.65	0.803
3	4.872	4	0.822	3.93	0.807

C. Twin Feedhorn Corrugated Structure

In our integrated feedhorn design, it was necessary to overlap the corrugated flanges, as the required center-to-center spacing between the two horns is less than a single-horn aperture diameter. Therefore, the twin feed structure with the overlapped corrugation (shown in figure 3.8) was studied. Its predicted and measured performance is demonstrated in figure 3.9, where the measured return loss (RL) is better than 20 dB and the isolation between the two horns exceeds 30 dB, which is very similar to the performance of a single feed. The radiation patterns of the twin feedhorn structure have been also measured and compared to that of the single horn structure. Radiation patterns for the co-polarization and cross-polarization are shown in figure 3.10 for two orthogonal

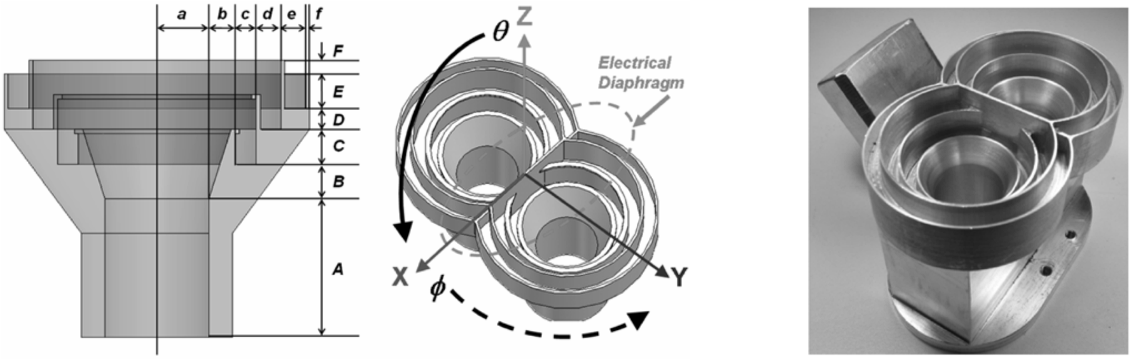

(a) HFSS model (b) Manufactured structure

Parameter	A	B	C	D	E	F
Unit(cm)	2.54	1.27	0.635	0.381	0.635	0.254
Parameter	a	b	c	d	e	f
Unit(cm)	0.9525	0.4953	0.381	0.4572	0.4572	0.0762

Figure 3.8. Integrated feedhorn structure. (a) Dimensions of the twin feedhorn and (b) manufactured structure.

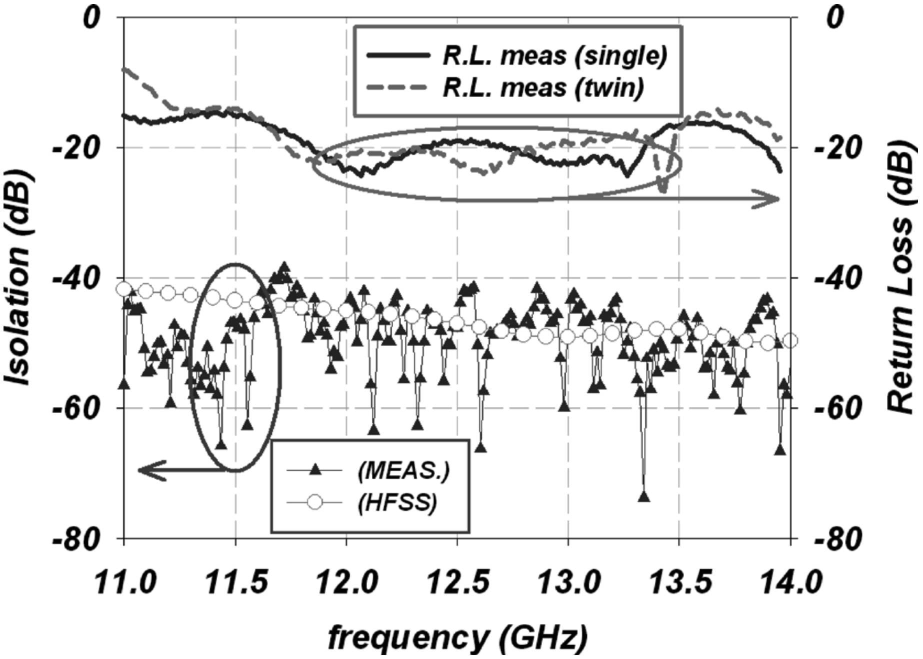

Figure 3.9. Predicted and measured isolation and RL of the twin feedhorn structure. HFSS simulation and measured isolation are on the left y-axis. Measured return loss for both single and twin feedhorn structures are on the right y-axis.

feeding modes. Based on these simulations, which used HFSS [22], it was concluded that the co-polar radiation patterns, apart from slight asymmetry, were very similar to the single horn case as well. While, as anticipated, the cross-polarization levels have been slightly increased. It was also observed that adding a separating wall, seen in figure 3.8, degrades both the radiation pattern symmetry and the isolation as indicated in figure 3.11.

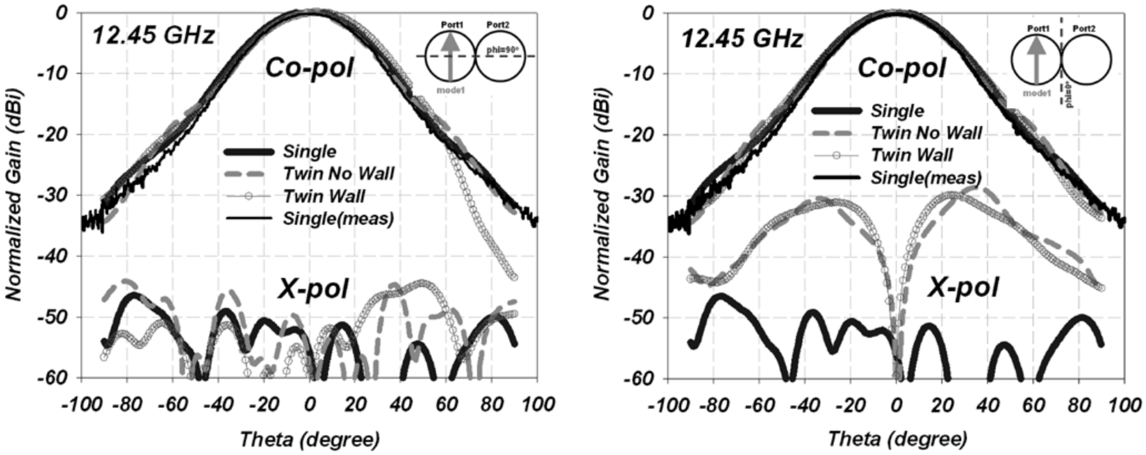

(a) Radiation pattern (mode1, phi(ϕ)=90°) (b) Radiation pattern (mode1, phi(ϕ)=0°)

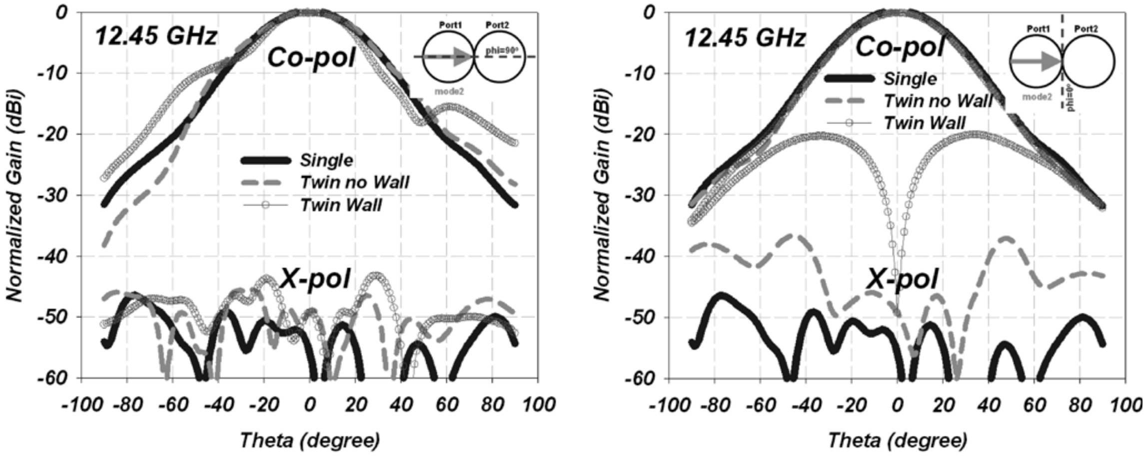

(c) Radiation pattern (mode2, phi(ϕ)=90°) (d) Radiation pattern (mode2, phi(ϕ)=0°)

Figure 3.10. Polarization radiation patterns oat 12.45 GHz of the developed twin feed structures at both x-z, and y-z planes (i.e., phi(φ) = 0°, 90°) as indicated in figure 3.8. The above graphs include the simulated performance of a separate single horn and that of one of the twin horns with and without the separating wall (diaphragm). The measured response of a single horn is added for comparison. (a) Radiation pattern (mode1, phi(φ) = 90°); (b) radiation pattern (mode1, phi(φ) = 0°); (c) radiation pattern (mode2, phi(φ) = 90°); (d) radiation pattern (mode2, phi(φ) = 0°).

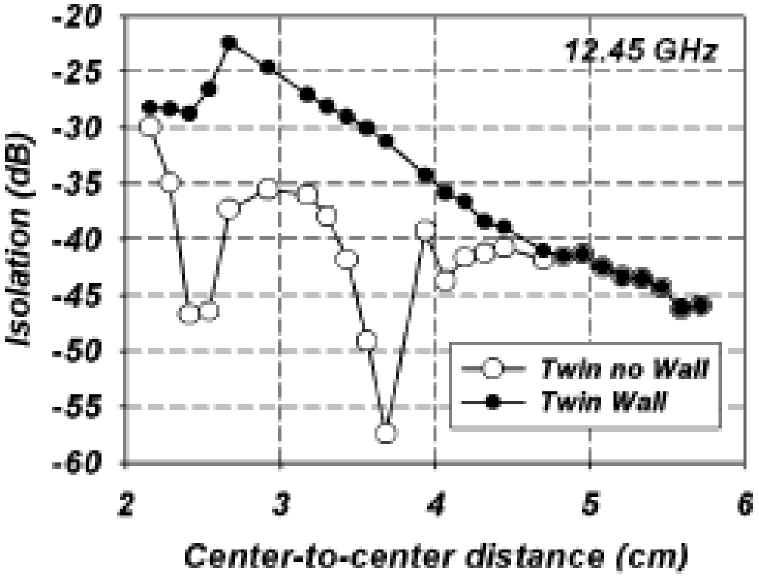

(a) Coupling effect due to the wall

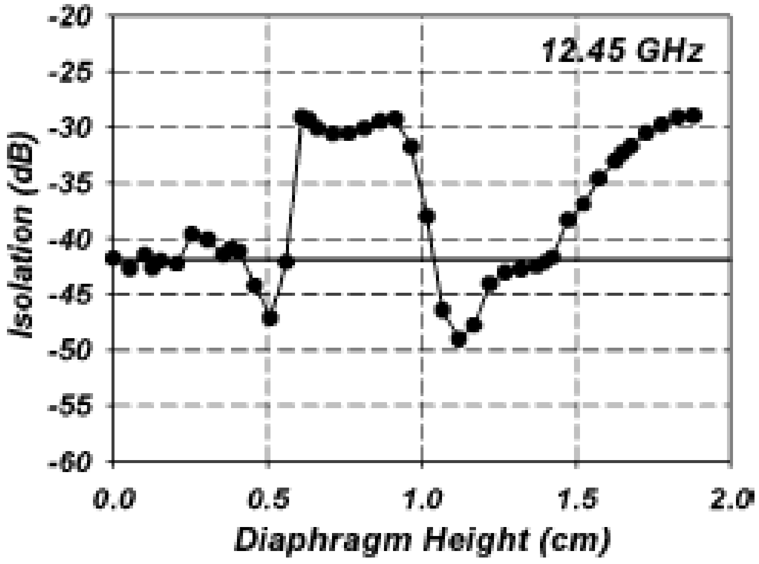

(b) Effect of the wall height

Figure 3.11. (a) Coupling between the two horns as a function of the center-to-center distance for a nominal wall height of 1.905cm. (b) Effect of the wall (electrical diaphragm) height on the decoupling between the two horns for a nominal center-to-center spacing of 3.429cm.

III-3 Overall Performance of the 60 cm Reflector

Finally, a vertical near-field measurement system [23] was used to test the 60 cm reflector antenna with the newly developed twin-feedhorn in the frequency range of 12.2 to 12.7 GHz. After the amplitude and phase measurements are obtained on a near-field grid, a Fourier transform of the near-field grid results in the far-field. Table 3.2 summarizes the measured results of the center and offset beams. An example of the overall measured performance of the 60-cm offset reflector at 12.45 GHz is shown in figure 3.12. Notably, the measured separation of the dual beams is 4.5° which is consistent with our predictions. The predicted center beam gain is 35 dBi with a 93% and a 57% spillover and aperture efficiencies respectively. Meanwhile, for the defocused horn, a slight drop in efficiency is seen for the offset beam due to a less efficient aperture illumination (54%).

Table 3.2. Measured gain and beam separation angles of the reflector antenna system

Frequency (GHz)	Center Beam Gain (dBi)	Offset Beam Gain (dBi)	Measured Beam Seperation (deg)
12.2	35.23	34.44	4.51
12.45	35.62	35.05	4.54
12.7	35.82	35.28	4.55

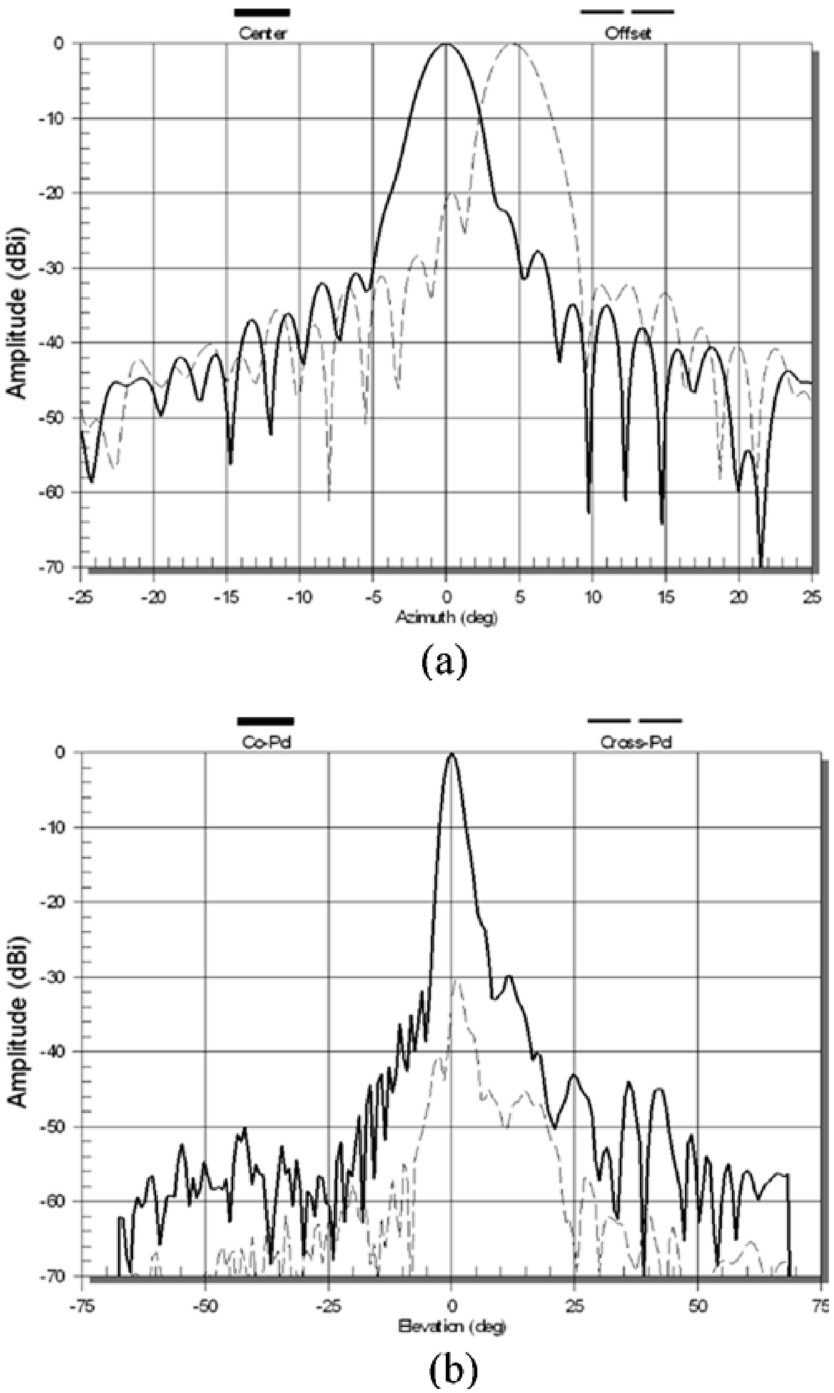

Figure 3.12. Near-field measurement of the twin feed horn with 60 cm reflector; (a) Frequency = 12.45 GHz, Polarization = Linear, azimuth cut, Center Beam Peak = -0.11°, offset Beam Peak = 4.43°, Beam Separation = 4.54°; (b) Frequency = 12.45 GHz, Polarization = Linear, elevation cut, -3 dB AZBW = 2.87°, Peak Gain = 35.62 dBi, El Peak = -0.32°, left sidelobe: -31.88 dBi, right sidelobe: -29.79 dBi.

III-4 Conclusion

In the design of multi-beam reflector antennas, it is essential to utilize CAD programs that take diffraction effects into account in order to accurately displace and allocate the utilized feed horns. Utilization of approximate BDF expressions could render pronounced beam pointing errors, especially for extreme defocusing distances. Additionally, the close proximity of the twin feed horn apertures may cause increased mutual coupling that could lead to significant performance degradation and beam asymmetries. Based on the theoretical and experimental investigation of the newly developed integrated twin feed horn structure, it was found that over 30 dB decoupling should be adequate to minimize such effects on the overall reflector antenna pattern. While the presence of the horn corrugation has helped in improving the overall dual feed horn performance, the use of a metallic diaphragm to separate the two apertures degrades the electrical performance (in the frequency range of 12.2 to 12.7 GHz). Our HFSS simulation results of the input match, decoupling, and cross polarization show that this wall could even lead to further performance degradation. It is noted that no pronounced degradation was noticed in both the input match and the radiation performance of the dual feed as compared to that of a single feed horn aperture performance. However, in the case of even narrower center-to-center feed horn spacing, the use of dielectrically loaded apertures should help in reducing the aperture size of these feed horns, thus minimizing the corrugation overlapping and eventually providing better decoupling.

CHAPTER IV
MIMO ANTENNA IN MOBILE LAPTOP SYSTEM

IV-1 Mobile antenna design trends

There is an increasing demand to combine computational and communication platforms. Intel Company and others are heavily involved in designing multi-functional chips that can facilitate such services for various platforms including laptops, PDAs, and cell phones. Addition of many services would mean the need to accommodate many services at different frequencies with different standards which would impact the design of their associated antennas, see table 4.1 for a list of current services. The simple and straightforward design is to use individual antennas to address these many services (figure 4.1). Such approach requires a large real-estate and cannot be implemented with the current trend in designing consumer type applications such as cell-phones or laptops where antennas generally must be compact and have extremely low profiles too. A second approach is to design multi-band antennas such that we can address many services with one antenna. This approach is very practical and is currently very popular. However, its wireless receiver is subject to collecting noise over the multi-band operation which still would lead to degrading the service quality and would significantly increase the complexity of the design of the receiver circuitry. A third approach that has been pioneered by our group here at the University of Tennessee is developing reconfigurable antennas or

Table 4.1. Mobile communication services and operation bands.

GSM/GPRS/EDGE	GSM 850 :0.824~0.894GHz GSM 900 : 0.88~0.96GHz DCS 1800 : 1.71~1.88GHz PCS 1900 : 1.85~1.99GHz
W-CDMA	UMTS : 1.92~2.17GHz
WLAN	IEEE 802.11b/g/n : 2.4GHz~2.48GHz IEEE 802.11a/n : 5.15GHz~5.85GHz
Bluetooth	IEEE 802.15.1 : 2.4GHz~2.48GHz (ISM)
GPS	1.575GHz
WiMAX	IEEE 802.16: 3.2-3.8GHz, 2.3-2.4GHz, 2.5-2.7GHz, 5.15-5.85GHz

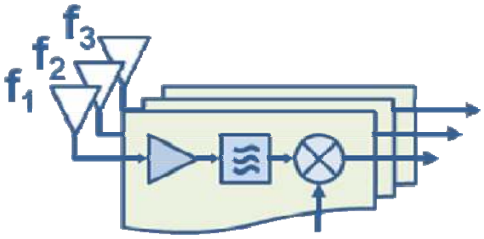

(a) Individual antenna system

(b) Multiband antenna

(c) Reconfigurable antenna

Figure 4.1. (a) Individual/separate antennas for each service, (b) multi-band antenna approach, (c) reconfigurable antenna where the antenna is tweaked to operate at f_1, f_2 or f_3.

even reconfigurable multi-band antennas [26,27]. This approach has a great potential to improve the receiver's performance upon reducing the input noise levels and is compliant with the need to have drastically reduced antenna sizes relative to the individual/separate antenna approach.

For laptop applications, however, the implementation of such antennas has slightly different issues that need to be addressed as well. There are plenty of potential spaces however, next to the keyboard and on the display cover that can be used for mounting these antennas. But there would be additional designs concerns such as: identifying the best antenna position on a laptop in terms of the optimum signal reception, the most suitable antennas for laptop application in the view of light weight, and low profile in general (table 4.2). The possibility of mounting multiple antennas on a laptop and the limitation of their number and spacing should be investigated as well. Use of multiple antennas with space diversity should enhance the overall performance.

Meanwhile, there are many types of antennas that could be used for wireless receivers, dipole, patch, wire, and dielectric resonator antennas are good examples. These various types are suited for single band operation, but can be easily re-designed for multi-band or reconfigurable operation. Patch and wire-antennas have been utilized to develop low profile structures suitable for laptop applications. [31-42] Therefore, there have been extensive research efforts to develop novel structures for both multi-band and reconfigurable operations. Figure 4.2 shows two novel structures that were developed by our group based on these structures —the nested patches and the mini-maze antennas [43,44].

Table 4.2. Various antenna properties in the laptop application. [28-30]

Type	Size	Bandwidth	Position	Description
Traditional slot and Patch	Very Large	Narrow	Surface of display	Possible only on the surface of lid due to their large size
Dipole and Sleeve dipole	Large	Moderate	Top of display	Dipole has wider BW than sleeve dipole, sleeve diploes are easy to use
Monopole and Helical	Large	Narrow	Top of display	Helical is small but narrower BW than monopole, difficult matching over the ISM band
	Small			
Inverted-F (INF)	Small	Wider than slot		Bandwidth, size, better overall performance than slot antenna
Ceramic chip	Very small	Very narrow		Small size (high ε_r), Helical or INF type, too narrow bandwidth

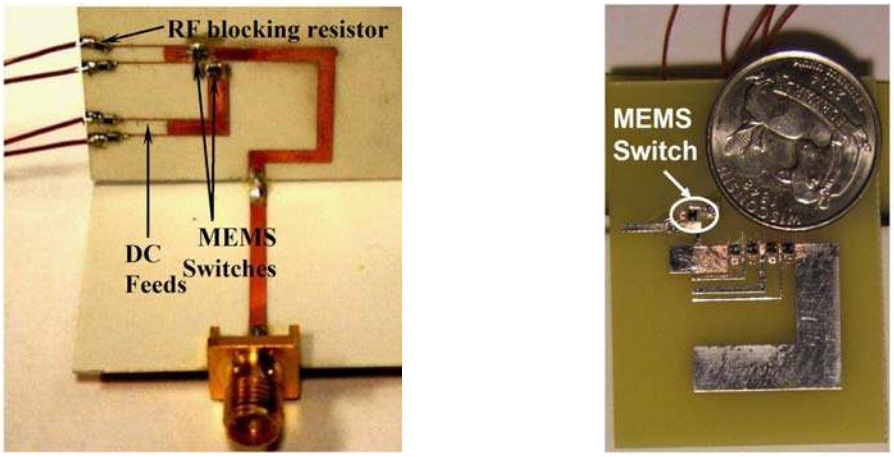

(a) Mini-maze reconfigurable antenna (b) Mini-nested reconfigurable patch

Figure 4.2. Novel reconfigurable antennas developed at UT a) the mini-maze, b) nested patch antenna.

One of the very popular antenna structures that is a derivative of the patch and wired antennas is the Planar Inverted-F Antenna (PIFA) structure. It is compact, low profile, and light weight structure. It can be utilized for a single or multi-band operation and can be additionally reconfigured using MEMS or PIN diodes. Figure 4.3 shows some pictures of novel PIFA antenna structure developed at UT for reconfigurable multi-band operation.

IV-2 Antennas for a Laptop System

Even though there are very limited spaces on laptops' platforms restricting the size of individual antennas, there is a room for more than one. Meanwhile, wireless traffic due to the increasing number of users, services and reflective hot spots easily explodes and falls short due to their limited channel capacities. However, recently multiple-input multiple-output (MIMO) concepts utilizing multiple antennas are being applied to cope with multi-fading, and reverberant wireless environments. Hence, more than one antenna as part of a MIMO system can be utilized to improve signal quality. Subsequently, antenna design and matching for MIMO application are no longer simple or deterministic because of the dynamic nature of their channel and required adaptive algorithms. Number, type, spacing, and relative orientation of these antennas have become of great concern and very challenging design issues in a laptop environment. [45-48]. In a MIMO system, using a larger number of utilized antennas leads to higher

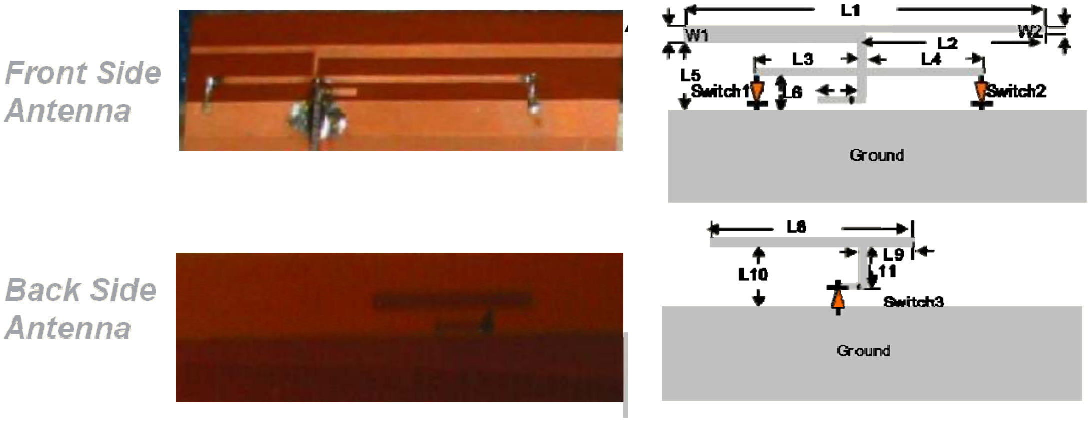

(a) Switching reconfigurable multi-branch PIFA antenna operating at 5 services (GSM/ DCS/UMTS/IMT-2000/WLAN) 7 frequency bands (800MHz, 900MHz, 1.8GHz, 2.1GHz, 2.4 GHz WLAN, and 5.2GHz) [26]

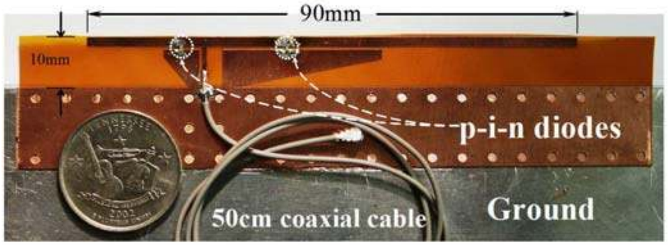

(b) Switchable twin PIFA multi-band antenna operating between WWAN (GSM850, PCS) and WLAN (IEEE 802.11b/g and 11a) [27]

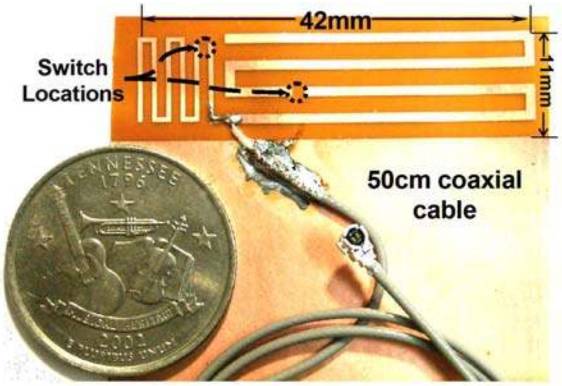

(c) The reconfigurable multi-band multi-branched monopole antenna [49].

Figure 4.3. Reconfigurable multi-band antennas developed at UT [26,27,49].

throughput capacity. Hence, there is a need to use the lowest possible antenna spacing to maximize the number of the utilized antennas mounted on a laptop platform. However, close spacing between the antennas would significantly increase their mutual coupling and would render them impractical for space diversity application. In this chapter, the relationship between the envelope correlation coefficient and both mutual coupling and input matching, and the effect of the antenna orientation configurations on these parameters will be discussed. The study is aimed at identifying the best antenna types, their optimum positions on the laptop chassis, and the minimal interspacing while sustaining adequate MIMO advantages.

IV-3 Test bed development

There have been extensive studies by G. Huff et al. [50] and D. Liu et al. [51], to identify the best antenna locations on a laptop platform. Investigated spots are ranked based on the received signal strength and these researchers have pointed out that the rim of the cover toward corner is the best place to receive/transmit signals from/to all directions. Other locations like the middle of the cover would obviously lead to radiation into only one direction operation because of the presence of the display shield behind the screen. Next to the keyboard is restricted again by the screen; however some vendors have utilized dipole antennas extending beyond the keyboard such as using PCMCIA card, but they are not embedded antennas.

Based on these studies we have developed two Novel designs that could tightly fit at/on the rim of the laptop's cover. These two simple linear PIFA structures have been designed for either a single frequency (2.4 GHz), or a dual frequency operation (2.4/5.2 GHz). They are printed on one side in 30x29.2 mm^2 on an epoxy substrate (FR-4, ε_r=4.8) with 64 mil thickness. Their overall dimensions and simulation results are shown in figure 4.4. These antennas have very low profiles and are limited to short-height and slim dimensions. To account for the laptop environment, the laptop was mocked up using metal plates as the back side of the LCD screen which is constructed from conductive metal to shield the radiations from various electronic circuits. The fabricated antennas were mounted on the mock up and placed in an anechoic chamber (Antenna Test Room at University of Tennessee) for full testing and evaluation as shown in figure 4.4 (c).

In the design of these antennas it is important to provide a good input match, wide angle coverage, an adequate bandwidth, and compliance with the size/volume of laptop rim's constraints. PIFA antenna with a flat profile is suitable for implementation on a laptop platform. Figure 4.4 shows our design that is mounted on a large ground-plane to emulate the laptop environment. Typical performance of such antenna is shown in figures 4.5 and 6, and shows measured and simulated results of both the input return loss and radiation pattern. Excellent agreement has been achieved with better than 25 dB return loss.

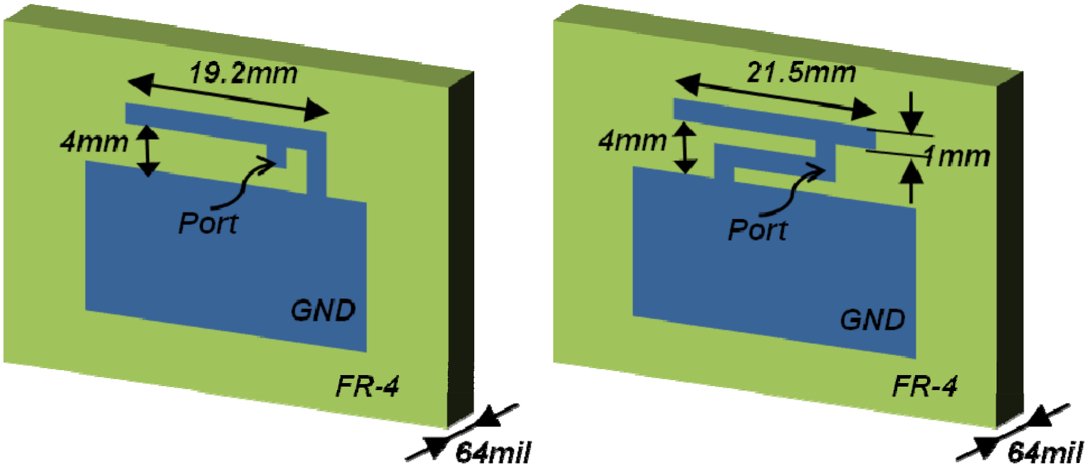

(a) Single-band (2.4 GHz) PIFA (b) Dual-band (2.4/5.2 GHz) PIFA

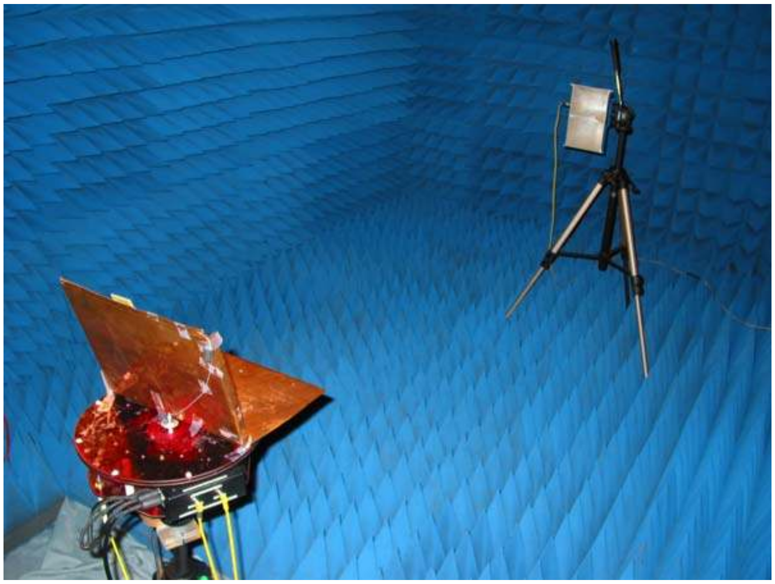

(c) Single-band PIFA mounted on laptop mock up and the radiation pattern was measured in anechoic chamber.

Figure 4.4. The developed antenna structure a) single-band, b) dual band. c) single-band antenna mounted on a laptop chassis and radiation pattern measurement performed in anechoic chamber.

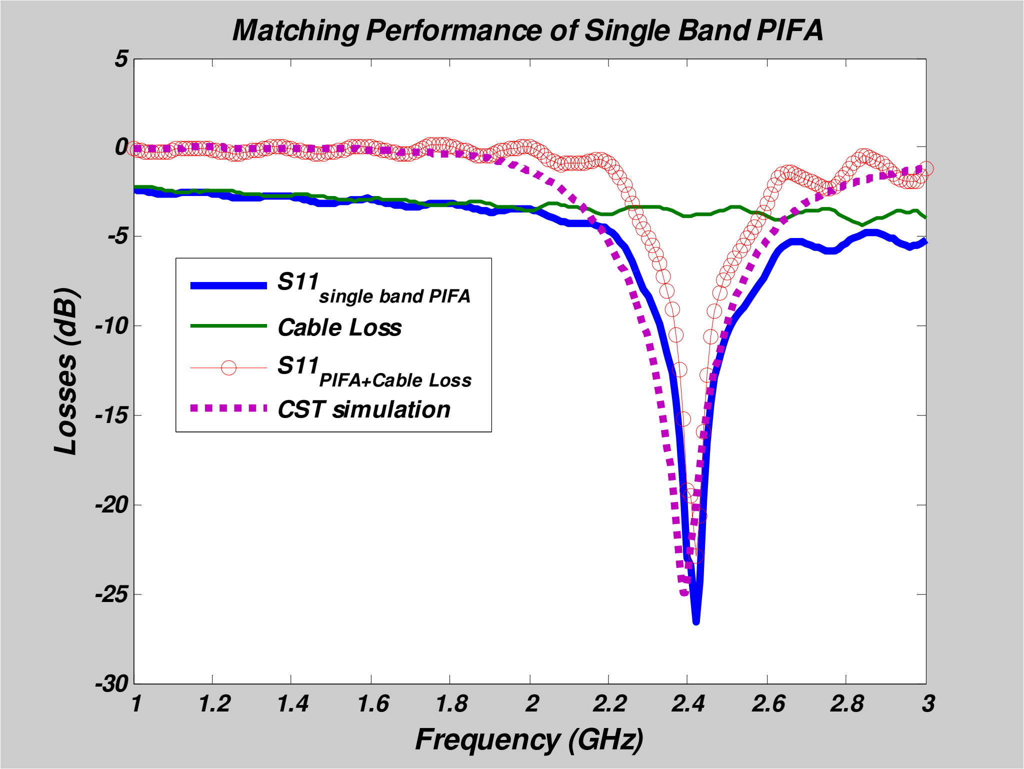

Figure 4.5. The input matching performance of single-band PIFA.

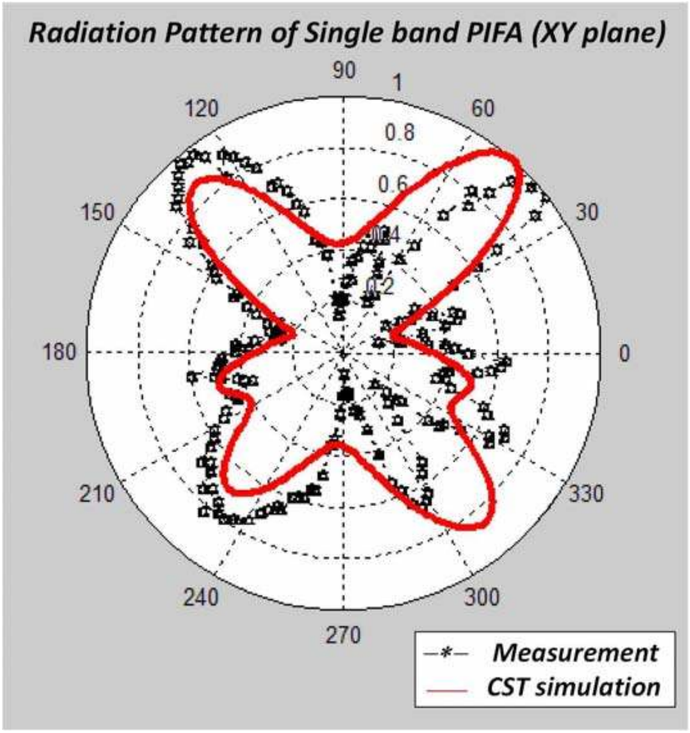

Figure 4.6. The radiation pattern of the single-band PIFA antenna.

The available space however is adequate for more than one antenna and can be utilized to address different services, i.e., different frequency bands or standards and different polarizations using individual antennas for example. These antennas, too, can be easily reconfigured to be optimized for these various services. They also can be combined to improve the overall system's performance, if they are part of Multi-Input Multi-Output (MIMO) system for diversity applications which could be either space or polarization diversity. In either case, it is important to determine the minimum distance between any two antennas to achieve an adequate decoupling which is sufficient for signals' de-correlation in a MIMO system.

IV-4 Antenna performance metrics for MIMO applications

A. Microwave Measurements Evaluation of Antennas' Decoupling:

The decoupling between the two previously designed PIFA antennas was evaluated as a function of their physical spacing. The two antennas were first placed at free space then mounted on a common ground plane to investigate the effect of the chassis' common ground plane. Figure 4.7 indicates that decoupling better than 12 dB can be achieved with a distance larger than 0.75λ (λ=125mm) in free space. However, the isolation between these two antennas becomes much weaker than that in free space when mounting both antennas on a common ground plane, a distance larger than 90 mm is required to achieve higher than 12 dB isolation. Increasing the distance to 180-mm will only lead to a 3 dB isolation improvement.

The previous simulations were carried out for a pair of PIFA antennas oriented in a certain configuration (defined later as collinear 3). However, it is believed that the orientation of these antennas can affect their decoupling performance. Hence, the above measurements were repeated for a set of various orientations given by collinear 1, collinear 2, and collinear 3 as shown in figure 4.8. The detailed dimensions and the measurement setup for mutual coupling evaluation between the antenna pairs are depicted in figure 4.9. In order to facilitate measuring their decoupling levels even for small distances, the two antennas were attached on both sides of the laptop mockup's screen that

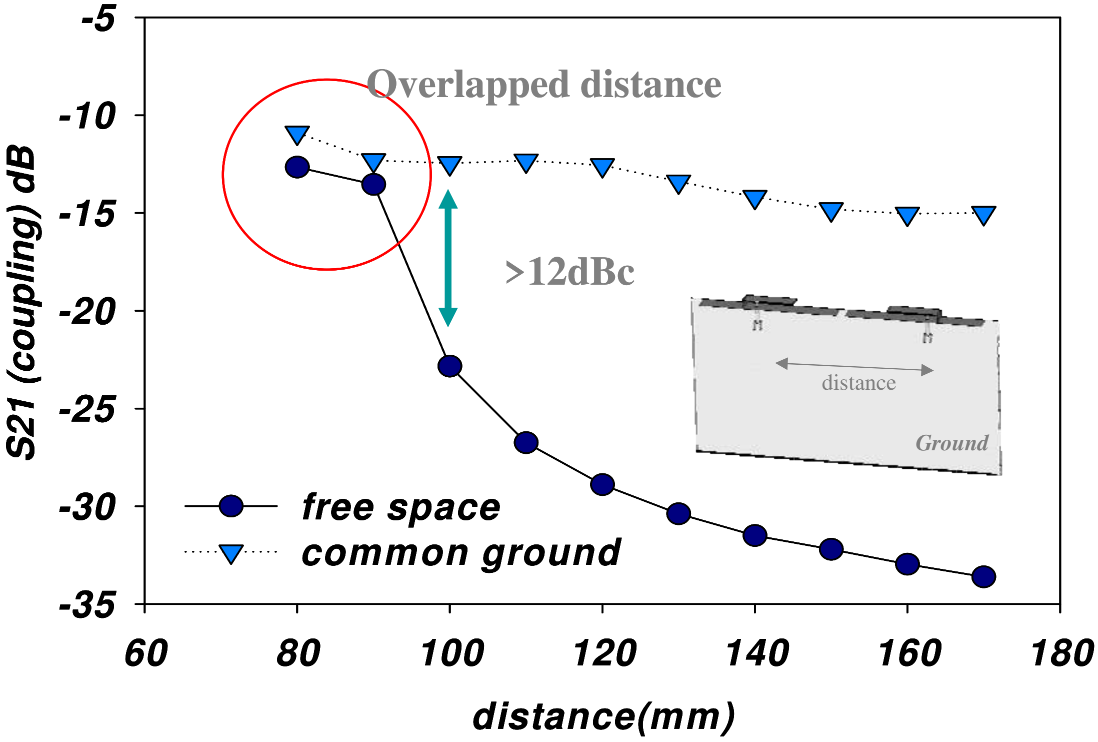

Figure 4.7. CST Microwave Studio^{TM} simulation results of the decoupling between two PIFA antennas placed on free space and when they are mounted on a common ground plane. (f=2.4GHz). The presence of the back side of the laptop display which is a conducting material acting as a common ground could lead to less decoupling between the two antennas. This effect is needed to be considered in designing the multi-element laptop antennas.

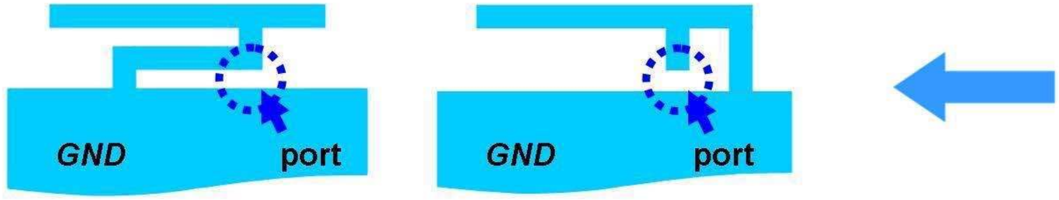

(a) Dual-band PIFA (b) Single-band PIFA (c) Symbol

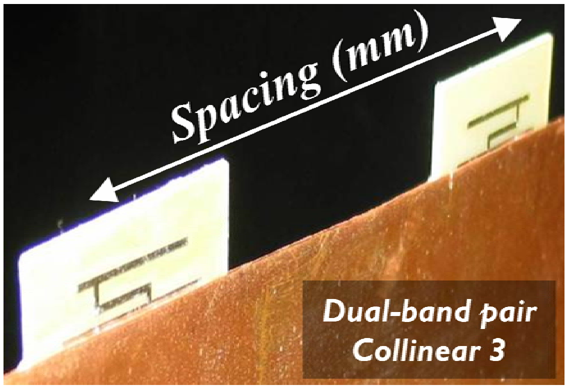

(d) Dual-band pair mounted on the laptop mock-up at the same side.

Figure 4.8. Dual-band and single-band PIFAs and a conceptual symbol. The arrowhead symbolizes the direction of the antenna arms away from the input port to the open end.

was emulated by a metal plate with a thickness of (d_x) 3 mm (0.024λ at f=2.4GHz). The spacing along the rim (d_y) was varied from 0 to 130mm (0~1.04λ).

In this experimental and theoretical study, we have used both single and dual band PIFA antennas to measure their decoupling performance as a function of their physical spacing and the study results are given in figure 4.10 and figure 4.11. Using tight spacing (<0.2λ) for all antenna types and orientations corresponds to strong coupling between the elements of > -10 dB. Meanwhile, it is apparent that collinear-3 orientation is relatively the worst, while collinear 2 is the preferred configuration of better than 15 dB decoupling for larger than 0.3λ. But, we still need more than 0.5λ for other orientations to achieve better than 15 dB isolation and the question now becomes: “Is 15-dB isolation acceptable for diversity utilization?” In addition to measuring the decoupling levels, we have monitored the antennas input match as shown in figure 4.12. It is also shown in figure 4.12 that strong coupling between antennas due to their close spacing lead to poor input return loss performance: It is clear that the input match even for a single element while the other antenna is match terminated could be less than 3-dB for spacing less than 0.2λ. Obviously, the input match is a function of the differential phase between the two antenna pairs and can be extremely poor and would lead to poor efficiency due to re-radiation and poor reception. Collinear-2 configuration with spacing greater than 0.3λ has better than 6-dB input-match which could be sufficient-- as will be discussed in the next sections.

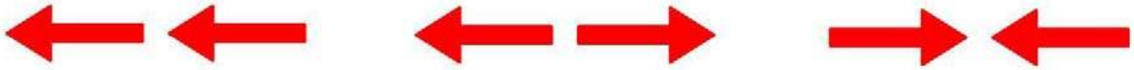

(a) Collinear 1 (b) Collinear 2 (c) Collinear 3

Figure 4.9. Three different symbolic configurations of identical antenna pairs. Collinear 1 represents the antenna pair with same direction, collinear 2 is for back to back configuration and collinear 3 represents that open ends of antennas are facing each other as shown in figure 4.8(d).

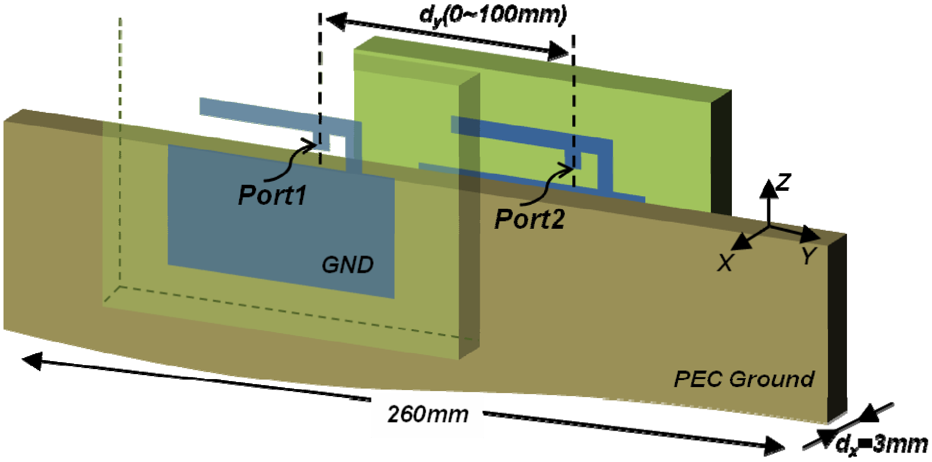

(a) Mounting method on the PEC laptop model for simulation and measurement.

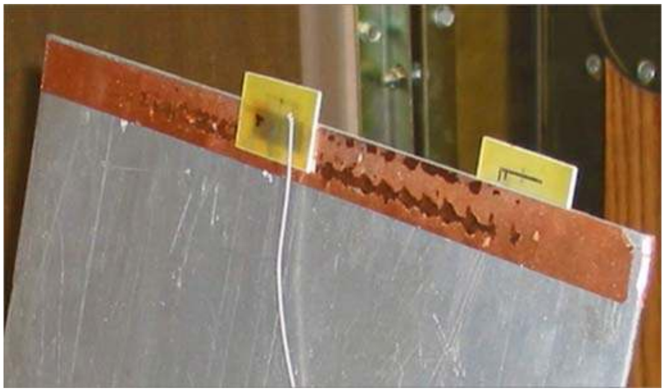

(b) Single-band (Inverted-F) pair mounted on laptop mock up: the thickness of the metal plate is 3 mm (0.024λ at f=2.4GHz)

Figure 4.10. Detailed dimensions of single-band PIFA collinear 1 pair. Two antennas are separated in x and y directions. (d_x: thickness of the metal plate as screen part of laptop mockup). So the antennas are physically separated even by a small distance (d_y).

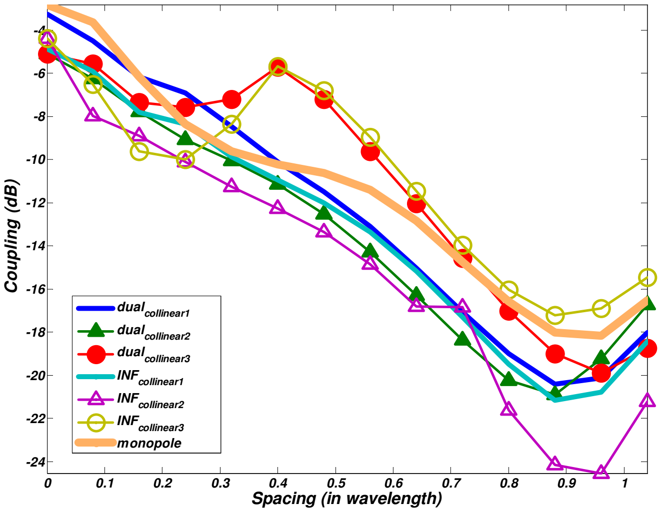

(a) CST simulation on various antennas and their configurations

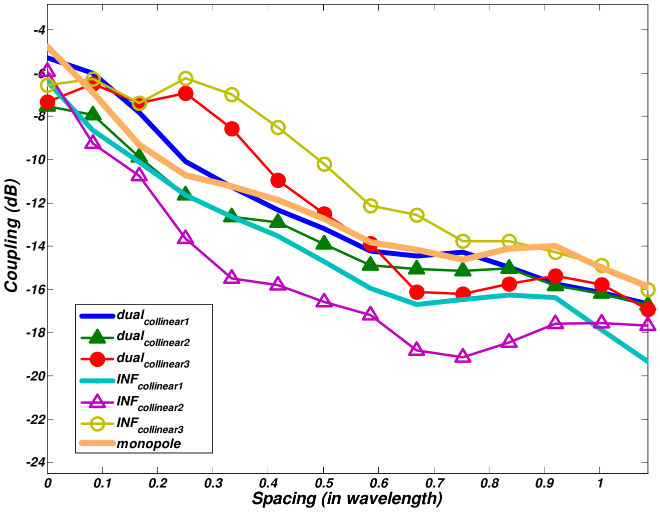

(b) Measured mutual coupling between inverted-F antenna pairs.

Figure 4.11. The decoupling performance of the three different configurations. Collinear 3 configuration has the poorest isolation performance compared to collinear 1 and 2, Better than 10 dB decoupling can be achieved for element spacing about 0.3~0.4λ. However collinear 2 configuration has consistently lower coupling for the same physical spacing between the two antennas.

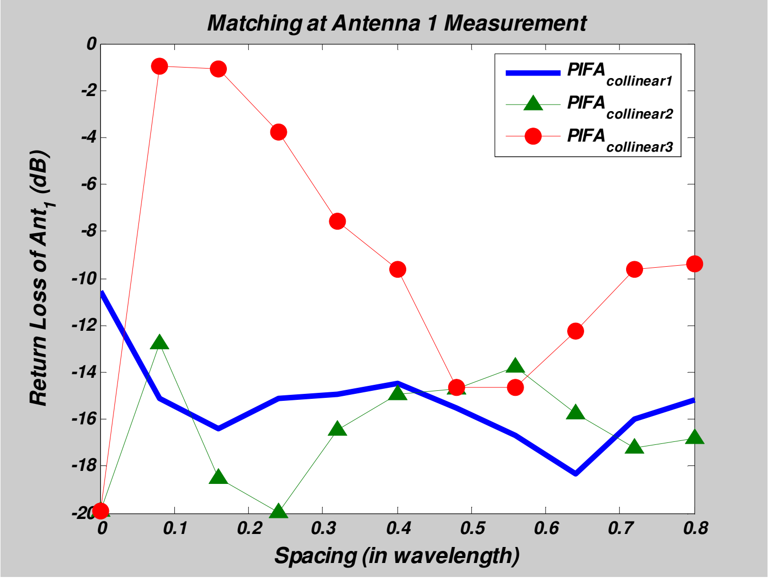

(C) Measured input matching performance at antenna 1.

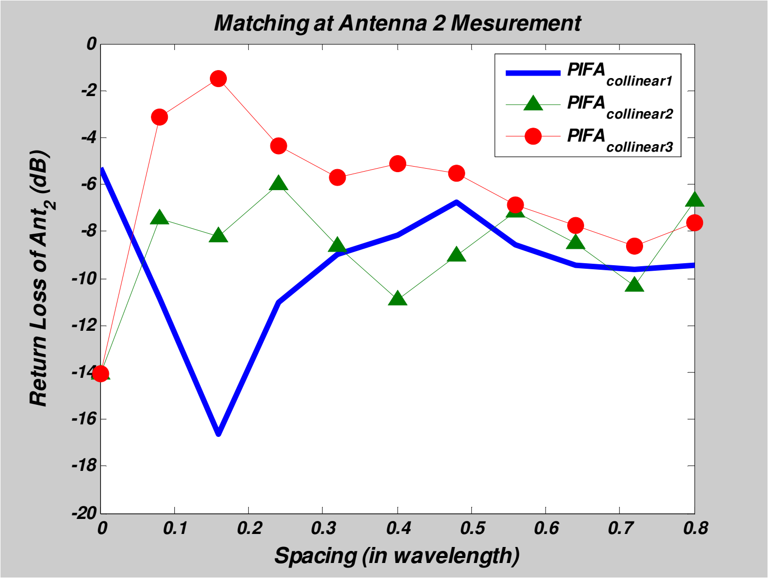

(d) Measured input matching performance at antenna 2.

Figure 4.12. Matching performance of the various configurations. Collinear 3 configuration has extremely poor match at an element spacing of about 0.1~0.2λ, again collinear 2 configuration has consistently less coupling and better input match for the same spacing and it is our preferred configuration.

However, such distances are still relatively large and would lead to limitations in the number of potentially utilized antennas. Hence, it is essential to look for the real minimum distance between the antenna pairs for both the diversity and MIMO applications.

To visualize the effect of mutual coupling between antenna pairs and relate that to their MIMO performance, we initially evaluated the effect of the mutual coupling between two monopole antennas on their radiation patterns as a function of their physical separation distances. The radiation pattern of a monopole antenna element was evaluated while the other element is match-terminated. Similar analysis was then carried out for other configurations as well (see Appendix B). From the simulations of the embedded element radiation patterns of monopole and single band PIFA (Inverted-F antenna) pairs, it is apparent that strong coupling between the two antennas can significantly degrade the overall performance when the spacing between the two antennas is less than 0.2λ. Configuration collinear 2 has relatively less physical spacing sensitivity as compared to all other configurations, which is consistent with our previous conclusions (based on the isolation and match) demonstrated performance in figures 4.11 and 12. Meanwhile, less coupling and sensitivity to the physical spacing between the two antennas can be noticed for 0.2λ~0.6λ especially for configuration collinear 2.

To summarize our findings at this point, increasing the spacing obviously increases the decoupling between the antenna pairs for any configuration, while decreasing their spacing lower than 0.2λ can seriously affect match and individual radiation patterns in the presence of the other due to the strong mutual coupling. So, the remaining questions here are: “What is really the adequate distance to be useful in a laptop implementation?”, “What is the minimum distance to be sufficient for MIMO application?” In the following section, we will first give a background on MIMO systems and then second will determine the minimum spacing required between the antennas to achieve a high throughput capacity in a MIMO system based on a new metric--the envelope correlation coefficient related to the measured radiation patterns.

B. Envelope correlation coefficient (ρ_e)

Background: Employing Multi-Input Multi-Output (MIMO) into wireless communication systems is the recently proposed solution for multi-path multi-fading wireless environment. Many researches and projects are being focused on this area from different points of views. When it departs from deterministic approaches, the correlation functions of the different channels are required. It is necessary to estimate the system performance such as the channel capacity and diversity gain to relate the signal correlation concepts to antenna or system performance indexes. In order to do this, the envelope correlation coefficient (ρ_e) can be determined by using the far-field radiation pattern function. In most locations of wireless laptop use (in indoor situations) can be represented by a ***uniform angular distribution of the received signals.*** This assumption is extremely important to simplify the estimation of the correlation coefficient using either S-parameters or radiation field patterns. [52-55]. The envelope correlation coefficient can be calculated using the far-field radiation pattern as given [53],

$$\rho_e = \frac{\left| \iint_{4\pi} [\boldsymbol{F_1}(\theta,\phi) \bullet \boldsymbol{F_2}(\theta,\phi)] d\Omega \right|^2}{\iint_{4\pi} \left| \boldsymbol{F_1}(\theta,\phi) \right|^2 d\Omega \iint_{4\pi} \left| \boldsymbol{F_2}(\theta,\phi) \right|^2 d\Omega} \tag{4.1}$$

where $\boldsymbol{F}_{\mathrm{i}}(\upsilon,\phi)$ is the field radiation. In the assumption of ***a lossless system (the energy conservation law)*** and ***uniform probability distributions of arriving angles***, meanwhile the exact representation of the envelope correlation coefficient of any two antennas for N antenna system using S-parameters becomes [54],

$$\rho_e(i,j,N) = \frac{\left| \sum_{n=1}^{N} S_{i,n}^{*} S_{n,j} \right|^2}{\prod_{k=i,j} \left[1 - \sum_{n=1}^{N} S_{k,n}^{*} S_{n,k} \right]} \tag{4.2}$$

Based on the above analysis, we have employed the above two expressions to calculate the envelope correlation coefficient for the different types of antenna pairs using both far-field computations and S-parameters evaluations. Figure 4.13 shows the envelope correlation coefficients for both the monopole antennas and the PIFAs (inverted-F), where excellent agreement between its estimated values based on both the S-parameters and the far field calculations is demonstrated. The comparison was carried out using the two different methods of the envelope correlation calculations for all cases: collinear 1, collinear 2, and collinear3, in addition to the monopole-pair. In the case of a two-antenna system,

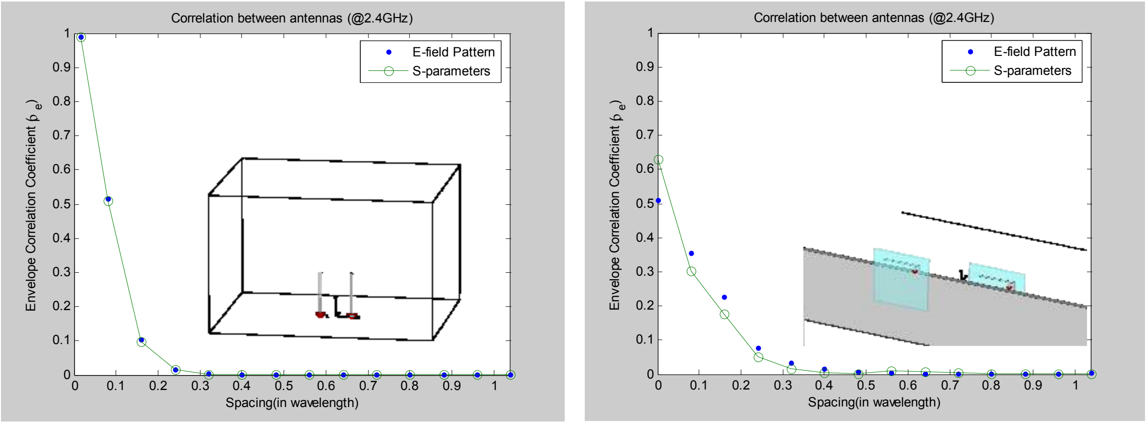

(a) Monopole pair (b) Single-band PIFA pair in collinear 1

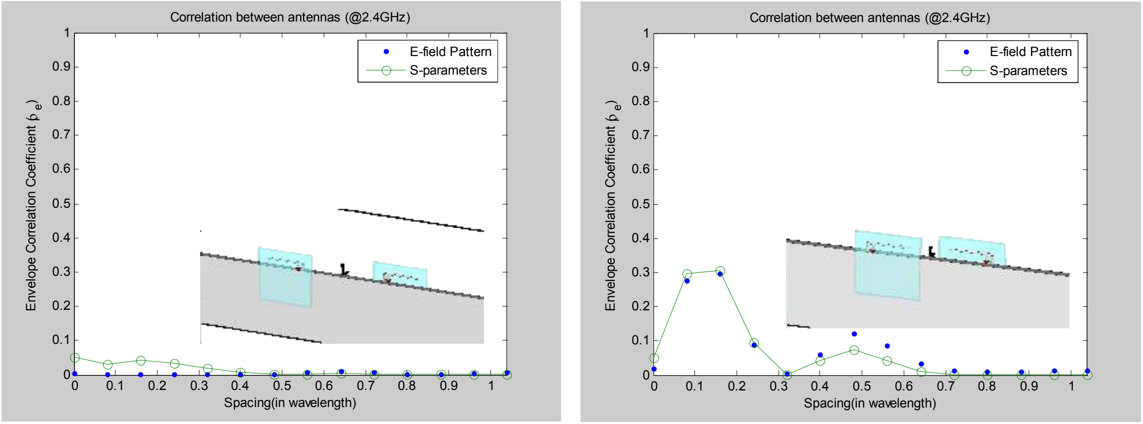

(c) Single-band PIFA pair in collinear 2 (d) Single-band PIFA pair in collinear 3

Figure 4.13. Envelope correlation coefficient calculations based on the simulations of radiation patterns (equation 4.1) and S-parameters (equation 4.2) of (a) monopole pair, and three different configurations of single-band PIFA pairs; (b) collinear 1, (c) collinear 2, (d) collinear 3 (refer to figure 4.8 and 4.9 and see Appendix B).

the maximum correlation coefficient ($\rho_{e,\max}$) can be expressed, [55] (see Appendix A)

$$\rho_{e,\max} = \left| \frac{2|S_{11}||S_{12}|}{1-\left(|S_{11}|^2+|S_{12}|^2\right)} \right|^2 \tag{4.3}$$

where $|S_{11}|=|S_{22}|$ and $S_{12}=S_{21}$. It gives the relation between the input match (S_{ii}), the coupling (S_{ij}) to the correlation coefficient. Figure 4.14 indicates the maximum allowable coupling (x-axis) under a given match condition and a correlation level. For example, if the matching of antenna input terminals is kept at S_{ii} =-7dB, then it is allowed to have a coupling value up to -7dB-- as long as the correlation coefficient is less than 0.7.

It is well-known that for various communication systems, that the acceptable ρ_e coefficient is less than 0.7 for a useful MIMO system [52]. Whatever is used to calculate the ρ_e coefficient, we need to determine the minimum acceptable physical spacing between the antennas while sustaining an acceptable ρ_e coefficient to be < 0.7. Figure 4.15 shows the correlation coefficient of the designed single and dual-band PIFA pairs as a function of the physical spacing between the elements. It is clear, if we assume a good input match, then even with a small spacing, almost touching each other (<0.1λ), between the antennas, low correlation coefficients can be achieved. But, this is impractical and unacceptable as strong mutual coupling would lead to poor match (as seen in figure 4.12), and practically stronger radiation pattern dependency, as well.

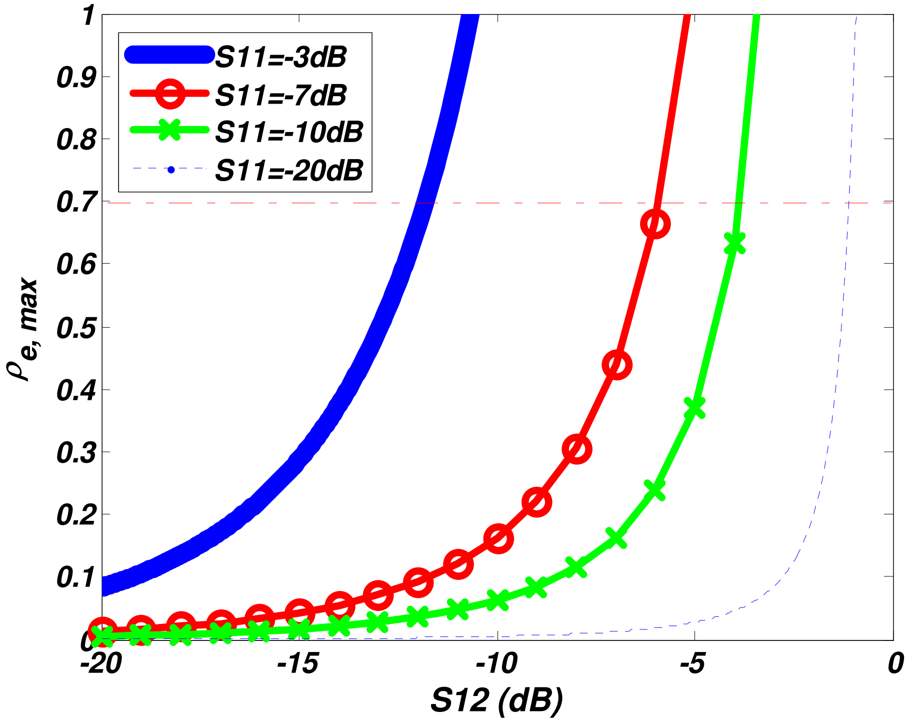

Figure 4.14. The envelope correlation coefficient versus coupling for a given input/output matching condition. Each curve represents a different input matching condition, and the maximum envelope correlation coefficient is calculated based on equation (4.3) as a function of the coupling coefficient S_{12}. This graph shows the ideal case that the matching and coupling can be controlled independently; however, they are interactively affecting each other [55].

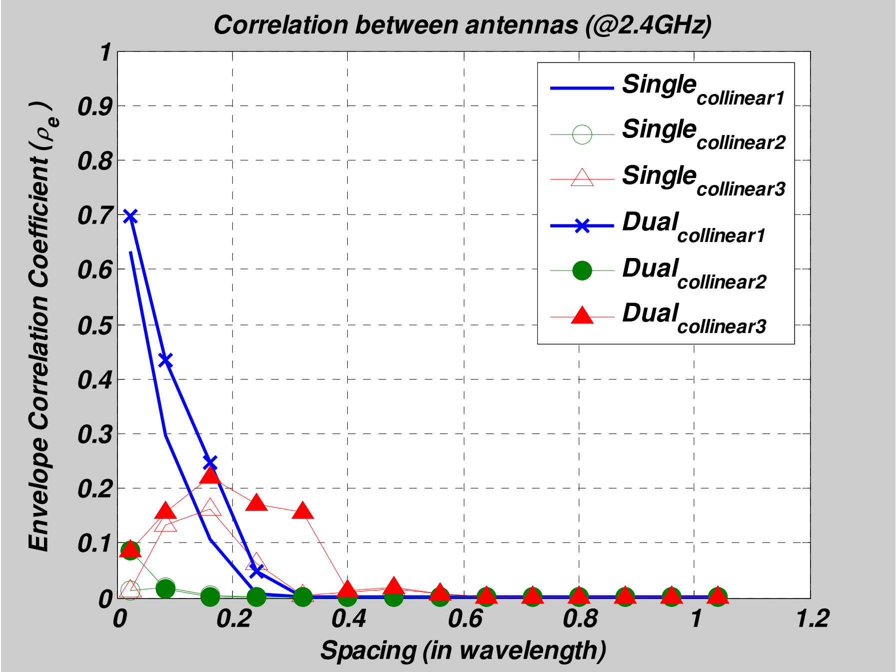

Figure 4.15. Envelope correlation coefficient of different collinear configurations of single and dual-band PIFAs.

Very strong performance dependence on the differential phase between the antenna pairs which would significantly affect the radiation efficiency as seen in the next section.

C. Radiation efficiency based on the power reflection ratio evaluation

The correlation coefficient is a normalized value and does not include the radiation efficiency-- which is another metric to determine acceptable minimum antenna spacing. Therefore, we need to calculate the radiation efficiency (represented by the reflected power factor) as a function of the input match while achieving an envelope correlation coefficient of <0.7. In order to clearly explain the radiation efficiency in terms of the S-parameters, the radiated power in a lossless antenna system can be represented as [56],

$$\mathbf{P}_{\mathbf{rad}} = \mathbf{I} - \mathbf{P}_{\mathbf{refl}} = \mathbf{I} - \mathbf{S}^{\mathbf{H}}\mathbf{S} = \mathbf{F}^{\mathbf{H}}\mathbf{F} \tag{4.4}$$

where P_{rad} and P_{refl} are radiated and reflected power rate matrices respectively (figure 4.16). The elements of S-parameter matrix both terminal matching (S_{ii}) and mutual coupling coefficients (S_{ij}) represent overall reflection from the antenna input terminal. And the mean reflected power ratio $<P_{refl}/P_{in}>$ is defined as,

$$\left\langle P_{refl} / P_{in} \right\rangle = \frac{1}{N} \sum_{i,j=1}^{N} \left| S_{ij} \right|^2 \tag{4.5}$$

where N is the number of antenna elements. This ratio given in (5) indicates the total reflected power normalized with respect to the input power to the antenna system. And the minimum value of the mean reflected power ratio occurs at a level defined by the ***critical mismatching condition***, and is given by:

$$\text{Critical mismatching condition: } \left|S_{ii}\right| = \left|S_{ij}\right| = \left|S\right| \quad (i, j = 1 \cdots N). \tag{4.6}$$

Then the correlation coefficient and minimum reflected power respectively become:

$$\text{Correlation coefficient: } \rho_{e,\max} = \left| \frac{N\left|S\right|^2}{\left|1 - N\left|S\right|^2\right|} \right|^2 \tag{4.7}$$

$$\text{Minimum mean reflected power: } \left\langle P_{refl} / P_{in} \right\rangle_{\min} = N\left|S\right|^2. \tag{4.8}$$

Some examples under critical mismatching conditions are shown in table 4.3 and figure 4.17.

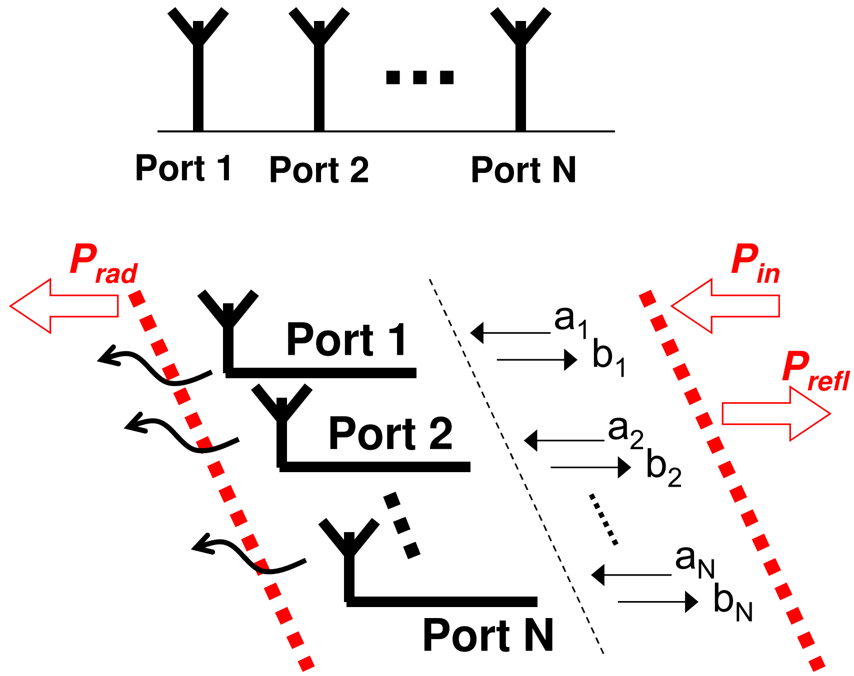

Figure 4.16. A diagram of the signal power flow in the multiple antenna system. P_{in} is the input, P_{refl} is reflected back to system, and P_{rad} is radiated power. In a lossless antenna system, the total radiated power is the difference between P_{in} and P_{refl}.

Table 4.3. Minimum power reflection and correlation coefficients based on critical mismatching cases (equations 4.6-4.8)

$\rho_{e,max}$	$\langle P_{refl}/P_{in}\rangle_{min}$	**|S|** *(N=2)*
0.7	0.46	0.48(-6.4dB)
0.5	0.42	0.46(-6.8dB)
0.3	0.36	0.42(-7.5dB)
0.06	0.2	0.32 (-10dB)
0.005	0.06	0.18 (-15dB)

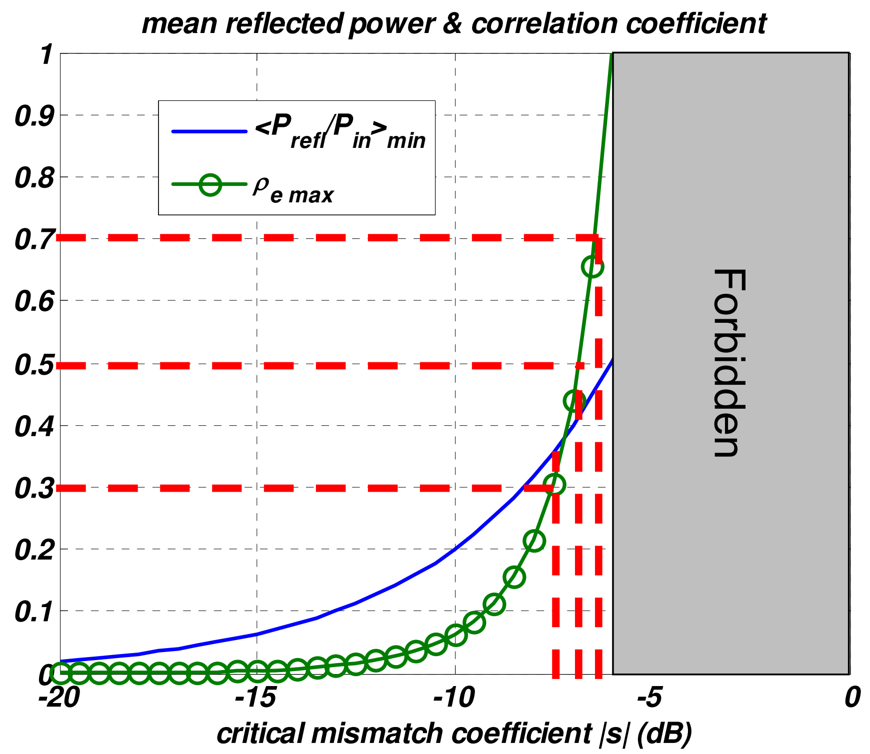

Figure 4.17. Graph (green) is the correlation coefficient vs. critical mismatch (the maximum allowed S_{11}) to achieve certain max. correlation coefficient. Graph (blue) is the minimum normalized reflected power ratio vs. critical mismatch, where we will use ρe max of 0.7, then this will be translated to ~-6 dB critical mismatch and 0.5 power coefficient will be reflected. In this case, 50% of the power will be radiated. In case of $|S_{11}|=|S_{21}|=|S_{12}|=|S_{22}|=0.5$, there is no radiation from the antenna system as indicated by the 'forbidden' region on the above graph. [56].

The mean reflected power ratios (equation 4.5) were calculated based on the S-parameters of our designed single and dual band PIFA pairs in figure 4.18. Unlike the minimum reflected power-ratio under critical mismatching condition, the mean reflected power ratio could be up to 1. In the case that it reaches 1, all the incident power will be completely reflected back to the system, in other words, no power radiation. Once the element spacing between antennas become more than 0.6λ, any of the antenna pairs have less than 10% of reflection (i.e. 90% of radiation). The collinear3 pairs radiate only less than 10% and 20% for single band and dual band PIFA respectively at a spacing around 0.3λ. And the collinear2 pairs have the least power reflection among the configurations, less than 40% even at very small distances as seen in figure 4.18.

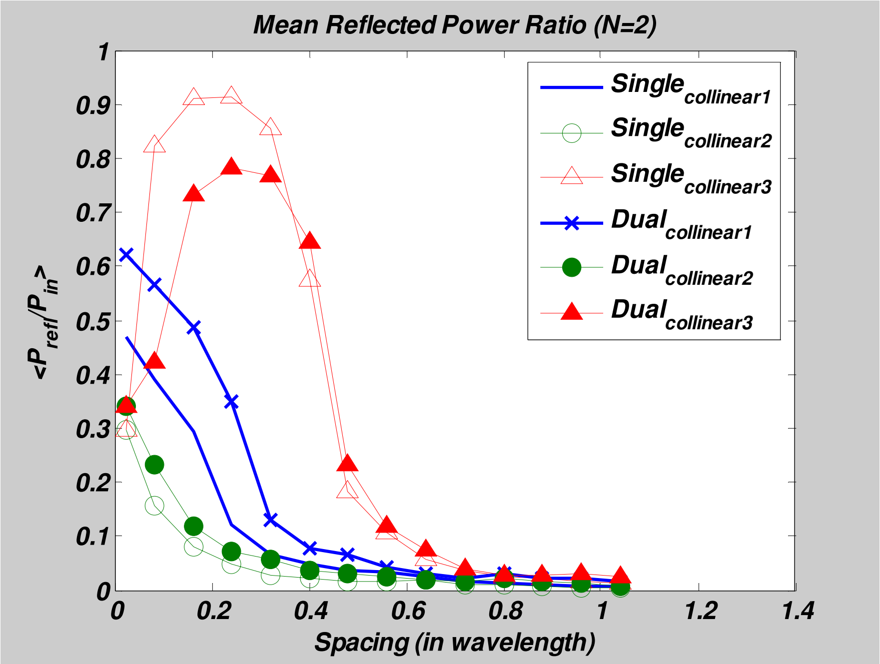

Figure 4.18. Mean relative reflected power ratio calculated from designed antennas in different collinear configurations based on equation 4.5.

Applying the above concepts which can be implemented in two steps:

1) Achieve less than 0.7 correlation coefficient by selecting certain spacing
2) Then validate that the selected spacing is adequate for good match, adequate isolation, and low reflected power as indicated by figure 4.18.

For example, based on figure 4.15 we can practically select any spacing between the two antennas for all configurations and still can achieve a correlation coefficient less than 0.7, but this is not the complete picture as it is still essential to calculate the effect of mutual coupling between the elements on their match and the subsequent radiation efficiency as related to the mean reflected power ratio. So, for configuration 1 and 2 with spacing larger than 0.2λ we can achieve at least 50% radiation efficiency (i.e., <0.5 mean reflected power rate), while for collinear configuration 3 it is required to space the two antennas based on figure 4.18 at a distance $> 0.4\lambda$.

IV-5 Implementation in an indoor environment

In order to verify our findings and studies on the antenna configuration pairs, we selected two possible environment scenarios; indoor and hallway static situations. We have implemented a simple MIMO system and the setups are depicted in figures 4.19 and 4.20 respectively. In general, it is anticipated that using the MIMO system we will lead to much lower fading levels as compared using to conventional links.

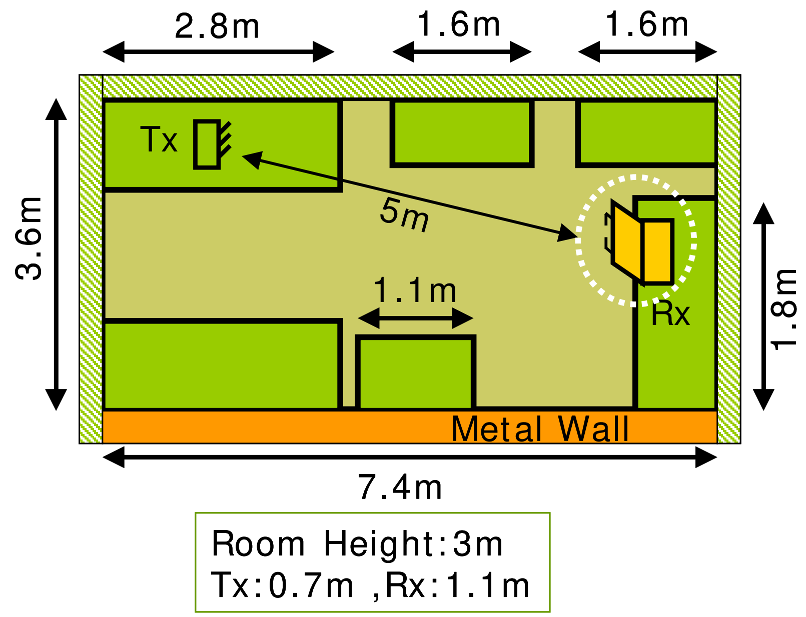

Figure 4.19. Layout and dimensions of indoor scenario for MIMO antenna measurement. Transmitting antennas are 3 sleeve dipoles, and receiving antennas are single-band PIFA collinear configuration pairs.

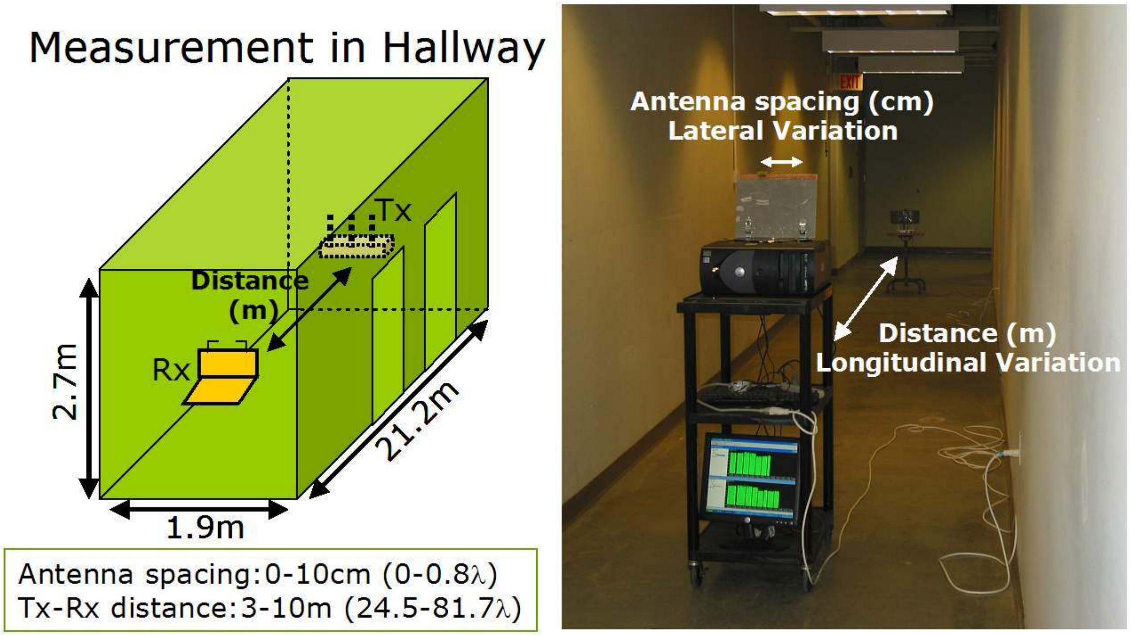

Figure 4.20. Measurement setup in a corridor scenario. The longitudinal distance between Tx and Rx varies from 24~80λ and lateral variation between single band PIFA is 0~0.8λ.

A. Indoor MIMO performance (small room)

We have mounted the various antenna configurations on the rim of a laptop mockup as a part of a MIMO enabled wireless link. Three-sleeve dipoles were used as transmitting antennas, while a pair of the single band PIFA (2.4GHz) antennas was used in the receiver side. For the transmitting and receiver units, we selected a commercial MIMO wireless access point, D-Link Xtreme N^{TM} DIR-655, and DWA-552 wireless adapter respectively. The received signal strength was collected and *averaged* using NetStumbler 4.0 software [60]. We subsequently carried out extensive measurements of the received signals as a function of the distance between the transmitter and the receiver. Typically for transmit/receive units with a single element (i.e., conventional systems not in a MIMO one) the received signals can undergo fading levels as high as 60 dB [57] due to multi-path effects. However, based on our measurements, it is clear that the MIMO system with adequate spacing between the antennas would suffer from much lower fading levels (~10 dB) for the various configurations as seen in figure 4.21. Meanwhile, fading levels are significant and even the received power levels on the average are relatively much lower when the antenna pairs are placed within a distance $<0.1\lambda$ for all configurations due to the strong mutual coupling and its impact on the effectiveness of the MIMO system for such close antenna spacing. Meanwhile, collinear 1 and 2 MIMO configurations start to be effective as their signal strength peaks at antenna spacing around 0.25λ, while the collinear 3 start to be effective beyond 0.35λ spacing. This is consistent with

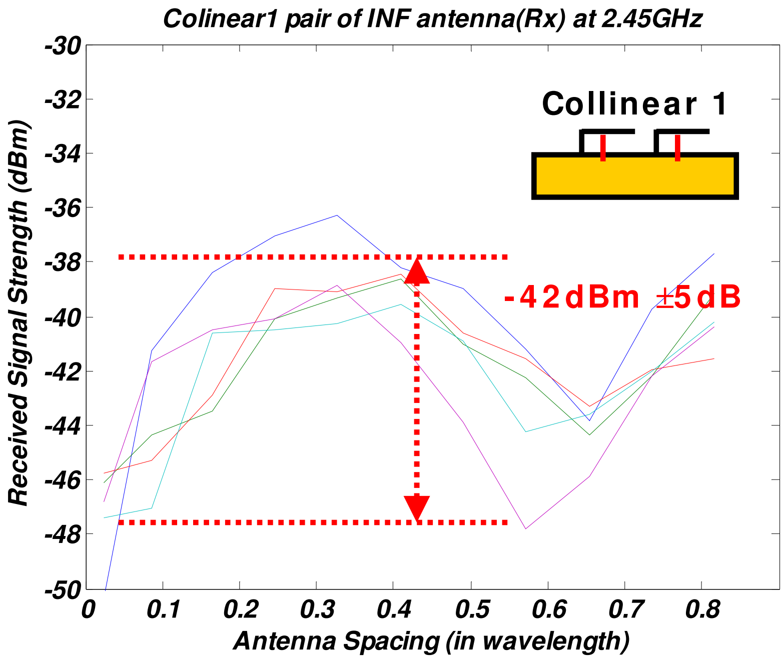

(a) Single band PIFA collinear 1 pair

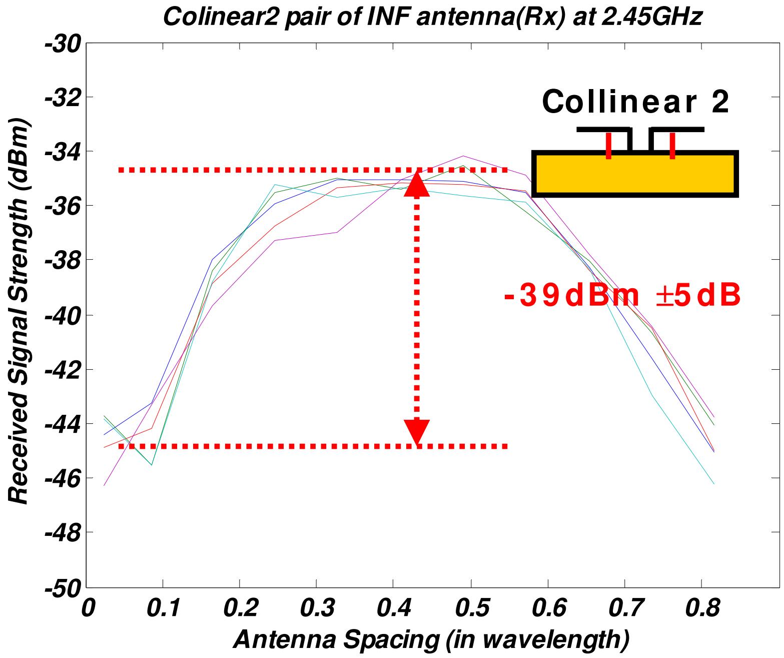

(b) Single band PIFA collinear 2 pair

Figure 4.21. Received signal strength measurement results on the single band PIFA pairs at indoor 3з2 MIMO scenario.

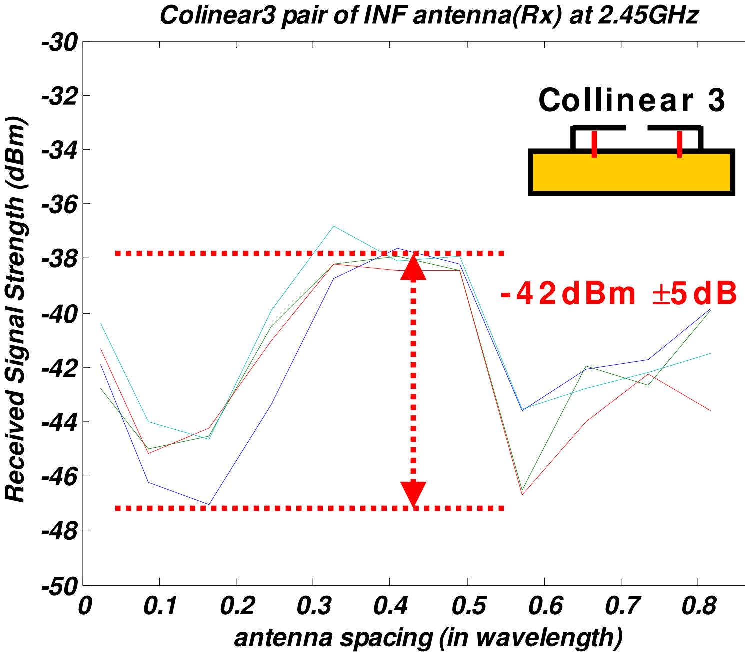

(c) Single band PIFA collinear 3 pair

Figure 4.20. Continued.

the adequate spacing required to practically demonstrate the merits of operating in a MIMO system.

B. Hallway measurements

We have also carried out similar set of measurements in a static hallway scene. Figure 4.22 shows that the received signal is generally high around 0.25λ to 0.5λ spacing and the variations of the signal levels are still around ±5dB. Higher fading levels, as anticipated, have been seen for spacing less than 0.1λ.

IV-6 Conclusion

There are generally two factors that need to be considered to determine the minimum spacing between the two antenna pairs for an effective MIMO system. These factors are the envelope correlation coefficient and the active power reflection ratio. The envelope correlation coefficient can be determined either by the radiation patterns or the system's S-parameters under certain conditions. S-parameters, however, is much easier to be utilized. It turned out from figure 4.15, that it is adequate to physically space the two antennas to the point that they are not overlapping. This would still provide envelope correlation coefficients less than 0.7. Based on the critical mismatching factor for an acceptable power reflection coefficient, the minimum spacing between the two antennas should be as low as 0.2λ for collinear 1 and 2, and 0.4-0.5λ for

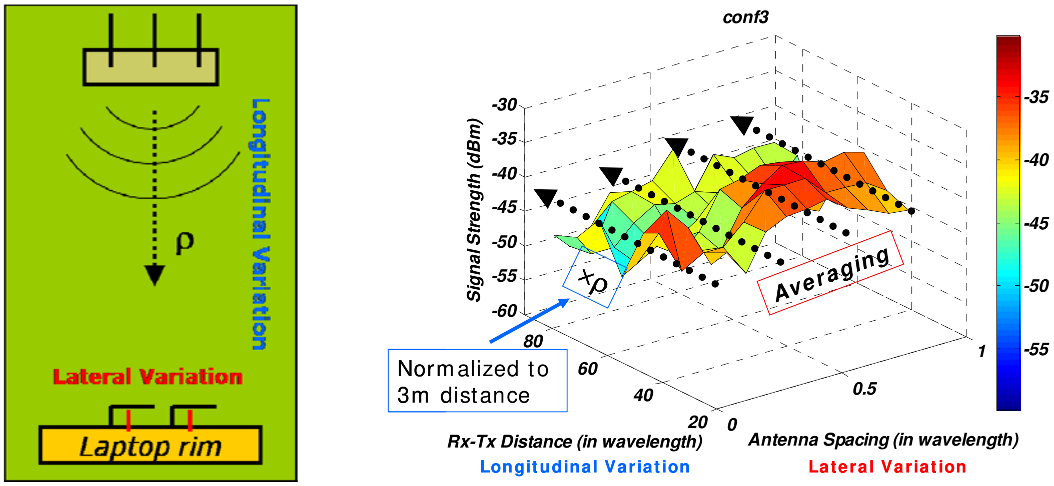

(a) Simplified propagation (b) Standing wave behavior compensation

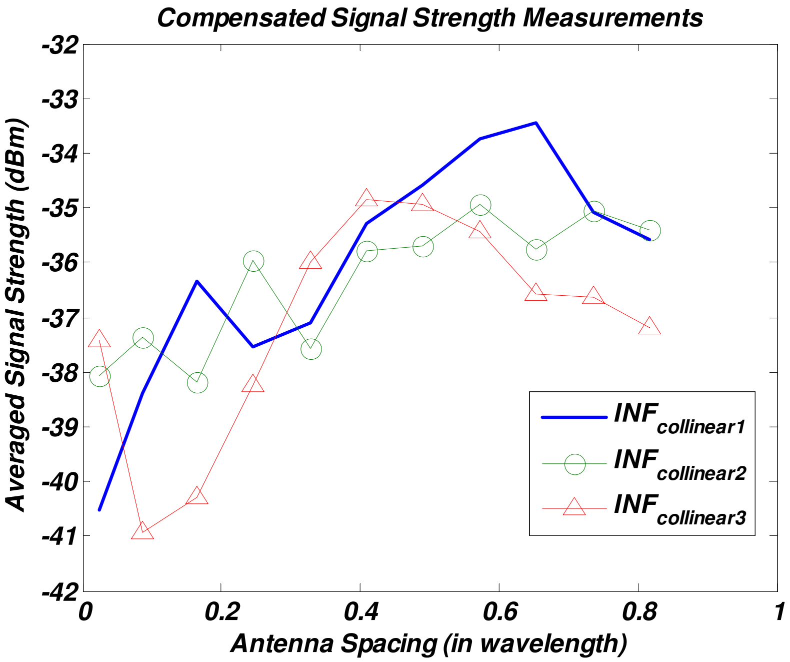

(c) The average signal strength after the standing wave compensation with cylindrical propagation assumption

Figure 4.22. Signal strength measurement in hallway. (figure 4.21 for setup)

collinear 3. In other words, a typical spacing of 0.25λ can be used for most antennas in a MIMO system, here we show that for configuration 1 and 2 a 0.25λ is adequate, but for configuration 3 if this spacing is used then the radiation efficiency would be < 30%, and their spacing should be > 0.4λ to achieve relatively higher radiation efficiency as can be seen in figure 4.18.

CHAPTER V
CONCLUSIONS AND RECOMMENDATIONS

The simple and general radial combiner design steps may be applied to design similar N-way radial microstrip combiner structures. The developed approximate design method has been validated using both equivalent circuit and HFSS modeling.

The structure has excellent graceful degradation performance and the use of these isolation resistors can help in minimizing the effect of higher order modes generated from the structure asymmetry due to its manufacture or use of unbalanced amplifiers.

In the design of multi-beam reflector antennas, it is essential to utilize CAD programs based on geometrical/physical optics to accurately account for the feedhorns defocusing effects. Utilization of approximate BDF expressions could render pronounced beam pointing errors, especially for slight or very large defocusing distances. Additionally, the close proximity of the twin feed horn apertures may cause increased mutual coupling that could lead to significant performance degradation and radiating beams asymmetries. Based on the theoretical and experimental investigation of the developed integrated twin feedhorn structure, it was found that over 30 dB decoupling should be adequate to minimize such effects on the overall reflector antenna pattern. While the presence of the horn corrugation can help in improving the overall dual feed horn performance, the use of a metallic diaphragm to separate the two apertures degrades the electrical performance (in the frequency range of 12.2 to 12.7 GHz) and does not help. In the case of even narrower center-to-center feed horn spacing, the use of dielectrically loaded apertures could help in reducing the aperture size of these feed horns, thus minimizing the corrugation overlapping and eventually providing better decoupling.

There are generally two factors need to be considered to determine the minimum spacing between the two antenna pairs for an effective MIMO system. These factors are the envelope correlation coefficient and the active power reflection ratio. The envelope correlation coefficient can be determined either by the radiation patterns or the system's S-parameters. It turns out from figure 4.15, that it is adequate to physically space the two antennas to the point that they are not overlapping but would still provide envelope correlation coefficients less than 0.7. Meanwhile, based on the critical mismatching factor for an acceptable power reflection coefficient, the minimum spacing between the two antennas should be as low as 0.2λ for collinear 1 and 2, and 0.4-0.5λ for collinear 3. In other words, a typical spacing of 0.25λ is used for most antennas in a MIMO system, here we show that for configuration 1 and 2 a 0.25λ is adequate, but for configuration 3 if this spacing is used then the radiation efficiency would be < 30%, and their spacing should be > 0.4λ to achieve relatively higher radiation.

LIST OF REFERENCES

LIST OF REFERENCES

Chapter 2

[1] X. Jiang, S. Ortiz, A. Mortazawi,” A novel Ka-band 1 to 8 power divider/ combiner,” 2001 IEEE MTT-S Int. Microwave Symp. Dig., vol.1, pp. 35, June 2001.

[2] K. Russell, Microwave Power Combining Techniques, IEEE Trans. MTT-27, pp. 472-478, May, 1979.

[3] S. Foti, 60-Way Radial Combiner Uses no, Isolators, Microwaves and RF, pp. 96-118, July, 1984.

[4] E. Belohoubek, R. Brown, H. Johnson, A. Fathy, D. Bechtle, D. Kalokitis, E. Mykietyn “30-Way Radial Power Combiner for Miniature GaAs FET Power Amplifiers,” *1986 IEEE MTT-S Int. Microwave Symp. Dig.*, vol. 86, Issue 1, pp. 515-518, June 1986.

[5] A. E. Fathy, D. Kalokitis, “ Analysis and Design of a 30 way radial combiner for Ku-band applications,” RCA Review, Vol. 47, Dec. 1986, pp. 487-508.

[6] A. G. Williamson, “Radial line/coaxial line stepped junction,” *IEEE Trans. Microwave Theory & Tech.,* vol. 33, (1), pp. 56, January 1985.

[7] N. Marcuvitz, Waveguide Handbook, Vol. 10, MIT Rad. Lab. Ser., New York, McGraw Hill, 1951.

[8] M. Cohn, B.D. Geller, and J. M. Schellenberg, A 10-Watt Broadband FET, Combiner/Amplifier, 1979 IEEE MTT-S Int. Microwave Symp. Dig. VOL. 79, Issue 1, pp. 292-297, June 1979.

[9] A. E. Fathy, S. W. Lee, D. Kalokitis," Simplified approach for the design of radial power combining structures," 2004 IEEE MTT-S Int. Microwave Symp. Dig., vol.1, pp. 73-76, June 2004.

[10] R. L. Ernst, R. L. Camisa, and A. Presser, "Graceful degradation properties of matched N-port power amplifier combiners," in *IEEE MTT-S Int. Microwave Symp. Dig.*, June 1977, pp. 174-177.

[11] A. A. Saleh, "Improving the graceful-degradation performance of combined power amplifiers," IEEE Trans. Microwave Theory Tech., vol. MTT-28, pp. 1068-1070, Oct. 1980.

[12] D. B. Rutledge, N. –S Cheng, R. York, R. M Weikle, M. P. De Lisio, "Failures in power-combining arrays," *IEEE Trans. Microwave Theory & Tech.*, vol. 47, No. 7, July 1999, pp. 1077-1082.

Chapter 3

[13] P. J. B. Clarricoats and G. T. Poulton, "High-efficiency microwave reflector antennas-a review," *Proc. IEEE*, vol. 65, no. 10, pp. 1470–1504

[14] Y. T. Lo and S. W. Lee, Eds., *Antenna Handbook Vol. II: Antenna Theory*. New York: Van Nostrand Reinhold, 1993.

[15] A. W. Rudge, Ed. *et al., The Handbook of Antenna Design*. London, U.K.: Peter Peregrinus, 1982, vol. 1.

[16] Y. Rahmat-Samii, P. Cramer, Jr., K. Woo, and S. W. Lee, “Realizable feed-element patterns of multibeam reflector antenna analysis,” *IEEE Trans. Antennas Propag.*, vol. AP-29, pp. 961–963, Nov. 1981.

[17] Y. T. Lo, “On the beam deviation factor of a parabolic reflector,” *IRE Trans. Antennas Propag.*, vol. AP-8, pp. 347–349, May 1960.

[18] J. Ruze, “Lateral-feed displacement in a paraboloid,” *IEEE Trans. Antennas Propag.*, vol. AP-13, pp. 660–665, Sep. 1965.

[19] W. A. Imbriale, P. G. Ingerson, and W. C. Wong, “Large lateral feed displacements in a parabolic reflector,” *IEEE Trans. Antennas Propag.*,vol. AP-22, pp. 742–745, Nov. 1974.

[20] R.Wohlleben *et al.*, “Two primary focus feeds for dual-beam operation in reflector antennas,” in *Proc. Antennas and Propagation Society Int. Symp.*, 1975, pp. 387–390.

[21] GRASP8 Student ed. TICRA Copenhagen, Denmark.

[22] *“HFSS (High Frequency Structure Simulator),”* ver. 10, Ansoft Corp., May 2003.

[23] Near-Field Systems 2001 [Online]. Available: http://www.nearfield.com/catalog 2001

[24] Software de Análisis de Bocinas y Reflectores (Horns and Reflectors Analysis Software), version 1.1, E.T.S.I. de Telecomunicación Universidad Politécnica de Madrid, Feb. 1998.

[25] T. H. Lee and R. C. Rudduck, “Numerical Electromagnetic Code – Reflector Antenna Code, NEC-REF (Version 3),” The Ohio State University ElectroScience Laboratory, Feb. 1994.

Chapter 4

[26] Chunna Zhang, Songnan Yang, Sung-Woo Lee, Samir El-Ghazaly, Aly E. Fathy, Helen K. Pan and Vijay K. Nair, “A Low Profile Twin-PIFA Laptop Reconfigurable Multi-band Antenna for Switchable and Fixed Services Wireless Applications,” *IEEE/MTT-S International Microwave Symposium*, pp. 1209-1212, Jun. 2007.

[27] Songnan Yang, Aly E. Fathy, Samir M. El-Ghazaly and Vijay K. Nair, “Novel Reconfigurable Multi-band Antennas for Multi-radio Platforms,” *IEEE Radio and Wireless Symposium*, pp. 723-726, Jan. 2008.

[28] D. Liu, E. Flint, and B. Gaucher, "Integrated Laptop Antennas - Design and Evaluations," *in Proceedings of the IEEE APS International Symposium and URSI Radio Science Meeting*, San Antonio, TX, June 16-21,2002, vol. 4, pp.56-59.

[29] S. B. Yeap, X. Chen, J. A. Dupuy, C. C. Chiau and C. G. Parini, “Integrated Diversity Antenna for Laptop and PDA Terminal in a MIMO System,” *IEE Proc. Microwave Antenna Propagation*, vol. 152, No. 6, Dec. 2005.

[30] Kin-Lu Wong, Liang-Che Chou and Chih-Ming Su, “Dual-Band Flat-Plate Antenna with a Shorted Parasitic Element for Laptop Applications,” *IEEE Trans. on Antennas and Propagation*, vol. 53, No. 1, Jan. 2005.

[31] Duixian Liu and Brian Gaucher, “Performance Analysis of Inverted-F and Slot Antennas for WLAN Applications,” *IEEE/AP-S International Symposium*, pp. 14-17. June 2003.

[32] Duixian Liu and Brian Gaucher, “A New Multiband Antenna for WLAN/Cellular Applications,” *IEEE Vehicular Technology Conference*, vol. 1, pp. 243-246, Sep. 2004.

[33] Duixian Liu and Brian Gaucher, “The Inverted-F Antenna Height Effects on Bandwidth,” *IEEE/AP-S International Symposium*, pp. 367-370, July 2005.

[34] Duixian Liu, Brian Gaucher and Thomas Hildner, “A Dualband Antenna for WLAN Applications,” *IEEE International Workshop on Antenna Tech.*, pp. 201-204, Mar. 2005.

[35] Zhi Ning Chen, Duixian Liu and Brian Gaucher, “A Planar Dualband Antenna for 2.4 GHz and UWB Laptop Applications,” *IEEE Vehicular Tech. Conf.*, vol. 6, pp. 2652-2655, 2006.

[36] Zhi Ning Chen, Duixian Liu, Brian Gaucher and Thomas Hildner, “Reduction in Antenna Height by Slotting Ground Plane,” *IEEE International Workshop on Ant. Tech. Small Antennas and Novel Metamaterials*, pp. 25-28, Mar. 2006.

[37] Zhi Ning Chen, Duixian Liu and Brian Gaucher, “Low-Profile Embedded Ultra-Wideband Antennas for Portable Devices,” *Proc. EuCAP 2006* 6-10 Nov. 2006.

[38] Chih-Ming Su, Hong-Twu Chen, Fa-Shian Chang and Kin-Lu Wong, “Dual-Band Slot Antenna for 2.4/5.2 GHz WLAN Operation,” *Microwave and Optical Tech. Letters*, vol. 35, No. 4, Nov. 20 2002.

[39] Kin-Lu Wong and Liang-Che Chou, “Internal Wideband Metal-Plate Antenna for Laptop Application,” *Microwave and Optical Tech. Letters*, vol. 46, No. 4, Aug. 20. 2005.

[40] Keisuke Fukuchi, Yuuki Yamamoto, Kenichi Sato, Ryo Sato and Hisachi Tate, “Wide-Band Wireless LAN Antenna for IEEE 802.11a/b/g,” *Hitachi Cable Review* No. 23, Aug. 2004.

[41] Young Jun Cho, Young Sun Shin and Seong-Ook Park, “Dual-Band Internal WLAN for 2.4/5 GHz Laptop PC Applications,” *Microwave and Optical Tech. Letters*, vol. 48, No. 11, Nov. 2006.

[42] Tatsuhiko Ito, Hiroshi Moriyasu and Masayuki Matsui, “A Small Antenna for Laptop Applications,” *IEEE International Workshop on Ant. Tech. Small Antennas and Novel Metamaterials* , pp. 233-236, Mar. 2006.

[43] Songnan Yang, Helen K Pan, Aly E. Fathy, Samir El-Ghazaly and Vijay K Nair, "A Novel Reconfigurable Maze Antenna for Multiservice Wireless Universal Receivers, " *IEEE Radio and Wireless Symposium*, San Diego, Jan. 2006.

[44] Chunna Zhang, Songnan Yang, Helen K Pan, Aly E. Fathy, Samir El-Ghazaly, Vijay K. Nair, "Development of Reconfigurable Mini-Nested Patches Antenna for Universal Wireless Receiver Using MEMS, " *IEEE 2006 AP-S/URSI/AMEREM*, Albuquerque, July. 2006.

[45] H. Carrasco, H. D. Hristov, R. Feick and D. Cofré, “Mutual Coupling Between Planar Inverted-F Antennas”, *Microwave and Opt. Tech. Letters*, vol. 42, No. 3, pp. 224-227, Aug. 2004.

[46] J. Thaysen and Kaj B. Jakobsen, “Design Considerations for Low Antenna Correlation and Mutual Coupling Reduction in Multi Antenna Terminals,” *Europ. Trans. on Telecomms.*, pp. 319-326, vol. 18, 2007.

[47] Samuel C. K. Ko and Ross D. Murch, “A Diversity Antennas for External Mounting on Wireless Handsets,” *IEEE Trans. Antennas and Propag.*, vol. 49, No. 5, pp. 840-842, May 2001.

[48] Jon W. Wallace and Michael A. Jensen, “Mutual Coupling in MIMO Wireless Systems: A Rigorous Network Theory Analysis,” *IEEE Trans. on Wireless Comm.*, vol. 3, No. 4, pp. 1317-1325, July 2004.

[49] Songnan Yang, Aly E. Fathy, Samir El-Ghazaly, Helen K. Pan and Vijay K. Nair , “A NOVEL HYBRID RECONFIGURABLE MULTI-BAND ANTENNA FOR UNIVERSAL WIRELESS RECEIVERS,” *International URSI Electromagnetic Theory Symposium*, July 2007.

[50] G. H. Huff, J. Feng, S. Zhang, G. Cung, and J. T. Bernhard, “Directional Reconfigurable Antennas on Laptop Computers: Simulation, Measurement

and Evaluation of Candidate Integration Positions," *IEEE Trans. Antenna and Propag.*, vol. 52, No. 12, pp. 3220-3227, Dec. 2004.

[51] D. Liu, B. P. Gaucher, E. B. Flint, T. W. Studwell, H. Usui and T. J. Beukema,"Developing Integrated Antenna Subsystems for Laptop Computers," *IBM Journal of Research and Development*, vol. 47, no. 2/3, MARCH/MAY 2003

[52] R. G. Vaughan and J. B. Andersen, "Antenna Diversity in Mobile Communications," *IEEE Trans. Veh. Technol.*, vol. 36, pp. 149-172, Nov. 1987.

[53] S. Blanch, J. Romeu and I. Corbella, "Exact representation of antenna system diversity performance from input parameter description," *Electr. Lett.,* vol. 39, no. 9, pp. 705-707, May 2003.

[54] J. Thaysen and K. B. Jakobsen, "Envelope Correlation in (N,N) MIMO Antenna Array from Scattering Parameters,"*Microwave and Opt. Tech. Letters*, vol. 48, No. 5, pp. 832-834, May 2006.

[55] I. Salonen, P. Vainikainen, "Estimation of signal correlation in antenna arrays," in *Proceedings of JINA 2002 International Symposium on Antennas*, Nice, France, 2002, vol. 2, (ISSN 1168-3848), pp. 383−386.

[56] I. Salonen, C. Icheln, and P. Vainikainen, "Pattern Correlation and Mismatch in Two-Element Antenna Arrays," *Microwave and Opt. Tech. Letters*, vol. 48, No. 1, pp. 41-43, Jan. 2006.

[57] Henry L. Bertoni, *Radio Propagation for Mordern Wireless Systems,* Prentice Hall PTR, NJ, 1999.

[58] R. Vaughan, J. B. Andersen, *Channels, propagation and antennas for mobile communications*, Institution of Electrical Engineers, 2003

[59] Hon Tat Hui, W. T. Ow Yong and K. B. Toh, “Signal Correlation Between Two Normal-Mode Helical Antennas for Diversity Reception in a Multipath Environment,” *IEEE Trans. on Antennas and Propag.*, vol. 52, No. 2, pp. 572-577, Feb. 2004.

[60] http://www.netstumbler.com/

APPENDICES

Appendix A. Envelope Correlation Coefficient

Envelope correlation coefficient can be calculated using the far-field radiation pattern as given [53],

$$\rho_e = \frac{\left| \iint\limits_{4\pi} [\boldsymbol{F_1}(\theta,\phi) \bullet \boldsymbol{F_2}(\theta,\phi)] d\Omega \right|^2}{\iint\limits_{4\pi} \left| \boldsymbol{F_1}(\theta,\phi) \right|^2 d\Omega \iint\limits_{4\pi} \left| \boldsymbol{F_2}(\theta,\phi) \right|^2 d\Omega} \tag{A.1}$$

where $\boldsymbol{F}_i(\upsilon,\phi)$ is the field radiation pattern of the antenna and $\bullet$ denotes the Hermitian product.

$$\boldsymbol{E} = \boldsymbol{E_1} + \boldsymbol{E_2} = a_1 \sqrt{\frac{\eta D_1}{4\pi}} \boldsymbol{F_1}(\theta,\phi) \frac{e^{-jkr}}{r} + a_2 \sqrt{\frac{\eta D_2}{4\pi}} \boldsymbol{F_2}(\theta,\phi) \frac{e^{-jkr}}{r} \tag{A.2}$$

The total radiated power from the antenna system is

$$P = \frac{1}{\eta} \iint \left| \boldsymbol{E} \right|^2 dS = \frac{1}{\eta} \iint \left(\left| \boldsymbol{E}_1 \right|^2 + \left| \boldsymbol{E}_2 \right|^2 + \boldsymbol{E}_1 \bullet \boldsymbol{E}_2 + \boldsymbol{E}_2 \bullet \boldsymbol{E}_1 \right) dS \tag{A.3}$$

If we define the complex constants C_{11}, C_{12}, C_{21} and C_{22} as

$$C_{ij} = \frac{\sqrt{D_i D_j}}{4\pi} \iint \left(\boldsymbol{F}_i \bullet \boldsymbol{F}_j \right) d\Omega, \quad d\Omega = dS / r^2, \quad i, j = 1, 2 \tag{A.4}$$

Then the total radiated power can be represented by,

$$P = C_{11} \left| a_1 \right|^2 + C_{12} a_1 a_2^* + C_{12} a_2 a_1^* + C_{22} \left| a_2 \right|^2 = \mathbf{a}^* \mathbf{C} \mathbf{a} \tag{A.5}$$

where **a** is the column vector of a_1 and a_c and **C is** the correlation matrix.

In a lossless system, under the energy conservation law, the radiated power can be expressed by S-parameters under the assumption of uniform probability distributions of arriving angles,

$$P=\sum_{i=1}^{2} a_i-\sum_{i=1}^{2} b_i=\mathbf{a}^*\mathbf{a}-\mathbf{b}^*\mathbf{b}=\mathbf{a}^*\left(\mathbf{I}-\mathbf{S}^*\mathbf{S}\right)\mathbf{a} \tag{A.6}$$

where **I** is the identity matrix and **S** the S-parameter matrix. The above two equations yield **C=I-S*****S** and the exact representation of envelope correlation coefficient of any two antennas for N antenna system using S-parameters becomes [54],

$$\rho_e(i,j,N)=\frac{\left|\sum_{n=1}^{N} S_{i,n}^* S_{n,j}\right|^2}{\prod_{k=i,j}\left[1-\sum_{n=1}^{N} S_{k,n}^* S_{n,k}\right]} \tag{A.7}$$

For two antenna system, the correlation coefficient can be expressed [55]

$$\begin{aligned}\rho_e&=\frac{\left|S_{11}^*S_{12}+S_{21}^*S_{22}\right|^2}{\left(1-\left(\left|S_{11}\right|^2+\left|S_{21}\right|^2\right)\right)\left(1-\left(\left|S_{22}\right|^2+\left|S_{12}\right|^2\right)\right)}\\&=\frac{\left|S_{12}\right|^2\left|S_{11}\right|^2\left[1+k^2+2k\cos(\varphi_1+\varphi_2)\right]}{\left(1-\left(\left|S_{11}\right|^2+\left|S_{21}\right|^2\right)\right)\left(1-\left(\left|S_{22}\right|^2+\left|S_{12}\right|^2\right)\right)}\end{aligned} \tag{A.8}$$

where $S_{12}=S_{21}$, $S_{11}^*S_{12}=\left|S_{11}\right|\left|S_{12}\right|e^{j\varphi_1}$, $S_{22}^*S_{12}=\left|S_{22}\right|\left|S_{12}\right|e^{j\varphi_2}$ and $\left|S_{22}\right|=k\left|S_{11}\right|$. For symmetric identical antenna pair, k=1 and $\varphi_1=\varphi_2$, then (4.2) becomes [55],

$$\rho_e=\left|\frac{2\left|S_{11}\right|\left|S_{12}\right|\cos 2\varphi_1}{1-\left(\left|S_{11}\right|^2+\left|S_{12}\right|^2\right)}\right|^2 \tag{A.9}$$

and then,

$$\rho_{e,\max}=\left|\frac{2\left|S_{11}\right|\left|S_{12}\right|}{1-\left(\left|S_{11}\right|^2+\left|S_{12}\right|^2\right)}\right|^2 \tag{A.10}$$

The maximum correlation ($\rho_{e,max}$) based on the symmetrical mismatch case ($|S_{11}|=|S_{22}|$) gives the relation of input match (S_{ii}) and coupling (S_{ij}) to the correlation coefficient.

Appendix B. Radiation patterns and envelope correlations

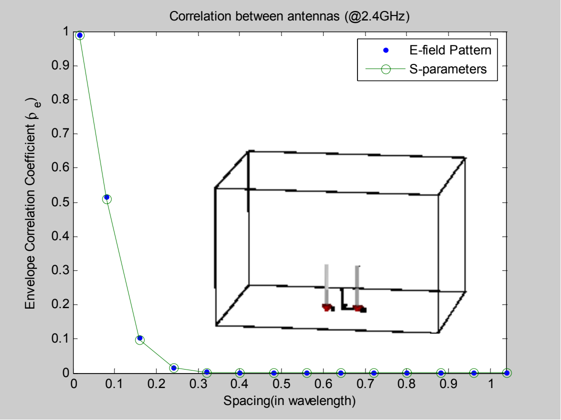

(a) Envelope correlation coeffeicient of monopole pair

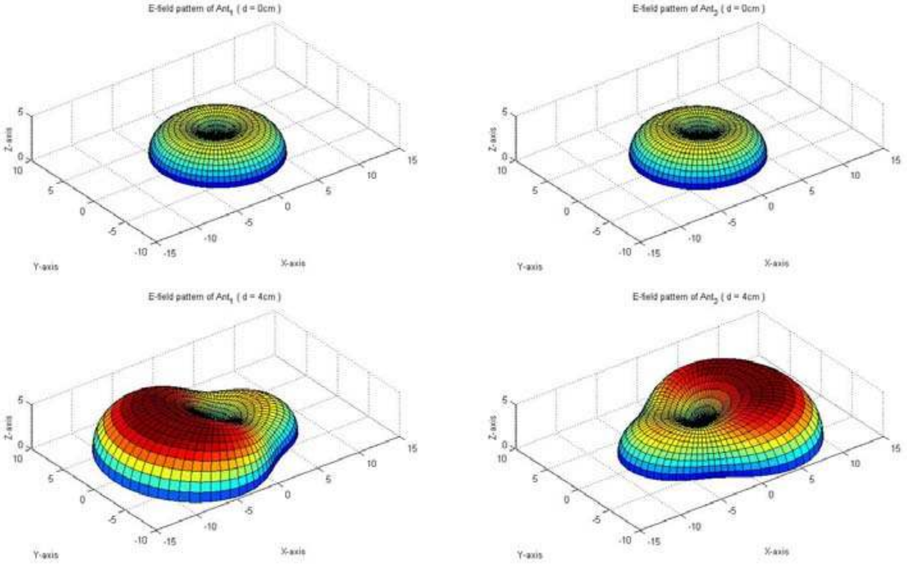

Figure 12 Envelope correlation coefficient and the radiation patterns of a monopole pair- these patterns are calculated when one is exited and the other is match-terminated (a) envelope correlation coefficients calculated based on the far-field radiation pattern and S-parameters of a monopole pair as a function of element spacing. It is apparent that when the two antennas are very close they act as one element and their radiation is drastically reduced due to strong mutual coupling, upon increasing their spacing and the reduced mutual coupling higher radiation patterns are demonstrated. At a spacing of xl radiation patterns are identical to their individual radiation patterns.

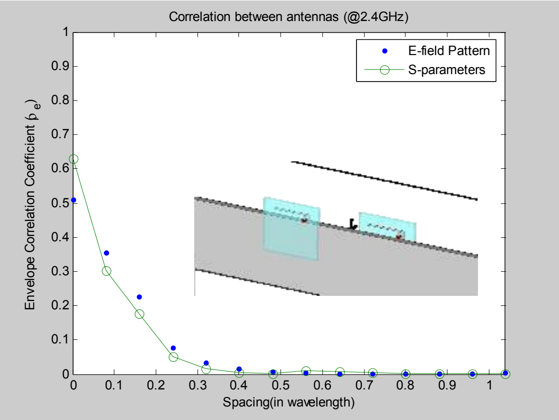

(a) Envelope correlation coefficient of single band PIFA pair in collinear 1 configuration

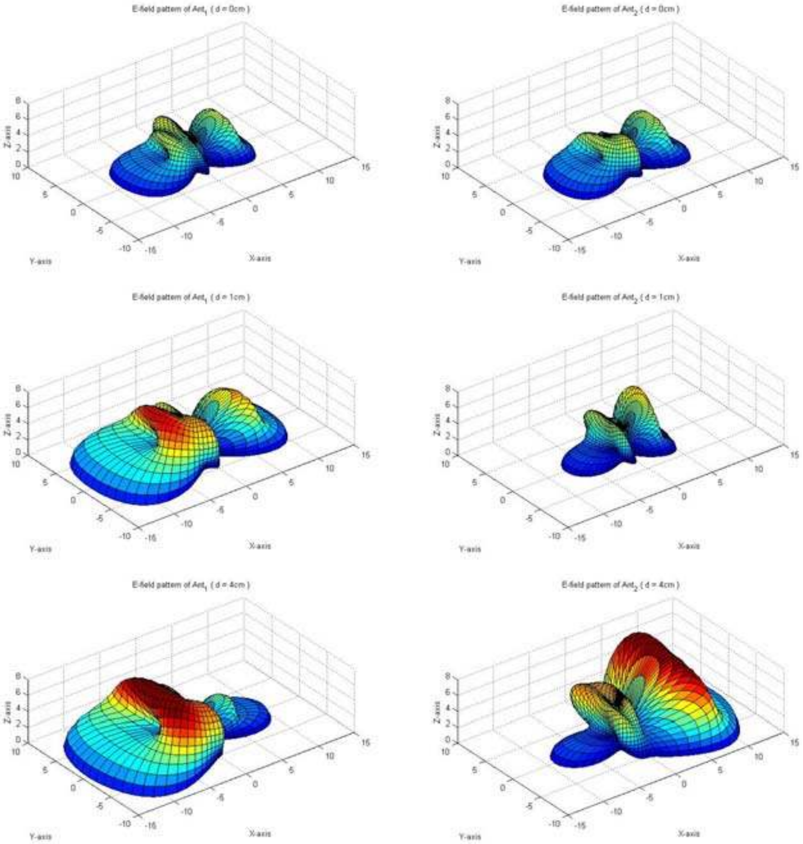

Figure 13 Envelope correlation coefficient and radiation patterns of single band PIFA collinear 1 pair (a) envelope correlation coefficients calculated based on far-field radiation pattern and s-parameters of monopole pair as a function of element spacing

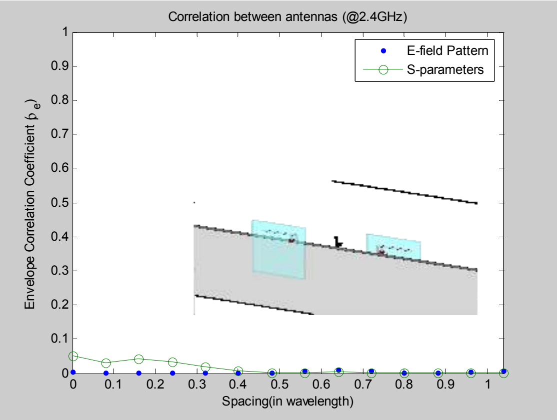

(a) Envelope correlation coefficient of single band PIFA pair in collinear 2 configuration

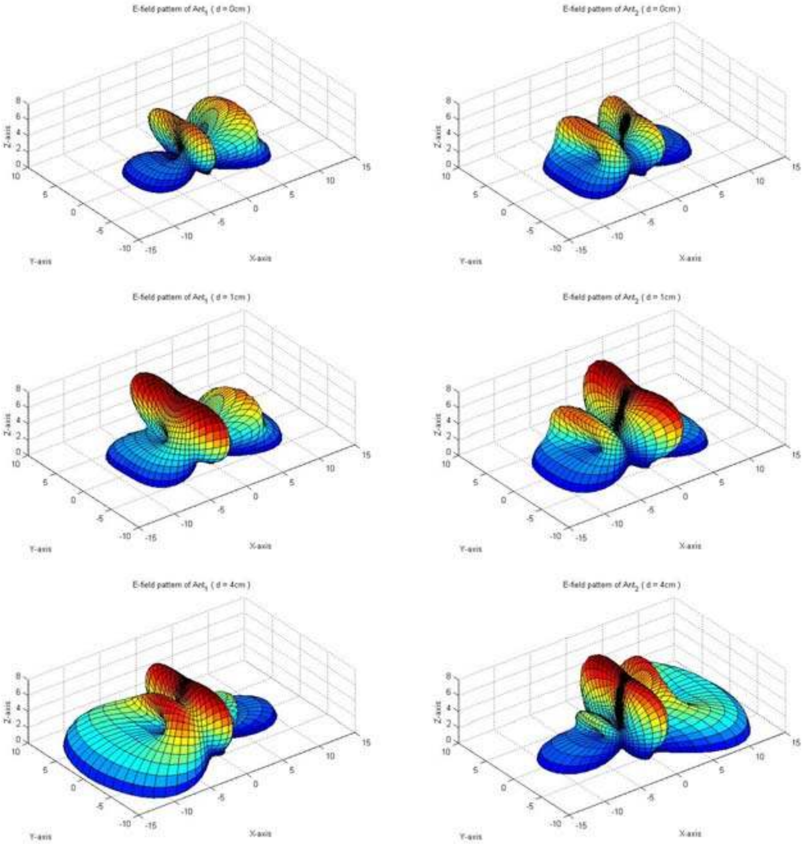

Figure 14 Envelope correlation coefficient and radiation patterns of single band PIFA collinear 2 pair (a) envelope correlation coefficients calculated based on far-field radiation pattern and s-parameters of monopole pair as a function of element spacing

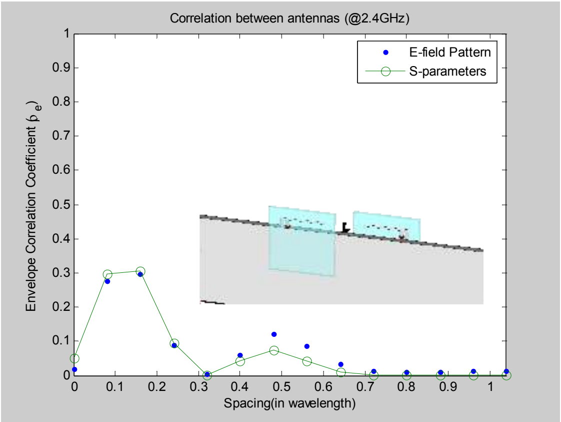

(a) Envelope correlation coefficient of single band PIFA pair in collinear 3 configuration

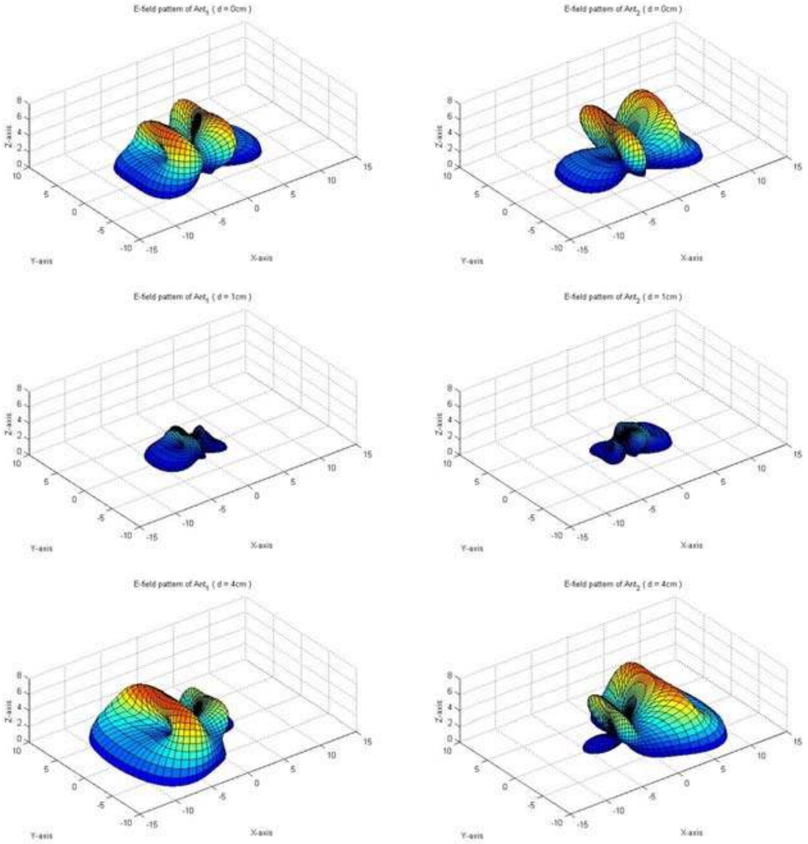

Figure 15 Envelope correlation coefficient and radiation patterns of single band PIFA collinear 3 pair (a) envelope correlation coefficients calculated based on far-field radiation pattern and s-parameters of monopole pair as a function of element spacing

VITA

Sung-Woo Lee was born in Seoul, Korea in September 24 1972. He received his B.E. degree in Electrical Engineering from Kookmin University on the February of 1998. He wrote a thesis titled as “Design and Implementation of a Single Bias FET Source Mixer” for his B.E. degree. He received his M.S. degree in Electrical Engineering in 2000 from Kookmin University with his thesis, “A Study on the Design and Implementation of a Source Pumped FET Image Rejection Mixer”. In July 2003, he received his second M.S. degree in Electrical Engineering from the Arizona State University at Tempe, AZ with his thesis, titled “Design and Analysis of a Nonlinear Microwave Circuit using Extended FDTD Method”.

He started his Ph.D. study as a graduate teaching and research assistant at the University of Tennessee, Knoxville in the August of 2003. He completed the doctorate in 2008. He has been working in the area of antenna design and implementation in different wireless communication services at Antenna and Microwave System Group under the supervision of Dr. Aly E. Fathy for his Ph.D. research. He also has been working to support the High Power Radio Frequency (HPRF) group as a graduate student intern in the Spallation Neutron Source (SNS) at the Oak Ridge National Laboratory (ORNL).

His future research interests include computational electromagnetics, antenna analysis and design, RF/microwave circuit and system design, and particle acceleration and interactions with microwave power signals.